UNIVERSIDADE FEDERAL DE MINAS GERAIS

Programa de Pós-Graduação em Física

Thiago Carvalho Ribeiro

Science and technology of solar cells based on SnS, SnS_2 and GeS

Belo Horizonte
2023

Thiago Carvalho Ribeiro

SCIENCE AND TECHNOLOGY OF SOLAR CELLS BASED ON SNS, SNS_2 AND GES

Tese apresentada ao Programa de Pós-Graduação em Física da Universidade Federal de Minas Gerais como requisito parcial para obtenção do grau de Doutor(a) em Ciências, área de concentração: Física.

Orientador: Prof. Dr. Rogério Magalhães Paniago
Coorientadora: Dra. Thaís Chagas Peixoto Silva

Belo Horizonte
2023

Dados Internacionais de Catalogação na Publicação (CIP)

R484s Ribeiro, Thiago Carvalho.
Science and technology of solar cells based on SnS, SnS2 and GeS / Thiago Carvalho Ribeiro. – 2023.
113f. : il.

Orientador: Rogério Magalhães Paniago.
Coorientadora: Thaís Chagas Peixoto Silva.
Tese (doutorado) – Universidade Federal de Minas Gerais, Departamento de Física.
Bibliografia: f. 103-113.

1. Células solares. 2. Sulfetos. 3. Semicondutores. 4. Microscopia de tunelamento de varredura. 5. Espectroscopia de tunelamento. I. Título. II. Paniago, Rogério Magalhães. III. Universidade Federal de Minas Gerais, Departamento de Física.

CDU – 621.383.5 (043)

Ficha catalográfica elaborada por Romário Martins Ribeiro – CRB6 3595
Biblioteca Professor Manoel Lopes de Siqueira – Departamento de Física - UFMG

UNIVERSIDADE FEDERAL DE MINAS GERAIS
INSTITUTO DE CIÊNCIAS EXATAS
PROGRAMA DE PÓS-GRADUAÇÃO EM FÍSICA

ATA DE DEFESA DE TESE

ATA DA SESSÃO DE ARGUIÇÃO DA 415ª TESE DO PROGRAMA DE PÓS-GRADUAÇÃO EM FÍSICA, DEFENDIDA POR THIAGO CARVALHO RIBEIRO orientado pelo professor Rogerio Magalhães Paniago e coorientado pela doutora Thais Chagas Peixoto Silva, para obtenção do grau de **DOUTOR EM CIÊNCIAS, área de concentração física**. Às 14 horas de cinco de abril de dois mil e vinte e três, reuniu-se a Comissão Examinadora, composta pelos professores **Rogerio Magalhães Paniago** (Orientador - Departamento de Física/UFMG), **Leonardo Cristiano Campos** (Departamento de Física/UFMG), **Klaus Wilhelm Heinrich Krambrock** (Departamento de Física/UFMG), **Abner de Siervo** (Instituto de Física Gleb Wataghin/UNICAMP) e **Christoph Friedrich Deneke** (Instituto de Física Gleb Wataghin/UNICAMP) para dar cumprimento ao Artigo 37 do Regimento Geral da UFMG, submetendo o Mestre **THIAGO CARVALHO RIBEIRO** à arguição de seu trabalho de Tese de Doutorado, que recebeu o título de **"Science and technology of solar cells based on SnS, SnS$_2$ and GeS"**. O candidato fez uma exposição oral de seu trabalho durante aproximadamente 50 minutos. Após esta, os membros da comissão prosseguiram com a sua arguição, e apresentaram seus pareceres individuais sobre o trabalho, concluindo pela aprovação do candidato.

Belo Horizonte, 05 de abril de 2023.

Prof. Rogerio Magalhães Paniago
Orientador do estudante
Departamento de Física/UFMG

Prof. Abner de Siervo
Instituto de Física Gleb Wataghin/UNICAMP

Prof. Leonardo Cristiano Campos
Departamento de Física/UFMG

Prof. Christoph Friedrich Deneke
Instituto de Física Gleb Wataghin/UNICAMP

Prof. Klaus Wilhelm Heinrich Krambrock
Departamento de Física/UFMG

Candidato: Thiago Carvalho Ribeiro

Documento assinado eletronicamente por **Abner de Siervo**, **Usuário Externo**, em 05/04/2023, às 16:27, conforme horário oficial de Brasília, com fundamento no art. 5º do Decreto nº 10.543, de 13 de novembro de 2020.

Documento assinado eletronicamente por **Christoph Friedrich Deneke**, **Usuário Externo**, em 05/04/2023, às 16:27, conforme horário oficial de Brasília, com fundamento no art. 5º do Decreto nº 10.543, de 13 de novembro de 2020.

Documento assinado eletronicamente por **Thiago Carvalho Ribeiro**, **Usuário Externo**, em 05/04/2023, às 16:32, conforme horário oficial de Brasília, com fundamento no art. 5º do Decreto nº 10.543, de 13 de novembro de 2020.

Documento assinado eletronicamente por **Rogerio Magalhaes Paniago**, **Professor do Magistério Superior**, em 05/04/2023, às 17:03, conforme horário oficial de Brasília, com fundamento no art. 5º do Decreto nº 10.543, de 13 de novembro de 2020.

Documento assinado eletronicamente por **Klaus Wilhelm Heinrich Krambrock**, **Professor do Magistério Superior**, em 05/04/2023, às 18:22, conforme horário oficial de Brasília, com fundamento no art. 5º do Decreto nº 10.543, de 13 de novembro de 2020.

Documento assinado eletronicamente por **Leonardo Cristiano Campos**, **Professor do Magistério Superior**, em 06/04/2023, às 14:26, conforme horário oficial de Brasília, com fundamento no art. 5º do Decreto nº 10.543, de 13 de novembro de 2020.

A autenticidade deste documento pode ser conferida no site https://sei.ufmg.br/sei/controlador_externo.php?acao=documento_conferir&id_orgao_acesso_externo=0, informando o código verificador **2209052** e o código CRC **5F0349D1**.

Agradecimentos

Gostaria de agradecer aos meus pais, Fátima e Moacir, minha irmã Déborah e minha companheira Camila, por estarem sempre presentes e me apoiarem incondicionalmente. Seu encorajamento, afeto, união e fé em mim foram fundamentais para minha jornada acadêmica.

Também quero agradecer ao meu orientador, o professor Rogério Paniago, pela paciência e comprometimento durante todo o período do meu doutorado. Seus ensinamentos, conselhos e discussões foram essenciais para meu desenvolvimento como pesquisador, e sua abordagem prática e aplicada da ciência tem sido uma grande fonte de inspiração.

Agradeço à minha coorientadora, Thais Chagas, pelos seus valiosos ensinamentos técnicos e experimentais, e por sua paciência, dedicação e disponibilidade em me ajudar sempre que precisei. Sua orientação foi fundamental para meu desenvolvimento acadêmico e profissional.

Também sou grato ao Angelo Malachias (meu coorientador de consideração) por seu suporte técnico e científico durante toda minha jornada de doutorado, e ao Gustavo Sáfar por estar sempre pronto para me ajudar com dúvidas relacionadas ao trabalho.

Agradeço ainda ao corpo técnico do departamento de Física, especialmente ao Pádua e Sergio, pelos valiosos ensinamentos técnicos e experimentais que foram fundamentais para meu desenvolvimento como físico experimental e aplicado.

Por fim, agradeço aos meus amigos e colegas do departamento de física, dos laboratórios de Nanoscopia UHV e Nanomateriais pelo suporte emocional e experimental ao longo de minha jornada acadêmica. E também às agências de financiamento FAPEMIG, INCT-Nanocarbono, CNPq e CAPES pelo apoio financeiro.

Resumo

Esta tese de doutorado teve como objetivo construir uma base de conhecimento sobre a ciência e tecnologia de células solares, com foco no uso de materiais novos e ecologicamente corretos. A tese está dividida em duas partes. A primeira parte desenvolveu o uso de microscopia e espectroscopia de tunelamento de varredura (STM / STS) para entender o comportamento eletrônico do monossulfeto de estanho (SnS), um material potencial para células solares. A segunda parte construiu e caracterizou uma célula solar funcional com base na combinação de dois novos candidatos, GeS e SnS_2. Filmes finos desses materiais foram facilmente produzidos por deposição de fase vapor, resultando na formação de semicondutores GeS tipo p e SnS_2 tipo n. Uma célula solar baseada nesses dois materiais foi caracterizada com sucesso usando curvas J-V padrão e mostrou uma resposta de fotocorrente estável. Medidas de eficiência quântica mostraram que o pico de eficiência da célula solar está exatamente onde a eficiência das células de silício padrão diminui acentuadamente. Portanto, a célula solar GeS/SnS_2 pode ter uso potencial como dispositivo complementar para produzir células solares tandem de silício. O trabalho fornece uma estrutura para a rápida determinação da adequação e aplicabilidade de SnS, SnS_2 e GeS para células solares e outras possíveis aplicações optoeletrônicas.

Palavras-chave Monossulfeto de estanho, dissulfeto de estanho, monossulfeto de gemânio, semicondutores, deposição em fase vapor, material 2D, microscopia e espectroscopia de tunelamento de varredura, célula solar.

Abstract

This PhD thesis aimed to build a knowledge basis on solar cell science and technology, with a focus on using environmentally friendly novel materials. The thesis is divided into two parts. The first part developed the use of scanning tunneling microscopy and spectroscopy (STM/STS) to understand the electronic behavior of tin monosulfide (SnS), a potential material for solar cells. The second part constructed and characterized a functional solar cell based on the combination of two novel candidates, GeS and SnS_2. Thin films of these materials were easily produced by vapor phase depositon, resulting in the formation of p-type GeS and n-type SnS_2 semiconductors. A solar cell based on these two materials was successfully characterized using standard J-V curves and showed a stable photocurrent response. Quantum efficiency measurements showed that the peak of efficiency of the solar cell is exactly where the efficiency of standard silicon collar cells sharply decreases. Therefore, the GeS/SnS_2 solar cell may be of potential use as a complimentary device to produce silicon tandem solar cells. The work provides a framework for the rapid determination of the suitability and applicability of SnS, SnS_2 and GeS for solar cells and other potential optoelectronic applications.

Keywords: Tin monosulfide, Tin disulfide, Gemanium monosulfide, Semiconductors, Vapor phase deposition, 2D material, Scanning tunneling Microscopy and Spectroscopy, Solar Cell.

Contents

1- Introduction

The global human population reached 8 billion in 2022 and there is a forecast that 10 billion will inhabit the Earth by the middle of this century [1]. According to this drastic increase in population, humanity needs to find a way to fulfill the energy demand in the near future. Nowadays, global energy utilization is met by traditional, non-sustainable, and mainly based on fossil fuels (more than 80%) [2]. This excessive usage of fossil fuels is followed by the vast production of CO_2, resulting in climate changes and other crucial environmental and health issues. Alternatives to the energy demand in a more environment-friendly way are renewable energy sources. Among them, solar energy is one of the most important, as it is non-polluting, abundant, and universal. This energy can be considered renewable since it is unlimited for humankind's lifespan. The Sun provides 4.6×10^{20} J of energy in one hour, which is equivalent to human energy consumption during a year. For comparison, 3 trillion barrels of oil contain the equivalent of 1.7×10^{22} J of energy, which is provide by the Sun to the Earth in 1.5 days [3].

Despite the abundance of solar energy, the current use for world electricity production is minimum, about 0.015% [2]! The huge gap between the potential of solar energy usage and our current use is due to the cost of conversion capacity. Nevertheless, the progress in the development of photovoltaic (PV) technologies over the recent few years is notable. The most efficient solar cells based on crystalline silicon have an efficiency of 27.6% [4]. This powerful PV technology has left the laboratory and reached commercial applications, dominating the PV market. However, the production of silicon solar cells can be energy-intensive and can result in the emission of greenhouse gases, which can have a negative environmental impact. Thus, exploring alternative solar cells that are more environmentally friendly is essential in the quest to transition from fossil fuel usage to cleaner energy sources.

Thin film PV technologies, particularly those with chalcogenide semiconducting absorbers, are a viable option to meet this requirement as they have a lower carbon footprint than traditional silicon solar cells. This is due to their manufacturing process, which requires less energy and fewer raw materials, resulting in lower emissions.These materials can combine significant conversion efficiency (PCE) with efficient materials usage. Solar cells based on copper indium gallium selenide (CIGS) and cadmium telluride (CdTe) have been extensively studied due to their promising photovoltaic properties and achieved PCEs higher than 20% [5]. However, there are serious limitations regarding the production and use of solar cells with these materials. The scarcity of gallium and indium for CIGS production and the toxicity of cadmium used in CdTe present an impediment for the mass production of solar cells based on these materials.

Tin monosulfide (SnS), germanium monosulfide (GeS), and tin disulfide (SnS_2) are simple binary metal chalcogenide compounds of the IV-VI family. They have recently attracted interest in solar cell applications since they are semiconducting materials with suitable electronic gaps, optical properties, and electron mobility. In addition, the elements that constitute these compounds are of low cost, present low toxicity, and are earth-abundant, making them advantageous when compared to other well-established solar cell materials previously mentioned. SnS has also attracted considerable interest for use in other optoelectronic devices, such as near infrared (NIR) detectors [6] and optical sensors [7].

Although there are various potential applications, the primary one lies in its capacity to function as an absorber layer in solar cells, since SnS is a p-type semiconductor material with a suitable electronic bandgap (1.1–1.4 eV) [8–10]. It also presents a fairly high light absorption coefficient (>10^5 cm^{-1}) [11,12] and good charge carrier mobility (15 $cm^2 \cdot V^{-1} \cdot s^{-1}$) [13,14]. Germanium sulfide (GeS) is also synthesized as a p-type semiconductor and exhibits a bandgap in the visible region (1.6 – 1.7 eV) [15–17], large light absorption coefficient (>10^4 cm^{-1}) [17], and high carrier mobility (~ 86 $cm^2V^{-1}s^{-1}$) [18]. All these properties make GeS a promising material for tunable light emitters with the possibility of interlayer twist [19–21], enabling its use in visible light photodetectors [22–24] or as an absorber layer in solar cells [17]. Complementarily, SnS_2 is an n-type semiconductor with a flexible wide-bandgap in the range of 1.8-2.9 eV [25–29]. SnS_2 has a plethora of potential applications ranging from diodes [30], photodectors [31], gas sensors [32], batteries [33], supercapacitors [34], field effect transistors [35], and buffer layers for heterojunction solar cells [29]. The broad capabilities of these materials turn them into suitable candidates for the replacement of hazardous materials in optoelectronic devices.

In the present work, we have prepared two-dimensional nano-platelets of tin sulfide on graphite using vapor phase deposition (VPD) under a controlled temperature gradient. Remarkably, we observe two types of growth modes: (i) a dominant one with platelet-like flat crystals and (ii) a less favorable one, formed by atomically flat spiral terraces. Both structures present a chemical composition compatible with SnS. Using scanning tunneling microscopy (STM) and spectroscopy (STS), we observe that, whereas flat SnS platelets exhibit fluctuations in the bandgap and doping, spiral ones exhibit stable, homogeneous bandgap, and negative doping. The observed local electronic band gap variation and doping fluctuation of flat platelets may be the most significant cause of the low efficiency of SnS solar cells. In contrast, the spiral ones, due to its homogeneous band gap and doping, is of potential interest for the production of more efficient SnS-based solar cells and other optoelectronic devices. Using selected area electron diffraction (SAED), we determine that, platelets exhibiting the unstable electronic phase are associated with the common orthorhombic structure of SnS while the electronically stable spiral platelets are formed by SnS in the cubic phase. The production of this less favorable phase on large surface areas is of potential interest for the development of more efficient tin sulfide-based solar cells. In addition, our analysis of solar cell materials using STM/STS and SAED provides a framework for the rapid determination of fundamental properties, as well as the suitability and applicability of materials for other potential optoelectronic applications.

The second focus of this thesis is on GeS that was deposited by PVD as a top layer of a structure composed of indium tin oxide (ITO) covered by SnS_2. The solar cells produced using these materials and gold/ITO as contacts have resulted in stable solar cells. Solar simulator measurements provided a framework for the photovoltaic properties of this heterostructure prototype. The density of current versus voltage (J-V) curves present no hysteresis for different light intensities and time-dependent photocurrent response. This was recorded by alternating bright and dark conditions with AM 1.5G illumination, indicating the high stability of the device. Remarkably, our solar cells present a better quantum efficiency (QE) compared to the diminished response exhibited by crystalline silicon (c-Si) solar cells, which will be further illustrated in chapter 6. Our results consist of a proof-of-principle of a prototype environmentally friendly solar cell made of two cost-effective binary green compounds. Therefore, the GeS/SnS_2 solar cell may be of potential use as a complementary device to produce silicon tandem solar cells.

This thesis covers various aspects related to solar cell technology and emerging materials for solar cell applications. In the first two chapters, the introduction to solar energy and solar irradiation is given, followed by an outline of solar cell development, including first-generation (1GEN), second-generation (2GEN), and third-generation (3GEN) solar cells. The operation of thin film heterostructure solar cells. The next section covers emerging materials for solar cell applications, including tin sulfide (SnS), germanium sulfide (GeS), and tin disulfide (SnS_2). Chapter 4 discusses various experimental methods, such as vapor phase deposition, Raman spectroscopy, scanning electron microscopy (SEM), energy-dispersive X-ray spectroscopy (EDS), X-ray diffraction (XRD), scanning tunneling microscopy and spectroscopy (STM/STS), transmission electron microscopy (TEM), selected area electron diffraction (SAED), as well as current density-voltage (J-V) characteristics and external quantum efficiency systems. The following two chapters present experimental studies on the electronic gap stability of two-dimensional tin monosulfide phases and the demonstration of an environmental-friendly solar cell based on two-dimensional materials GeS and SnS_2, respectively. Finally, the thesis concludes with a summary and outlooks section and a list of publications.

2. Solar cell technology

2.1 Solar energy

The amount of energy that the Sun continuously delivers to Earth, approximately 1.2 × 10^5 TW, is significantly greater than the rate at which human civilization produces and consumes energy (~13 TW) [3]. In other words, solar energy is capable of single-handedly meeting humanity's energy demands. There are three main ways to utilize solar energy: (i) sunlight can produce chemical fuel through natural or artificial photosynthesis, (ii) it can be converted into electricity using solar cells, and (iii) it can produce heat. Figure 1 provides a schematic of these energy conversion processes.

Despite the abundance and versatility of solar energy, its current usage is relatively small. Only 0.015% is used for producing electricity, while 0.3% is utilized for heating purposes. The largest use of solar energy is in natural photosynthesis (11%) [2]. In contrast, over 80% of our energy is derived from fossil fuels, which are exhaustible, harmful to the environment, unevenly distributed, and non-renewable. Solar energy, on the other hand, is an inexhaustible and unrestricted energy source that has the potential to become a clean and sustainable alternative to fossil fuels and should be considered as such for a cleaner and more sustainable future.

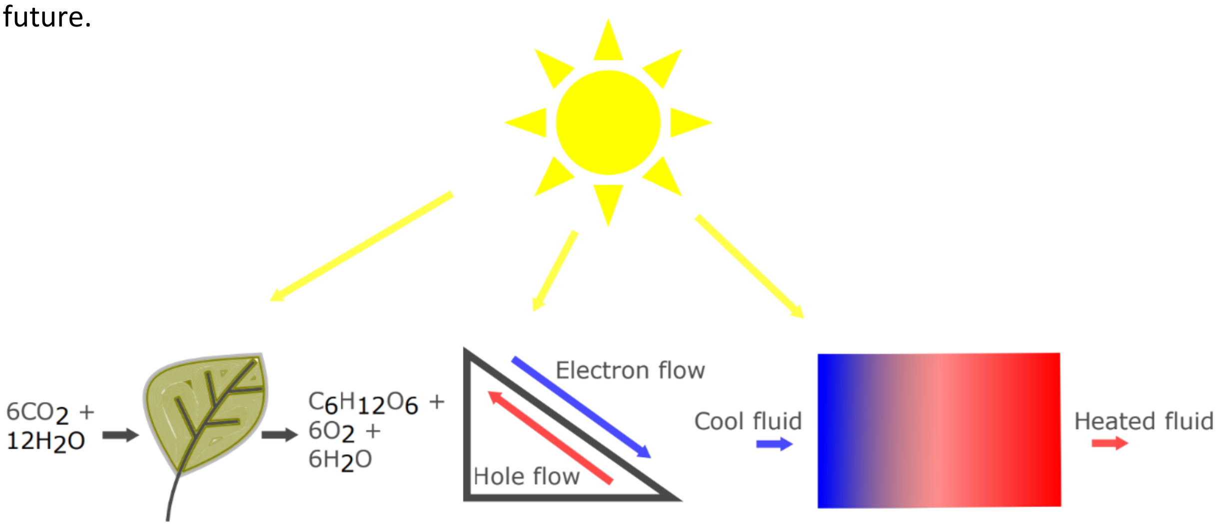

Figure 1. There are three methods for transforming solar energy into different forms of energy: (a) creating chemical fuel through photosynthesis, (b) inducing electrons in a solar cell to produce electricity, and (c) focusing sunlight to generate heat.

2.2 Solar irradiation

All the solar energy usage depends on how much sunlight is accessible. The solar irradiance that reaches the Earth's surface is highly variable due to atmospheric effects [36]. Approximately 30% of the irradiance is lost due to natural phenomena such as atmospheric absorption, Rayleigh scattering, and dust and aerosol scattering. Moreover, the path that sunlight must travel through the atmosphere before reaching the Earth's surface has the greatest impact on irradiance loss. This can be estimated by the degree of attenuation, which serves as the basis for the standardized air mass (AM) scale. The AM scale is a method of quantifying the impact of atmospheric attenuation on the amount of solar radiation that reaches the Earth's surface. It is calculated using the following equation:

$$AM = \frac{1}{\cos(\theta)}, \tag{1}$$

where θ is the solar zenith angle, which is the angle between the sun and the observer’s zenith (the point directly overhead).

The AM0 configuration refers to the solar irradiation outside the Earth's atmosphere when the Sun is at its zenith position (i.e., $\theta = 0°$). This configuration is considered the standard for extraterrestrial applications. On the other hand, AM1 also occurs at $\theta = 0°$, but it takes into account the effects of atmospheric absorption, scattering, and reflection on the solar spectrum. In this scenario, light travels through the atmosphere along the shortest path and experiences minimal attenuation. Finally, AM1.5G is the terrestrial standard reference that is widely used in the study of solar radiation and PV devices. It represents the solar spectrum at the Earth's surface at mid-latitudes where the majority of developed countries employing solar technologies are located. AM1.5G corresponds to θ = 48.2° and an irradiation of approximately 1000 W/m^2. The "G" in AM1.5G stands for "global" and represents a weighted average of solar radiation at different angles of incidence, taking into account the relative proportions of direct and diffuse components of sunlight. Figure 2a illustrate different AM configurations and Figure 2b depicts the solar spectral irradiance for AM0 and AM1.5G configurations as well as the absorption bands of water vapor (H_2O), oxygen (O_2), ozone (O_3), and carbon dioxide (CO_2).

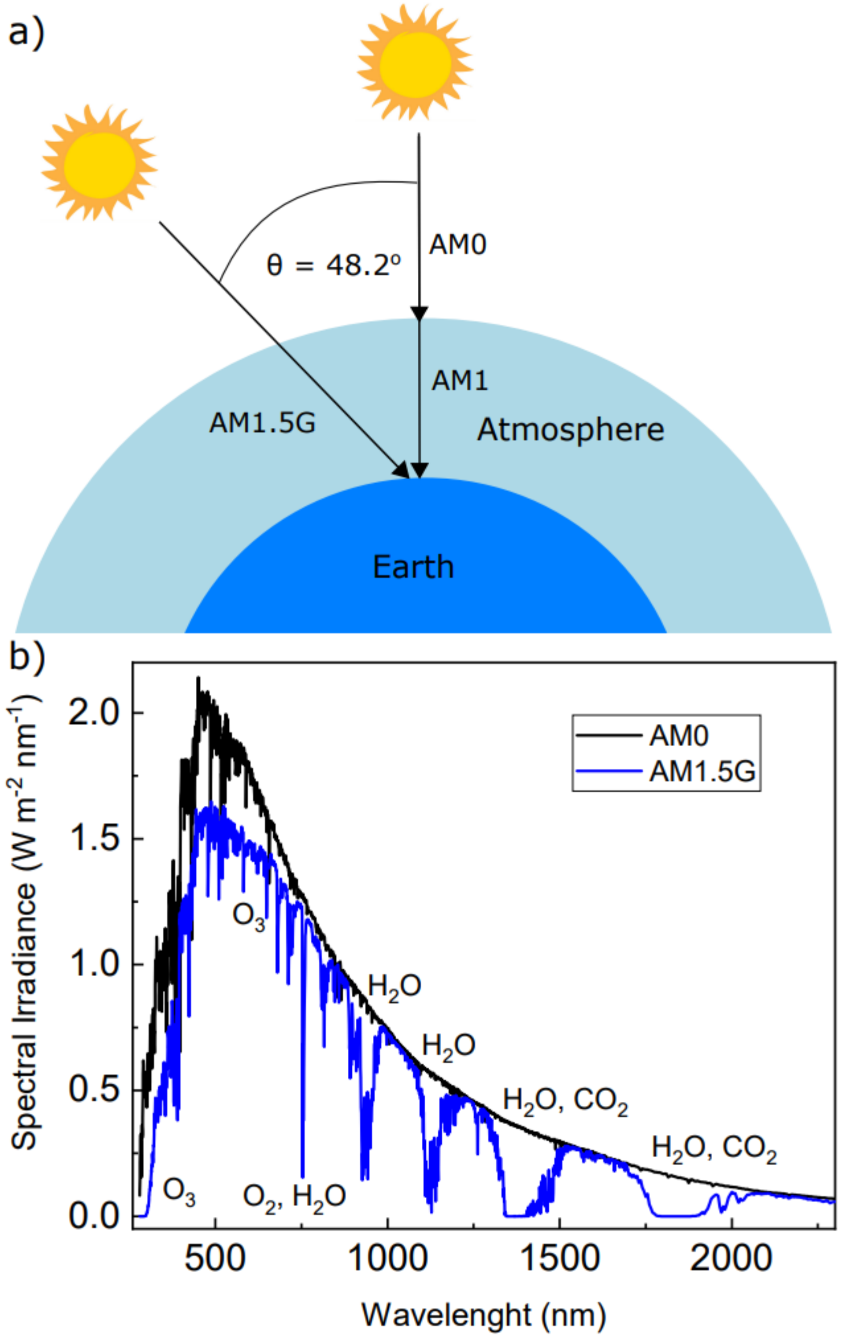

Figure 2. a) Depicts the concepts of AM0, AM1, and AM1.5G solar irradiances. Meanwhile, Figure 2.b) displays the solar irradiation spectra of AM0 and AM1.5G (ASTM G-173-03 global, see Reference https://www.nrel.gov/grid/solar-resource/spectra-am1.5.html), emphasizing the atmospheric absorption areas of various elements such as oxygen, ozone, water vapor, and carbon dioxide.

2.3 Outline of solar cell development

As previously stated, solar cells can generate useful electricity directly from sunlight through the photovoltaic effect. The French physicist Alexandre Edmond Becquerel first observed this phenomenon in 1839 [37]. Since then, there have been many research and development work in solar PV technologies. However, this development has undergone numerous changes, leading to the classification of solar cells into different generations as depicted in Figure 3. The goal of each generation is to lower costs while improving efficiency.

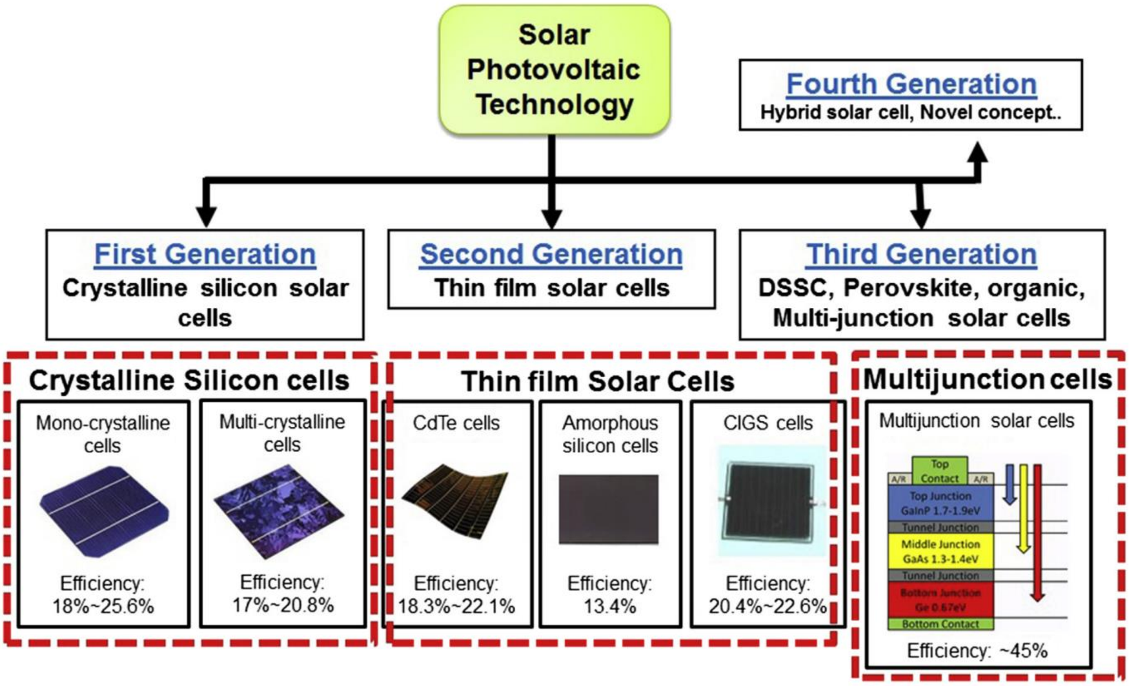

Figure 3. The efficiency range achieved by different generations of solar cells, including first, second, third, and fourth generation solar cells. The figure is sourced from reference [38].

2.3.1 First-generation (1GEN)

First-generation solar cells are based on mono or polycrystalline silicon and gallium arsenide. These cells are the most common and widely used in the world [2]. The advantages of this generation are their reliability and durability [39]. Nevertheless, this technology is based on thick crystalline films (mainly Si) which not only leads to limited efficiency (see Figure 3) but also the production can be energy-intensive and can result in the emission of greenhouse gases, which can have a negative environmental impact [39]. Additionally, their rigid and inflexible nature makes them unappropriated for applications that necessitate flexible solar panels. Despite these limitations, 1GEN solar cells remain a critical component of the solar industry and are expected to persist in playing a pivotal role in the transition to a more sustainable and renewable energy future.

2.3.2 Second-generation (2GEN)

The second generation of solar cells were developed with the goal of reducing the high costs prevalent in the 1GEN through the utilization of thin film technologies. Unlike 1GEN solar cells, which are mainly based on silicon, 2GEN can be made of a variety of materials, such as amorphous silicon, cadmium telluride (CdTe) and copper indium gallium selenide (CIGS) [39]. The 2GEN solar cells are based on thin layers of semiconductor materials that have lower cost and simpler manufacturing processes than the 1GEN. Moreover, the use of less material makes these solar cells more versatile than 1GEN solar cells, allowing a variety of applications. They are lightweight, flexible, and thin which is interesting to building-integrated PV, where solar panels are integrated into the design of buildings.

Overall, 2GEN solar cells represent a major advance in PV technology. However, their efficiency is generally lower compared to 1GEN (see Figure 3), and the use of materials has serious commercial limitations due to the scarcity of gallium and indium and the serious toxicity of cadmium. As a result, further research and development are essential to find new materials and enhance the efficiency of solar cells.

2.3.3 Third-generation (3GEN)

The goal of third-generation solar cells is to improve efficiency and environmental sustainability by building upon the advancements achieved by 2GEN solar cells. 3GEN solar cells incorporate a range of innovative designs such as dye-sensitized solar cells, hybrid solar cells that utilize inorganic quantum dots or nanomaterials in conjunction with organic materials, and multi junctions based on group IV and group III-V elements (see Figure 3). Recent advancements in PCE of organic solar cells have demonstrated their potential for practical applications.

Currently, the most efficient type of solar cell is the multijunction cell, which can achieve power conversion efficiencies of up to 47.1% [40]. Single-junction GaAs cells follow with efficiencies of up to 30.5% [41], while c-Si cells can reach up to 27.6% [4], and thin film technologies fall within the range of 14% to 23.35% [42]. Among emerging PV technologies, the efficiency ranges from 12% to 29.1% [43], with monolithic perovskite tandem cells exhibiting the highest performance among them [44].

However, most of the research and development efforts for third-generation PV technology are currently being carried out under laboratory conditions by research groups in universities or companies. As a result, the commercial availability of these technologies is still limited.

2.4 Thin film heterostructure solar cell operation

In these devices, sunlight is absorbed by a semiconductor material, creating an electron-hole pair that is transported to the electrical contacts of the solar cell to generate current for an external circuit. The power conversion process involves several steps, each of which requires a specific layer as shown in Figure 4. The scheme is described in detail in the following paragraphs.

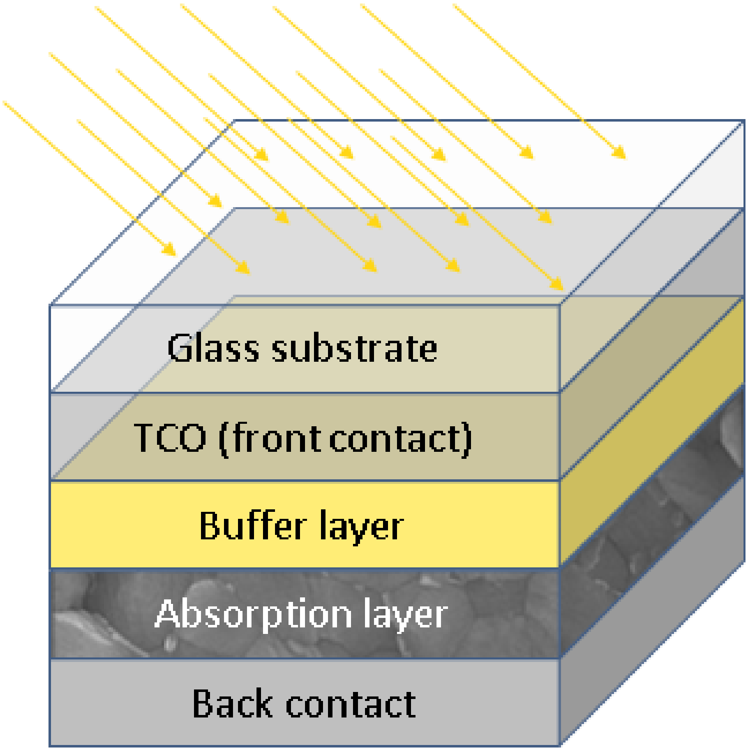

Figure 4. A heterojunction solar cell is illustrated, which comprises several layers including a glass substrate, a transparent conducting oxide (TCO) layer serving as the front contact, a buffer layer, an absorption layer, and a back contact. The diagram provides a visual representation of the layers that make up a heterojunction solar cell.

The absorption layer plays a crucial role in solar cells by absorbing light. It is typically made of p-type semiconductor material with a high optical absorption coefficient and a suitable energy bandgap that influences its properties. According to the Shockley-Queisser (S-Q) theory [45], the maximum theoretical efficiency of a solar cell, as illustrated in Figure 5, can be achieved by a material whose energy bandgap is within the range of 1.1-1.4 eV. Additionally, the absorber film synthesis induces crystal lattice defects, such as grain boundaries, intrinsic point defects (vacancies), and impurities. These defects create extra electronic states within valance and conduction band [46] that can influence the efficiency of the solar cell.

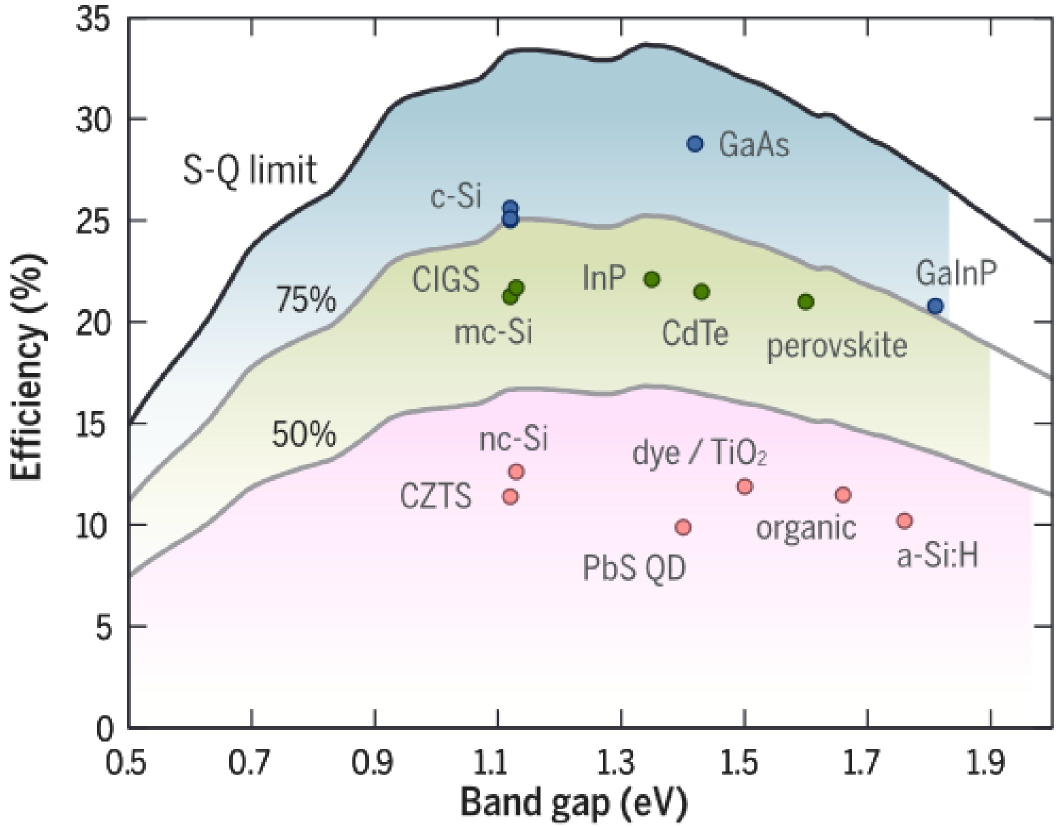

Figure 5. The theoretical Shockley-Queisser detailed-balance efficiency limit as a function of band gap. The black line shows the efficiency limit, while the gray lines illustrate 75% and 50% of that limit. This figure from reference [47] includes the efficiency limits for several materials used as an absorber layer in solar cells, plotted against their respective band gaps.

The buffer layer is composed of n-type semiconductor material and is responsible for creating a junction with the absorption layer. When the absorption layer and the buffer layer are joined to form a *p-n* junction, excess electrons from the *n-type* material move to the p-type side, and excess holes from the p-type material move to the *n-type* side. This charge movement exposes positive ion cores on the n-type side and negative ion cores on the p-type side, resulting in the formation of an electric field at the junction and the depletion region. A schematic of a *p-n junction* is shown in Figure 6a and 6b. When light strikes the surface of a solar cell, photons are absorbed by the semiconductor material, which excites electrons to higher energy levels. If the energy of the absorbed photon is greater than the bandgap energy of the semiconductor material, an electron-hole pair is created. The electric field across the depletion region then separates the electron and the hole, creating a flow of electrons towards the n-type material and a flow of holes towards the p-type material, which are then transported to the electrical contacts.

The energy band alignment plays an important role in the device's efficiency [48]. The magnitude and sign of the conduction band offset (ΔE_C) between the *p-* and *n-type* semiconductors are crucial to define the solar cells' carrier transport and recombination. The presence of a significantly negative value of ΔE_C results in a conduction band offset with a cliff-like profile at the heterojunction (see Figure 6c). This causes a loss of energy for electrons as they move across, facilitating unfavorable interface recombination. Conversely, a considerably positive value of ΔE_C results in a conduction band offset with a spike-like profile at the heterojunction (see Figure 6d). This creates a significant energy barrier that impedes photocurrent collection. However, an optimal conduction band offset is desirable to reduce interface recombination without sacrificing photocurrent collection.

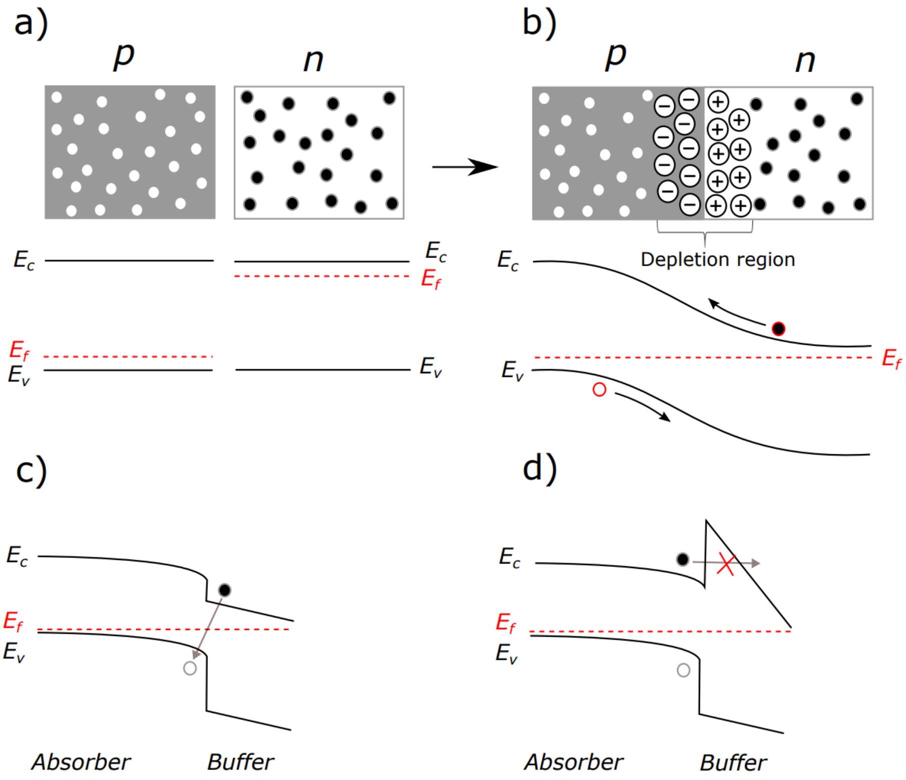

Figure 6. In the first sub-figure (a), p-type and n-type semiconductors are separated. In the second sub-figure (b), a p-n junction is formed, which creates the depletion region, and the energy band diagram in thermal equilibrium is shown. The third and fourth sub-figures (c and d) present a simplified schematic of the cliff-like and spike-like conduction band configurations at the pn-junction. This figure provides a visual representation of the formation of a p-n junction and the associated energy band diagrams at equilibrium.

The third component of a solar cell is the electrical contacts, which serve the purpose of collecting the charge carriers produced in the p-n junction and transporting them to the external circuit. While back electrical contacts are typically made of metals, front contacts need to be transparent to allow the incoming light to reach the p-n junction. Transparent conducting oxide (TCO) is commonly used as an optically transparent thin film and electrically conductive material for the front contacts, with indium tin oxide (ITO) being the most prevalent example.

The interface metal/semiconductor in solar cells can pose problems that limit their performance [49]. A Schottky barrier (SB), which is a potential barrier, can form at this interface, leading to a reduction in the photocurrent flow and ultimately reducing the PCE of the cell. Therefore, it is important to decrease the SB by optimizing the contact interfaces between the thin films to enhance the performance of a solar cell. Figure 7 shows the schematic diagram of band bending and illustrates the appearance of the Schottky barrier.

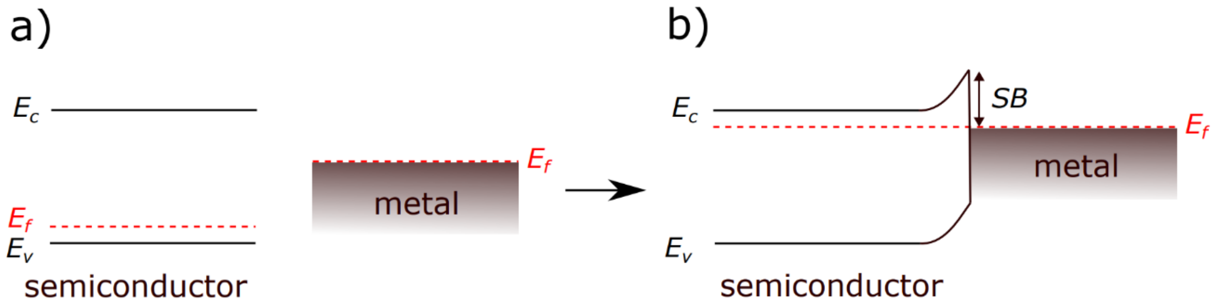

Figure 7. The figure depicts illustrations of band bending that occur at the interface between semiconductors and metals, leading to the formation of the Schottky barrier. Specifically, the figure shows how the energy bands bend at the contact between the two materials, causing the formation of the Schottky barrier. This figure provides a visual representation of the phenomenon of band bending and its impact on the electronic properties of semiconductors and metals at their interfaces.

3. Emerging materials for solar cell applications

3.1 Tin sulfide (SnS)

Tin monosulfide (SnS) is a monochalcogenide compound of the group IV-VI, which also includes SnSe, GeSe, and GeS. The most commonly reported crystal structure of SnSis the orthorhombic phase (α-SnS). This phase corresponds to a layered material with a puckered arrangement of atoms. Its orthorhombic unit cell belongs to the *Pnma* space group with a = 1.1200 nm, b = 0.3987 nm, and c = 0.4334 nm (ICSD number: 52108) as lattice parameters at room temperature. Figure 8 shows a schematic representation of the α-SnS crystal structure, revealing its layered lattice structure, each layer being two atoms thick. The unit cell contains two layers weakly coupled by van der Waals interactions.

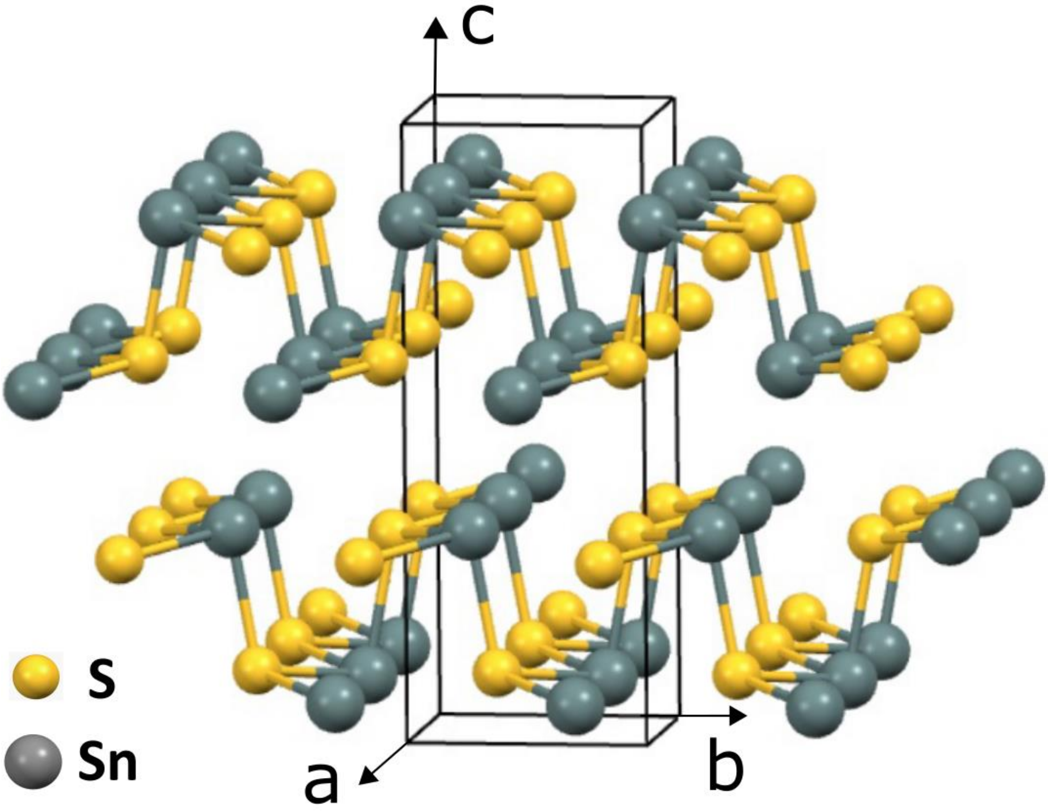

Figure 8. The figure shows the crystal structure of the layered orthorhombic α-SnS phase, including the unit cells represented by rectangular cuboids. This figure provides a visual representation of the physical structure of the α-SnS phase, which consists of layers of tin (Sn) and sulfur (S) atoms arranged in a particular way.

The α-SnS phase has attracted considerable interest for its potential use in optoelectronic devices which include near-infrared (NIR) detectors [6] and optical sensors [7]. Its main potential application is as an absorber layer in solar cells since α-SnS is a p-type semiconductor material with a suitable electronic bandgap (1.1–1.4 eV) [8–10], has a fairly high light absorption coefficient ($>10^{5}$ cm^{-1}) [11,12] and good charge carrier mobility (15 $cm^{2}V^{-1}s^{-1}$) [13,14]. It is important to stress that its the suitable bandgap enables a high absorption coefficient, making this material capable of absorbing more than 90% of light with a thickness of 1200 nm [14].

In addition, the layered structure of α-SnS results in a highly anisotropic material, meaning that the crystallographic orientation plays an important role in its properties. The material exhibits notable contrast when measurements are made along its axes, including carrier mobility [50], surface energy [51], ionization potential [51], and thermoelectric transport [52]. Although anisotropy can increase the complexity of device manufacturing, it can also present some benefits. The charge mobility along the layer direction is 10 times higher than in the perpendicular direction in a single crystal [9].

Recently, the cubic structure of the metastable π-SnS phase was reported [53]. The properties of this phase are distinct from the α-SnS. π-SnS has a large lattice constant of a = 1.1506 nm (see Figure 9) and a wider bandgap in the range 1.6–1.8 eV [54,55] when compared to the α-SnS phase (1.1–1.4 eV) [8,9,56]. π-SnS has been synthesized by several techniques such as chemical bath [57], spray pyrolysis [58], thermal evaporation [59], and atomic layer deposition [54]. As the α-SnS phase, the π-SnS phase has potential applications in various fields. It exhibits high performance in NIR photodetectors [60] and thermoelectric applications [61]. In terms of its application as an absorber layer in solar cells, π-SnS has demonstrated a current record efficiency of 1.28%, when deposited by chemical bath [62].

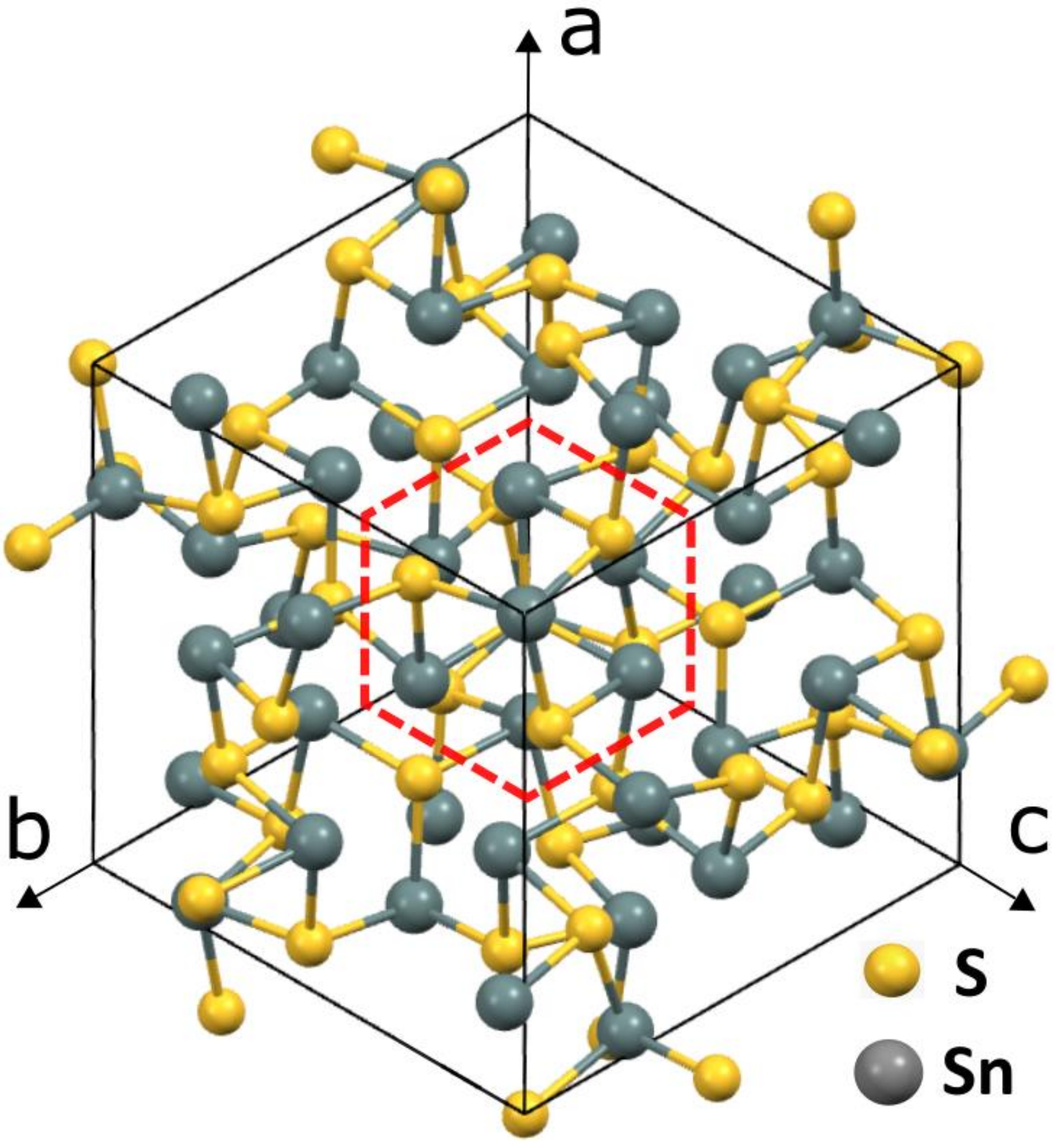

Figure 9. This figure provides a detailed depiction of the crystal structure and unit cells of the cubic π-SnS phase, including the unit cells represented by the black lines. The red dashed hexagon in the figure represents the SnS atoms in the [111] direction that are arranged to form a hexagon.

The use of SnS as a solar absorber layer in solar cell devices was first proposed in the late 1980s [63,64]. Figure 10 shows the maximum theoretical efficiency as a function of the bandgap for a single-junction solar cell calculated by Shockley-Queisser [45] for an AM 1.5 solar irradiance (depicted in Figure 2). In this figure, one observes that the range of the bandgap of α-SnS is at the maximum of this curve (grey region), with a theoretical maximum efficiency of ~ 32% [65]. Similar analyszes show that for the π-SnS the Shockley-Queisser efficiency limit is ~26% (red region in the graph) [5]. Therefore, this polymorphism presented by SnS is a rich subject for research and further studies are required to assess the full potential of both phases.

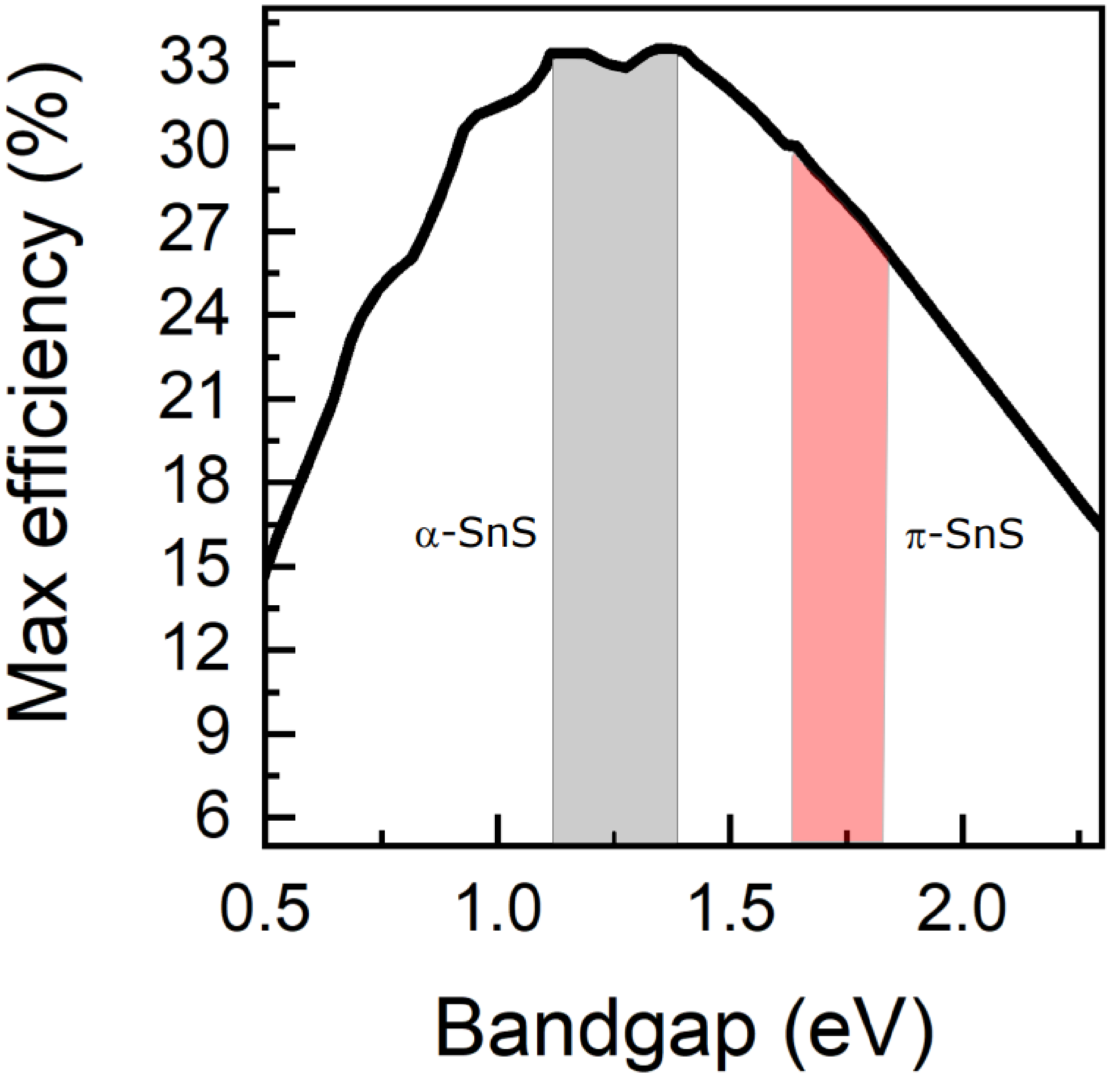

Figure 10. Theoretical efficiency as a function of band gap calculated by Shockley and Queisser with AM 1.5 solar irradiance. The shaded regions indicate the band gap range for bandgaps of α-SnS (grey – 1.1–1.4 eV) and π-SnS (red - 1.6–1.8 eV)

Sinsermsuksakul *et al.* [66] reported the development of one of the most efficient α-SnS-based solar cells, with an efficiency of 4.36%. This configuration is depicted in Figure 11. In this system, the solar cell was deposited on glass substrates coated with molybdenum metal by radio frequency sputtering. The SnS film was deposited by atomic layer deposition (ALD) using alternating doses of tin precursor vapor and a gas mixture of H_2S and N_2. The SnS surface was oxidized to form SnO_2. Zn(O, S) and ZnO were then deposited by ALD using diethyl zinc, H_2O, and a gas mixture of H_2S and N_2. ITO was deposited by radio frequency sputtering and the device is completed by depositing a Ni/Al metal contact.

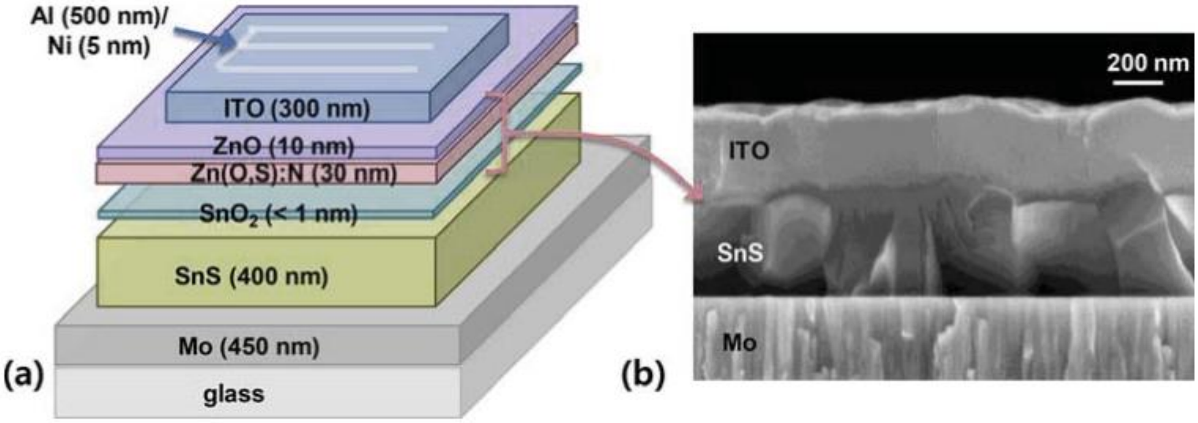

Figure 11. Solar cell based on α-SnS presented by Sinsermsuksakul et al. Figure from ref. [66].

Despite the significant efficiency of the α-SnS solar cell, ALD is a costly and complex approach. In addition, it has a slow deposition rate that greatly prolongs the device's manufacturing process. As an alternative, thermal evaporation is a relatively straightforward process that does not necessitate intricate machinery or precise regulation of deposition parameters. Moreover, the equipment involved in thermal evaporation is typically less expensive compared to that of ALD, making it a more cost-effective option for certain applications. Steinmann *et al.* [14] produced a device with a power conversion efficiency of 3.88% using thermal evaporation process, demonstrating that it is possible to produce SnS-based solar cells presenting good efficiencies in a simple way. Figure 12 presents the structure of the device.

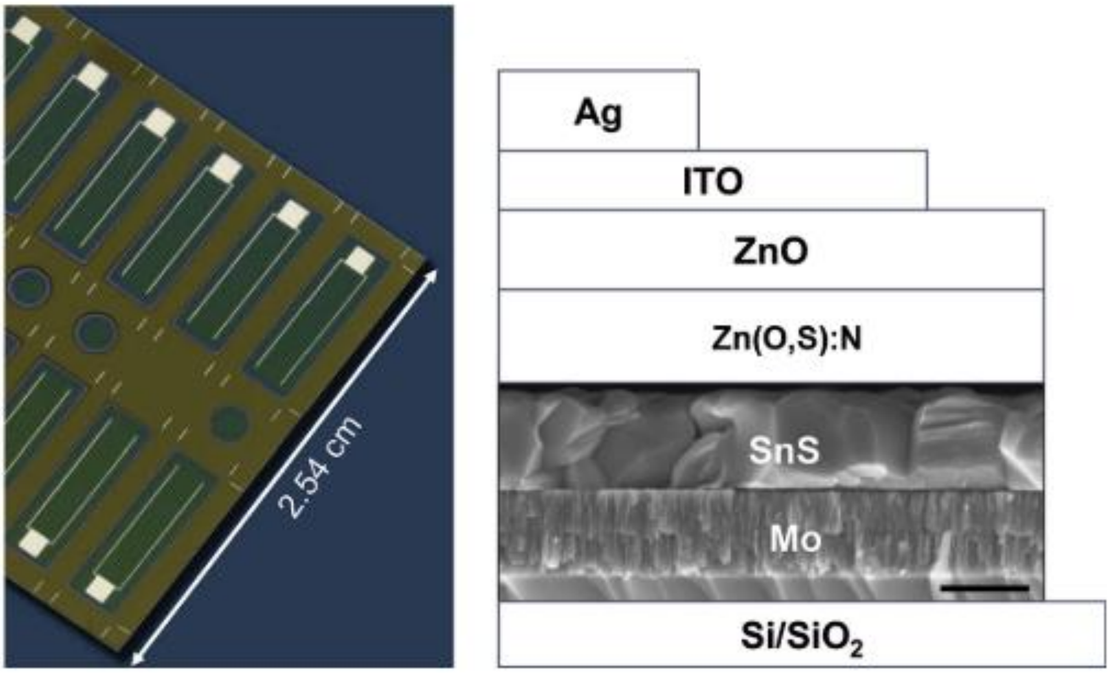

Figure 12. Solar cell based on α-SnS deposited using thermal evaporation by Steinmann et al. Figure from ref. [14].

More recently, Yun *et al.* [67] developed the current best-working α-SnS-based device with an efficiency of 4.8% (depicted in Figure 13). They fabricated a solar cell by solution process using rapid thermal treatment under Ar gas flow after spin coating a precursor solution of $SnCl_2$ and thiourea dissolved in dimethylformamide onto a nanostructured thin TiO_2 electrode. This process is also an alternative to the expensive ALD.

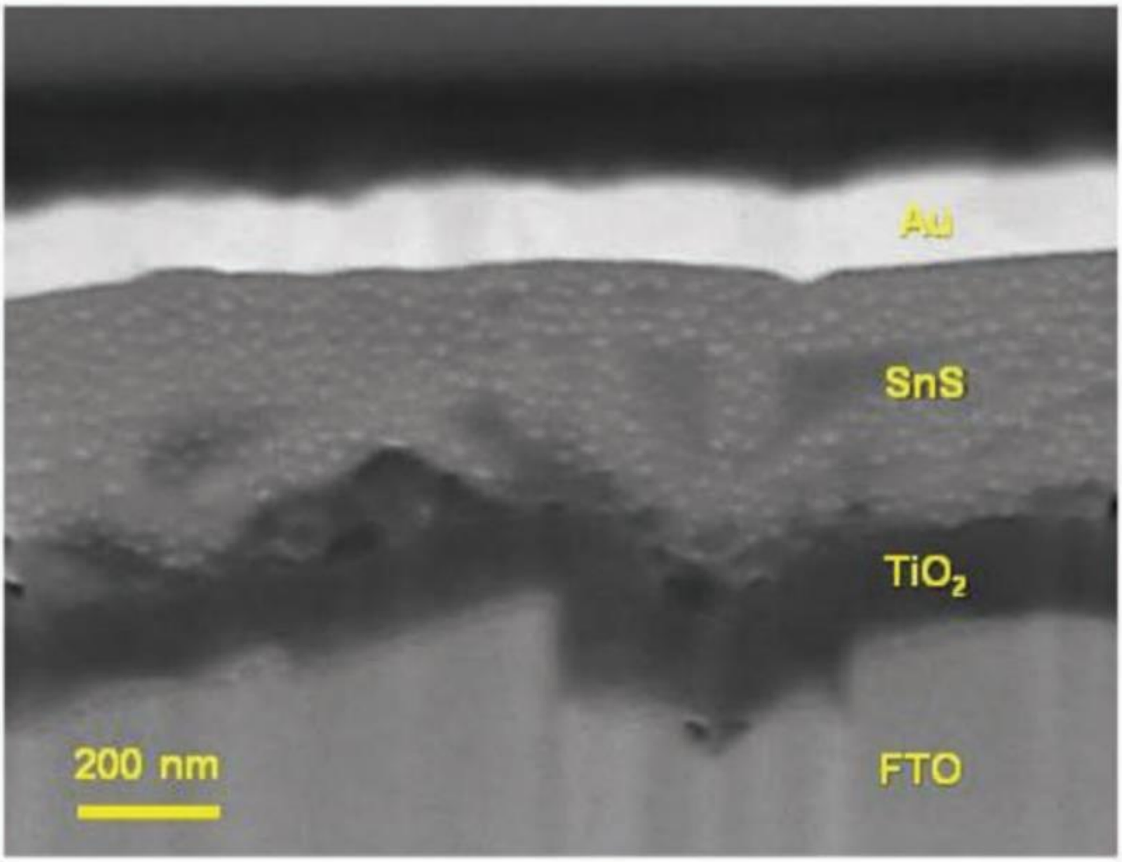

Figure 13. The best solar cell based on α-SnS presented by Yun et al. Figure from ref. [67].

The newly discovered metastable cubic π-SnS phase, presents current top-performing efficiency of 1.28% [62]. González-Flores *et al.* produced a solar cell by depositing π-SnS thin films on glass substrates coated with F-doped SnO_2 (SnO_2:F) as transparent conducting oxide (TCO) and CdS film as window layers (depicted in Figure 14). The chemical bath for depositing π-SnS thin films contained thioacetamide. The promising properties that SnS continues to show, together with low efficiencies (4.8%), are the main motivations for the first part of this study.

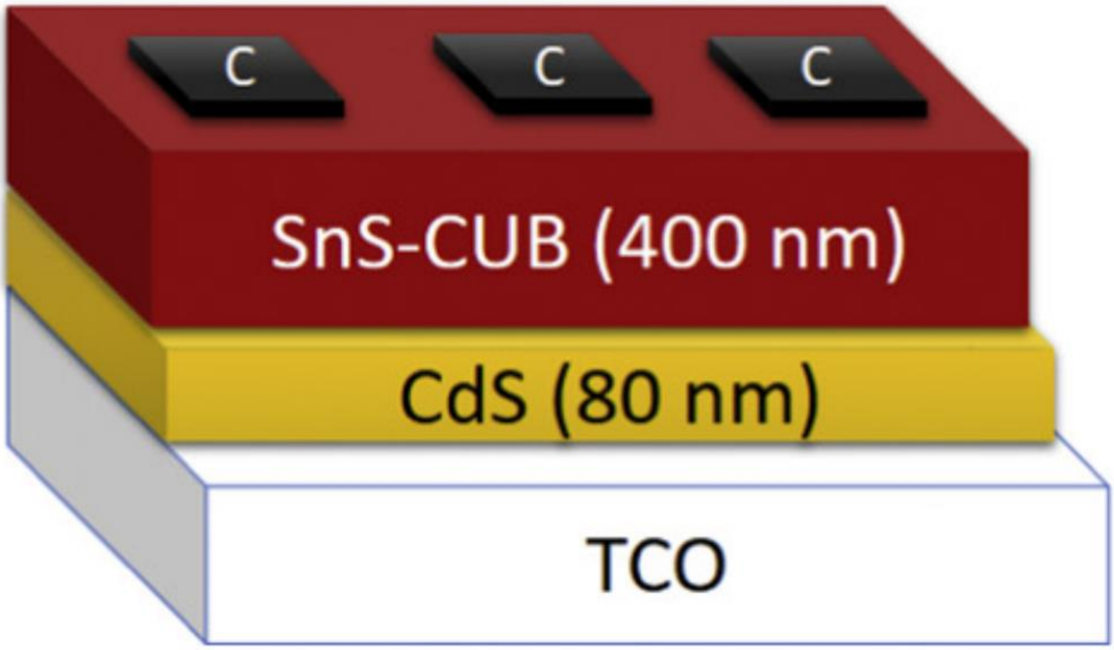

Figure 14. Schematic of π-SnS solar cell structure: TCO/CdS/SnS-CUB/SnS-ORT/C. Figure from ref. [62].

3.2 Germanium sulfide (GeS)

Similar to SnS, germanium monosulfide (GeS) is also part of the IV-VI family. It is an emerging material with suitable optoelectronic properties for solar cell applications, additionally presenting environmentally friendly and earth-abundant characteristics. GeS is usually synthesized as a p-type semiconductor and exhibits a bandgap at the end of visible region (1.6 – 1.7 eV) [15–17], large light absorption coefficient ($>10^4$ cm^{-1}) [17], and high carrier mobility (~ 86 $cm^2V^{-1}s^{-1}$) [18]. Theoretical studies indicate that single-junction GeS-based solar cells are situated in the spectral range of maximum efficiency (~ 34 %) for solar radiation if thermal losses are minimized. GeS has a puckered lattice with a = 0.430 nm, b = 1.047 nm, c = 0.364 nm lattice parameters and belongs to the Pbnm space group, analogous to α-SnS structure, as shown in Figure 15a. This atomic arrangement induces an anisotropic electronic response to polarized optical absorption [16,68], preferential photoconductivity [69], and multiferroic properties coupling ferroelectricity and ferroelasticity [70–72]. All these properties make GeS a promising material for tunable light emitters with the possibility of interlayer twist [19–21], enabling its use in visible light photodetectors [22–24] or as an absorber layer in solar cells [17]. GeS have been synthesized by methods with some extent of scalabilities such as chemical vapor deposition (CVD) [23,73], vapor phase deposition (VPD) [16] and colloidal synthesis [15]. A density functional theory (DFT) calculation of the GeS band structure, showing its direct gap at the Γ point is depicted in Figure 15b.

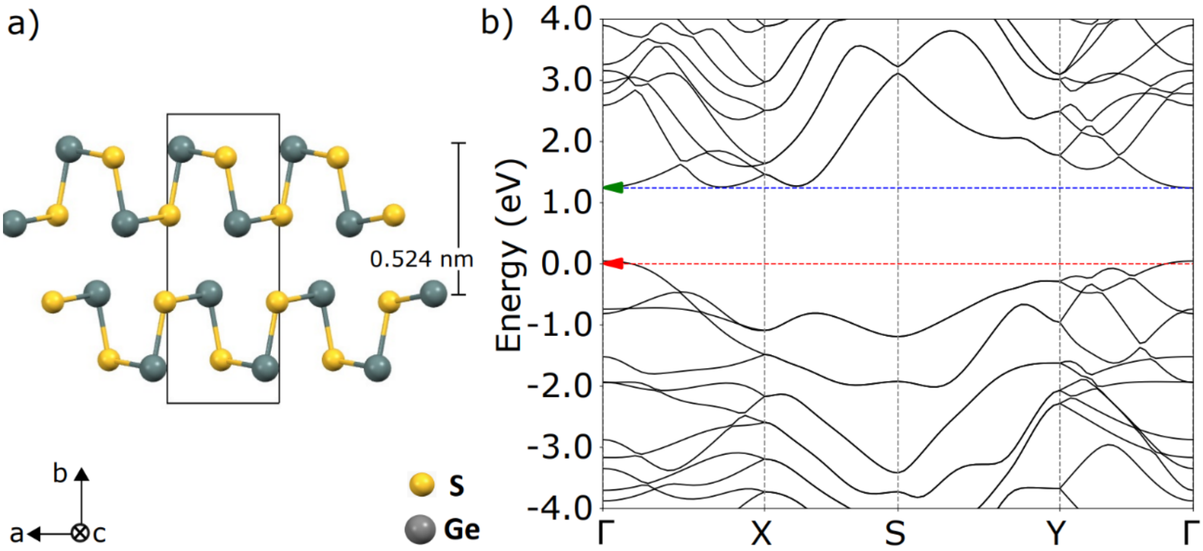

Figure 15. Crystal and band structure of GeS. a) Side view of the crystal structure and unit cell (black rectangle) of GeS. b) Band structure DFT calculations near the Fermi energy level for GeS, calculated by Rafael Reis. The green triangle indicate the bottom of the conduction band red triangle the top of the valence band, exhibiting a direct for GeS (theoretical gap values are underestimated with respect to experimental results).

Feng *et al.* [17] fabricated the first solar cell based on GeS as an absorber layer. GeS films were prepared by the close-space sublimation method that was employed as absorber layer in a device structure of glass/Mo/$MoSe_2$/GeS/CdS/i-ZnO/ITO/Ag (Figure 16). The best devices present a PCE of 1.36% under AM1.5G illumination and 3.6% under indoor illumination of 1000 lux. These devices show negligible PCE loss after storing in an ambient atmosphere at room temperature for 1500 h, demonstrating the great potential for photovoltaic applications.

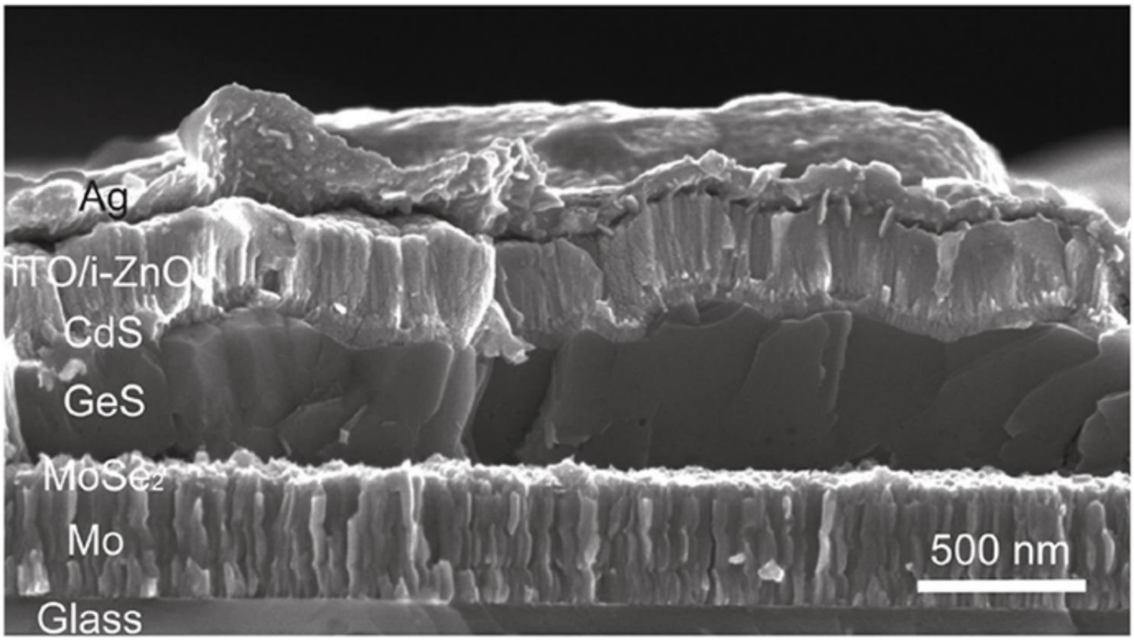

Figure 16. The figure shows a cross-sectional scanning electron microscope (SEM) image of the layers in a GeS solar cell. Figure adapted from reference [17].

3.3 Tin disulfide (SnS_2)

Tin disulfide (SnS_2), unlike GeS and SnS, is an n-type semiconductor with a hexagonal crystal structure with a = 0.364 nm, b = 0.364 nm, c = 0.589 nm lattice parameters and belongs to the P3m1 space group (Figure 17a). SnS_2 has a flexible wide-bandgap in the range of 1.8-2.9 eV, varying according to the deposition methods [25–29]. This compound is synthesized using inexpensive elements, simple controllable chemical stoichiometry, and consistent environmental stability. SnS_2 has a plethora of potential applications ranging from diodes [30], photodectors [31], gas sensors [32], batteries [33], supercapacitors [34], field effect transistors [35], and buffer layer for heterojunction in solar cells [29]. The synthesis of SnS_2 can be achieved by different processes, such as CVD [74], wet chemical processes [29] and spray pyrolysis [75]. The SnS_2 calculated (DFT) band structure is shown in Figure 17b, in which one can observe the occurrence of an indirect gap.

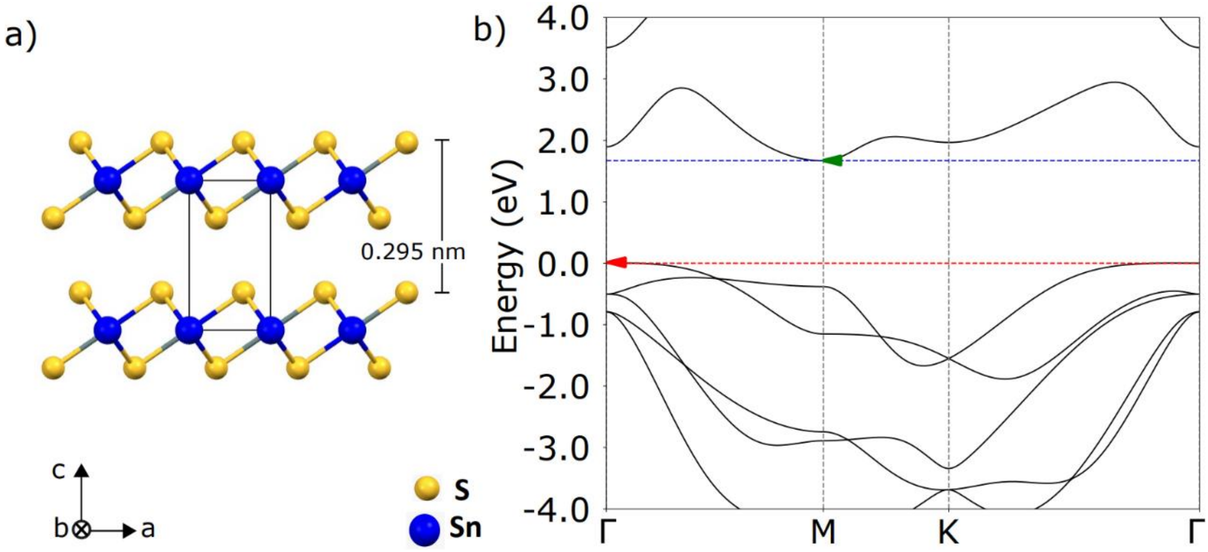

Figure 17. Crystal and band structure of SnS_2. a) Side view of the crystal structure and unit cell (black rectangle) of SnS_2. b) Band structure DFT calculations near the Fermi energy level for SnS_2, calculated by Rafael Reis. The green triangle indicate the bottom of the conduction band red triangle the top of the valence band, exhibiting an indirect for SnS_2 (theoretical gap values are underestimated with respect to experimental results).

The broad capabilities of SnS_2 turn it into a suitable candidate for the replacement of hazardous materials in several devices. For solar cells, the use of buffer layers with a bandgap of approximately 2.5 eV and partial transparency to visible light usually leads to material choices such as In_2S_3 [76,77], ZnS [78–80], ZnO [81,82], TiO_2 [83,84], Zn(O, S) [14], ZnMgO [85] and the CdS [17,86,87] (the most used). These compounds present production cost drawbacks related to their vacuum-based synthesis techniques, which consequently limits scalability. Particularly for cadmium sulfide (CdS), toxicity is a severe restriction for the production and waste disposal of devices.

Recent studies present SnS_2 as a buffer layer for $Cu(In,Ga)Se_2$(CIGS) solar cell devices with similar performance to CdS [29]. In this work, Gedi *et al.* fabricated a solar cell with SnS_2 presenting an open circuit voltage (V_{OC}) of 0.41 V, short circuit current density (J_{SC}) of 25.67 mA cm^{-2}, fill factor (*FF*) of 49%, and conversion efficiency (η) of ~ 5.1% (see Figure 18). All values are comparable to CdS-based devices, with an efficiency of ~ 7.5%. Such a condition points to SnS_2 as an interesting alternative for Cd-free solar cell production.

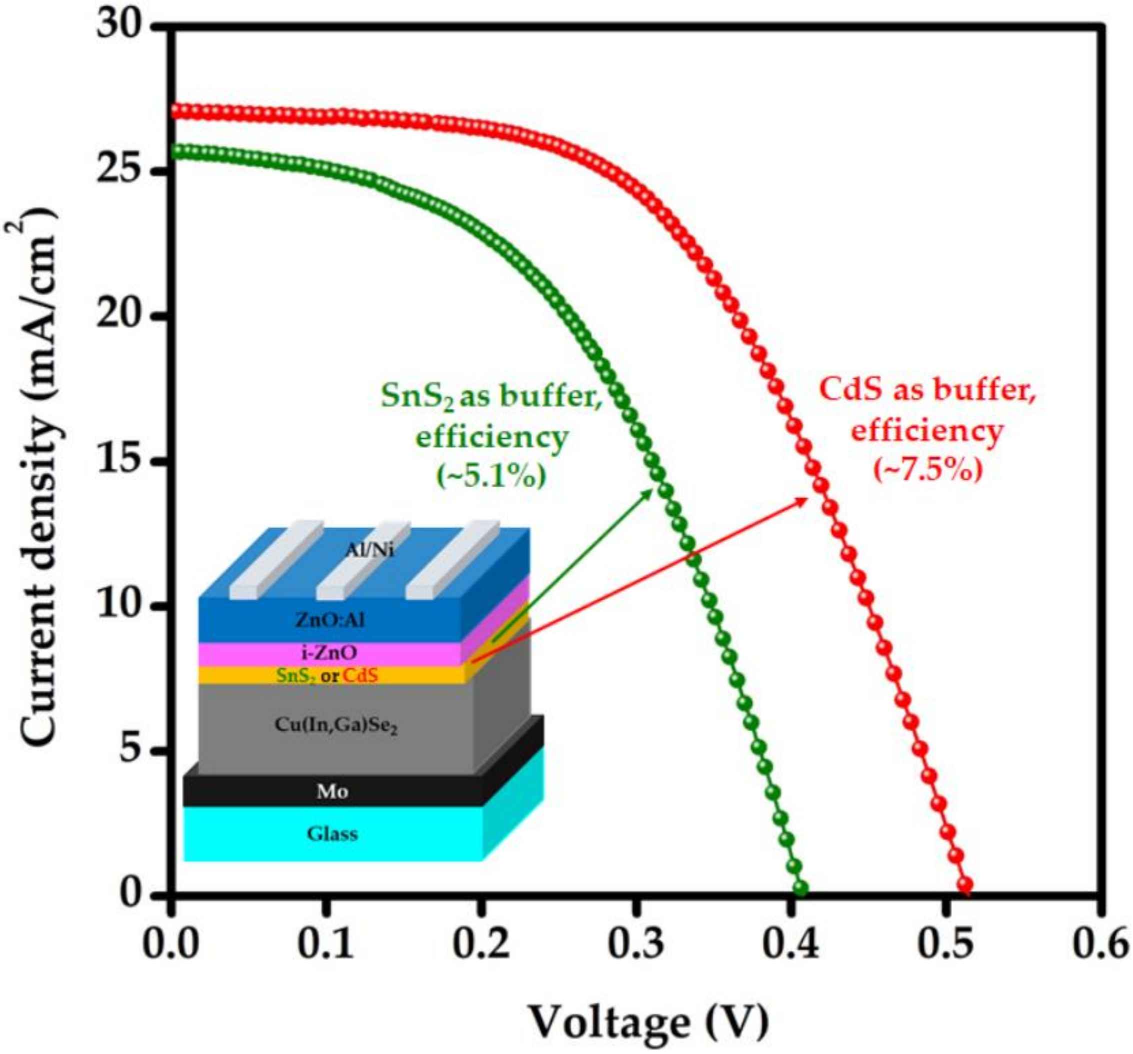

Figure 18. J-V curves of CIGS devices with conventional CdS and SnS_2 buffer layers. The CdS cell demonstrates an efficiency of 7.5%, while the SnS_2 cell exhibits an efficiency of 5.1%. The performance of the SnS_2 cell is comparable to that of the CdS cell. This figure was adapted from ref. [29].

4. Experimental methods

4.1 Vapor phase deposition

Vapor phase deposition is a method of synthesizing films and isolated structures that uses a simple experimental setup and in which the material deposition rate is reasonably low. The procedure consists of placing the precursor powder in a ceramic boat inside a vacuum chamber and heating it so that it sublimates. Subsequently, the material vapor is carried downstream by inert gas and deposited over the substrate that is at a lower temperature compared to the source. Once the deposition takes place, the following processes can occur:

1) Adsorption: gas molecules that collide with the substrate surface can be adsorbed when they dissipate part of their momentum via electrostatic interaction. On the other hand, very energetic molecules can be reflected from the substrate surface.
2) Diffusion: weakly adsorbed molecules can use their residual momentum to diffuse along the substrate surface. Some of them can gain enough energy during the migration and be desorbed from the substrate surface.
3) Nucleation: adsorbed molecules can interact with each other forming nucleation centers.
4) Condensation: nucleation centers can interact with each other forming flakes and films, as shown in Figure 19.

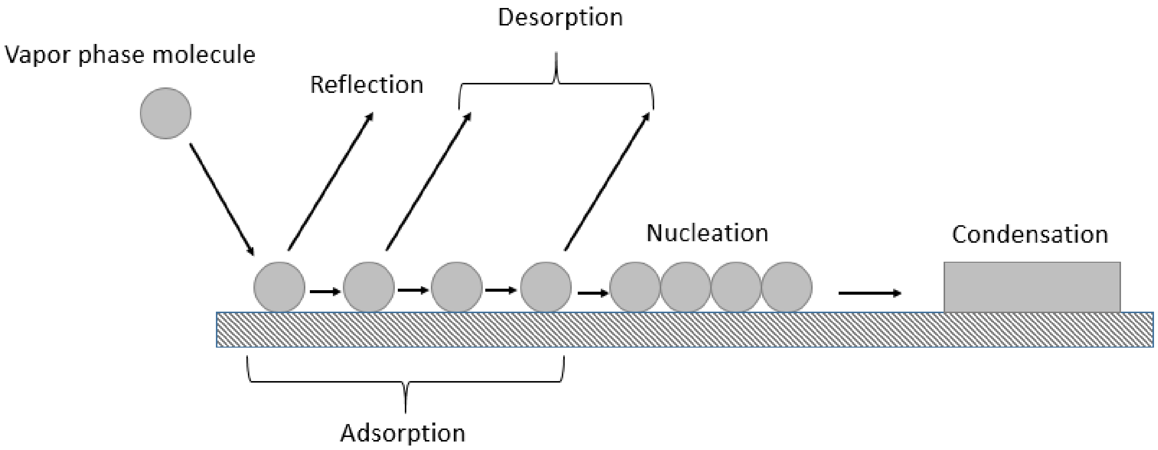

Figure 19. The figure demonstrates the vapor phase deposition on a substrate, including the stages of adsorption, diffusion, nucleation, and condensation, in a sequential manner.

To synthesize the structures used in this thesis, the purified material powder was placed in an alumina boat at the center of the furnace's hot zone (zone 1 - see Figure 20a), while the substrates were placed downstream from the powder source. The tube reactor was then connected to a vacuum pump, and ultrapure argon was injected at a flow rate of 200 sccm for 20 min to purge the chamber. Afterward, the argon flux was reduced, leading to a decrease in pressure, and the furnace was heated to reach the synthesis temperature. In this example recipe, the temperature ranged from approximately 550°C to 520°C along the substrate in the longitudinal axis direction (see Figure 20a). The system was heated for 10 min while the vapor was carried downstream and deposited on the substrate. Finally, the system was naturally cooled to room temperature. Figure 20 shows a schematic of the synthesis process.

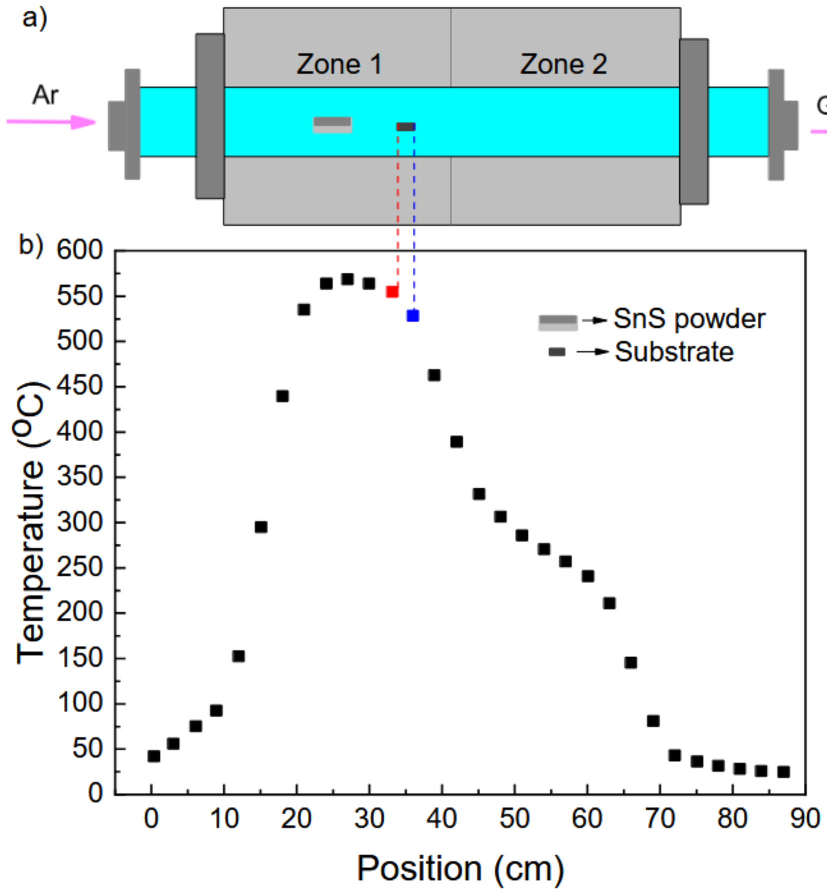

Figure 20. a) Schematic representation of the experimental setup for growth of SnS samples. The vertical red and blue dashed lines indicate the regions where flat and spiral platelets appear, respectively. b) Measured temperature profile of the furnace along its horizontal axis for conditions used in this work.

The described process relies on several experimental parameters to determine or influence the morphology and evolution of the synthesized structures. These parameters include vapor phase supersaturation, source material and substrate temperature, temperature gradient in the tube furnace, distance between the source material and the substrate, furnace heating rate, gas flow rate, inner diameter of the ceramic tube, and starting material.

The vapor phase supersaturation and the surface energy of the material's growth planes, play a dominant role in the evolution of structure growth. The rate of crystal growth is determined by the supersaturation of vapor phase atoms and molecules, while the final structure of the crystal is determined by the surface energy of the growing surfaces, among other parameters. Understanding the morphological evolution of nanostructures and achieving the desired nanostructures in a controllable manner relies on a fundamental understanding of these factors. Supersaturation can be defined as [67]:

$$S = \frac{p - p_0}{p_0}, \tag{2}$$

where values p and p_0 represent the actual gas pressure and the equilibrium pressure between the solid and gas phases of the material, respectively.

The temperature profile in Figure 20b reveals that in the substrate region closer to the source (defined by the red square), where the temperature gradient was minimal, the sublimated material's vapor pressure approached the equilibrium vapor pressure, leading to a supersaturation close to zero and growth near thermodynamic equilibrium. Consequently, the low nucleation rate of SnS platelets resulted in their orthorhombic shape, consistent with Wulff's theory [88]. Conversely, in the region further from the source (defined by the blue square), a significant temperature gradient led to a sudden increase in supersaturation (due to a decrease in equilibrium vapor pressure), resulting in high nucleation rates, material deposition, and the formation of structures with random orientation and undefined shapes. The growth under large gas-phase supersaturation occurred far from thermodynamic equilibrium, necessitating the consideration of kinetic effects such as gas phase diffusion and surface diffusion. Figure 21 depicts scanning electron microscopy images of regions on the substrate, highlighting the described characteristics at varying distances from the powder source.

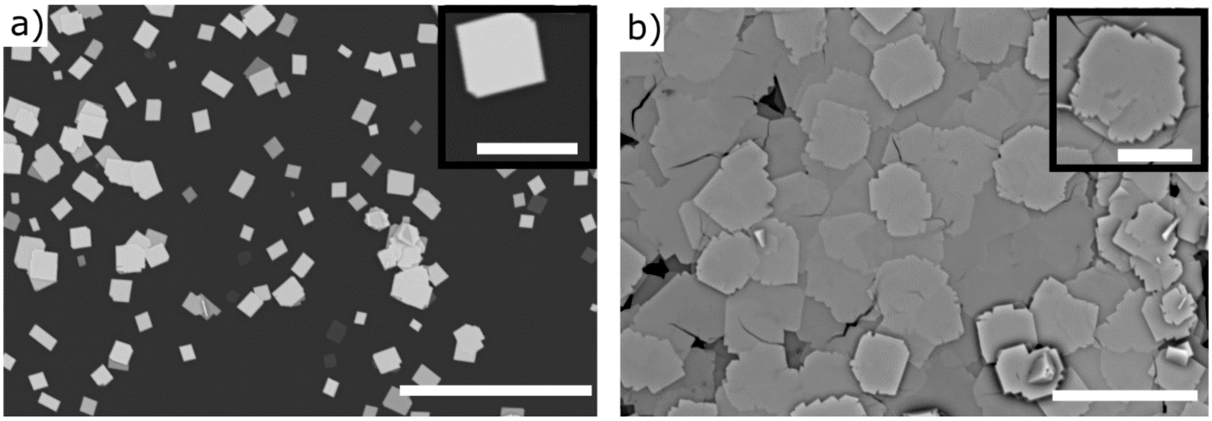

Figure 21. The figure shows scanning electron microscopy images of different regions of the substrate. a) Representing a closer view (regular platelets) and b) representing a further view (undefined shapes platelets) from the powder source, respectively.

The vapor pressure of the source material is determined by its temperature, with pressure increasing exponentially as the temperature rises. As the vapor travels downstream with the carrier gas towards the substrate, a local supersaturation builds up, which is higher with higher heating temperatures. Thus, the morphology of the synthesized structures is affected accordingly. The temperature at the substrate and the temperature gradient also affect the supersaturation profile and hence the morphology. The distance between the source material and the substrate determines the local supersaturation and temperature. Additionally, the heating rate may influence the initial nucleation process, with a higher heating rate allowing for homogeneous nucleation and lower dispersity of morphology, while a lower heating rate generally results in higher dispersity.

The supersaturation profile is significantly impacted by the gas flow rate and the inner diameter of the tube. A higher gas flow rate and smaller inner diameter will cause the maximum supersaturation to shift downstream from the source material, thereby altering the structure's morphology at a fixed position on the substrate.

It is widely known that materials with nanometer-scaled sizes exhibit a lower melting temperature [89]. Therefore, utilizing nanomaterial as the source material can increase the heating temperature and subsequently alter the supersaturation profile, leading to changes in the final morphology of the structure. While other factors may also affect the morphology in specific situations, they are not relevant to the current study.

4.2 Raman spectroscopy

In Raman spectroscopy, a non-destructive interaction of a monochromatic light beam (usually a laser) with the investigated material causes molecular vibrations that result in a shift in the frequency of the scattered radiation. This technique, commonly used to determine the vibrational modes of molecules, provides a structural fingerprint of the phase, polymorph, crystallinity, and molecular interactions of the studied material.

The elastic scattering light (Rayleigh scattering) is at the same frequency as the incident light and does not provide useful information. On the other hand, Stokes shift occurs when the frequency of the inelastically scattered light is lower than that of the incident light. In this case, the vibrational state of the target material is more energetic than its initial state. Differently, the anti-Stokes occurs when the frequency of the inelastically scattered light is shifted to a higher value compared to incident light, and consequently, the vibrational state of the material is less energetic than the initial state. In all these cases, the energy of the system is conserved. The schematics of the Raman scattering are shown in Figure 22.

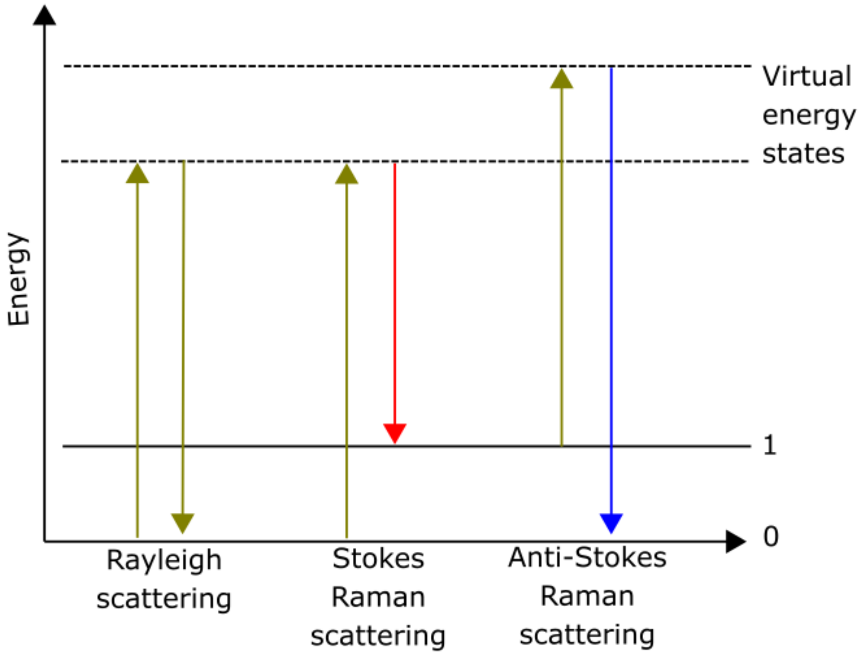

Figure 22. In Raman spectroscopy, the interaction between matter and light causes the excitation of a molecule from its ground state to a virtual excited state, followed by the relaxation to a higher vibrational state. This process can result in three types of scattering: Rayleigh, Stokes Raman, and anti-Stokes Raman scattering. The energy excitation-level diagram presented in this figure shows the states involved in Raman spectroscopy, including the ground state, virtual excited state, and vibrational states involved in Rayleigh, Stokes Raman, and anti-Stokes Raman scattering.

Figure 23a shows vibration diagrams for A_g and B_{3g} SnS modes and Figure 23b depicts the corresponding peaks in the Raman spectra for films and platelets located at 95, 160, 189, and 218 cm^{-1}. The A_g (218 cm^{-1}) mode corresponds to the “NaCl” type vibration; A_g peaks (95 cm^{-1}, 189 cm^{-1}) are “waving” and “breathing” modes; and B_{3g} (160 cm^{-1}) is a “NaCl” type vibration along the b-axis direction, as presented in reference [90]. This thesis utilized Raman spectroscopy with a Witec Alpha300 spectrometer, which employed a 532 nm laser passed through a 100x objective lens and operated at approximately 0.4 mW power.

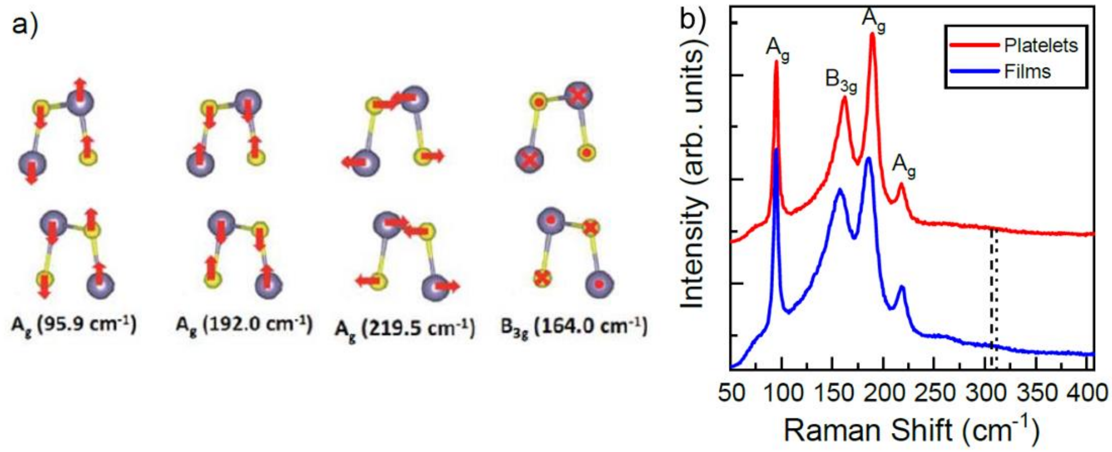

Figure 23. a) Vibration diagrams of Ag modes and B_{3g} modes. Figure from ref. 89. b) Raman spectra of SnS platelets (red line) and films (blue line). Figure from ref. [88].

4.3 Scanning electron microscopy (SEM) and energy-dispersive X-ray spectroscopy (EDS)

Scanning Electron Microscopy (SEM) is a powerful imaging technique used to observe the surface morphology of a sample at high magnification. SEM works by scanning a focused beam of electrons across the surface of the sample, and detecting the emitted electrons that interact with the sample's surface. These emitted electrons are then used to generate a detailed, high-resolution image of the sample's surface.

To put it briefly, the standard scanning electron microscope comprises a tower that emits electrons through thermionic or field emission from a tungsten or lanthanum hexaboride (LaB6) filament (cathode) at its top. After being accelerated and passing through an anode, the electron beam is focused by condenser lenses that align it with the objective aperture. The objective then adjusts the beam focus before it reaches the sample. Figure 24 shows the SEM column and its main components in an illustration.

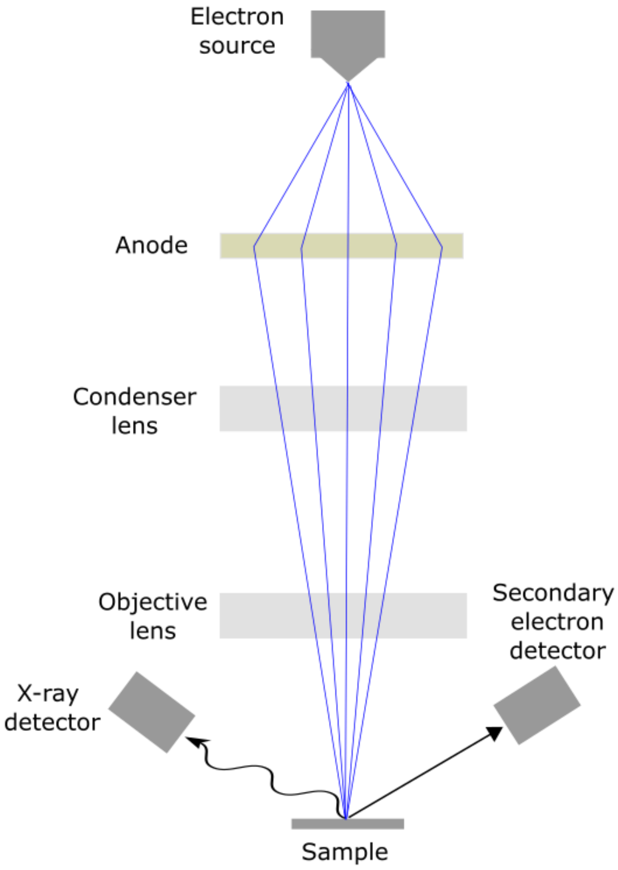

Figure 24. This schematic diagram illustrates the essential components of a scanning electron microscope (SEM), including an electron source, anode, condenser lens, objective lens, and x-ray and secondary electron detectors. The sample interactions with the electron beam are also depicted, which can include secondary electrons, and characteristic X-rays emitted from the sample.

When the beam interacts with the sample, it emits various types of radiation, including bremsstrahlung X-rays, characteristic X-rays (fluorescence), electromagnetic radiation in the infrared, visible, and ultraviolet regions, as well as secondary electrons, backscattered electrons, and Auger electrons. In scanning electron microscopy, the most significant signals are the backscattered electrons (which collide elastically with the surface atoms of the sample) and the secondary electrons (which result from inelastic collisions between the primary electrons and the sample atoms). The secondary electron mode mainly reveals the topography contrast of the sample surface, while in the backscattered electron mode, images are produced based on the mass contrast between the elements on the surface. Heavier atoms are more likely to undergo backscattering interactions with the electrons and thus appear brighter in SEM images. The SEM detector can be switched between the secondary electron and backscattered electron modes, or the SEM system can be equipped with multiple detectors.

In addition, EDS detects the energy of the X-rays emitted from atoms in the sample, which are excited by the electron beam. Excited electrons tend to revert to their initial states and release a photon with energy equal to the difference between the excited and initial states. Measuring the energy of these emitted X-rays allows for determination of the type and concentration of elements, even when unknown. With advanced EDS detectors, like wavelength-dispersive spectrometers (WDS), the energy resolution can reach ~5 eV [91].

Figure 25 illustrates an example of a secondary electron image, a backscattered electron image, and an EDS spectrum. A secondary electron image (Figure 25a) and a backscattered electron image (Figure 25b) of the letter-printed part on a name card are displayed. The ink of the letters contains heavy metals, resulting in a brighter contrast in the backscattered electron image compared to the fiber part of the name card (compositional contrast). The secondary electron image does not exhibit compositional contrast. It is important to note that the surface of this specimen has been carbon-coated to prevent electric charging. Figure 25c shows the EDS spectrum that displays the concentration of Sn and S in a SnS sample. This thesis utilized Scanning Electron Microscopy (SEM) was performed using a Hitachi TM4000Plus microscope working at 15 KeV. Energy-dispersive X-ray (EDS) spectra, collected in the same equipment, identified the stoichiometry of the produced samples.

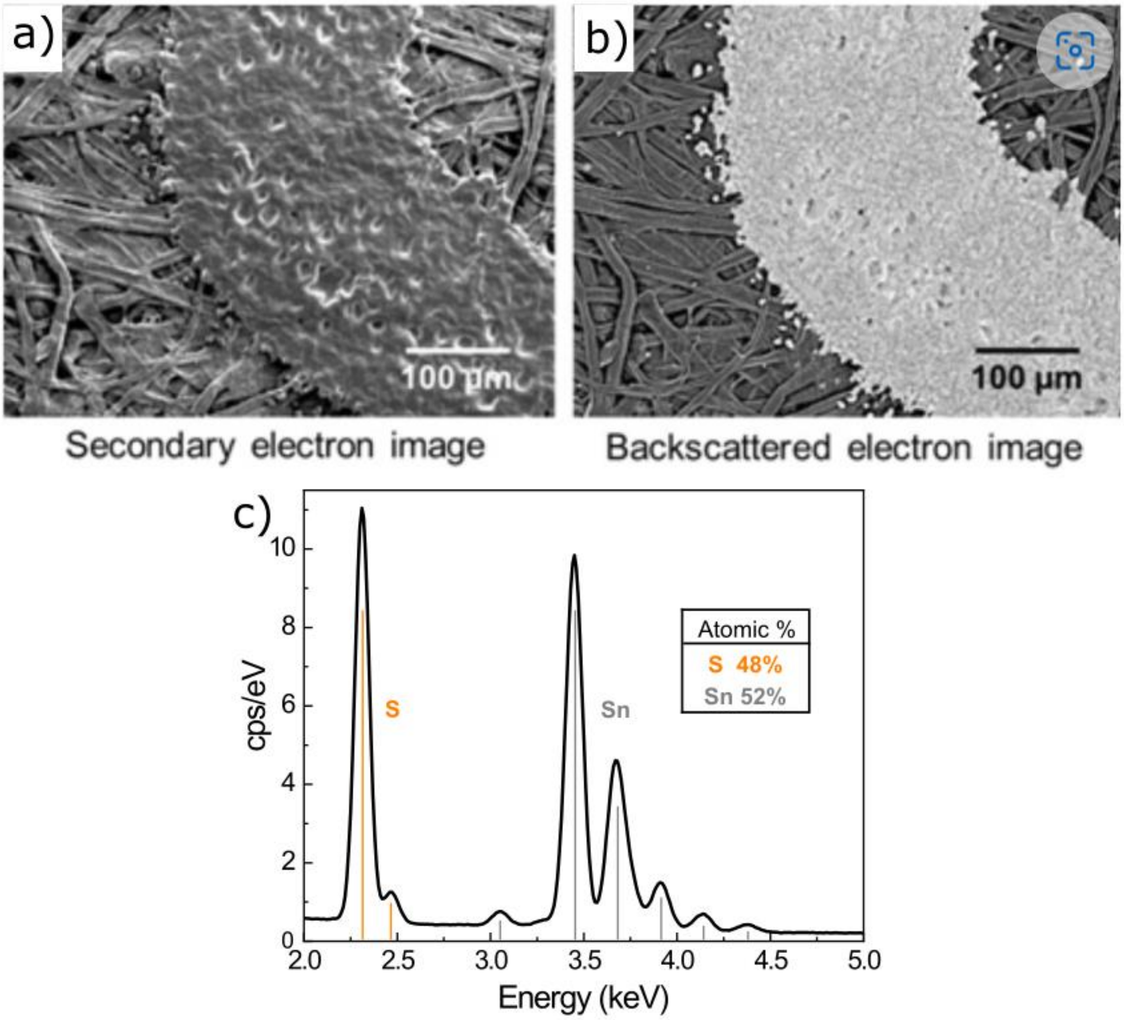

Secondary electron image

Backscattered electron image

Figure 25. The image a) shows a secondary electron view, while the one on b) displays a backscattered electron view of the lettering section of a carbon-coated name card (located at the center of both images)(see Reference https://www.jeol.com/words/semterms/20190129.113542.php#gsc.tab=0). c) EDS spectrum SnS platelets with Sn: S atomic ratio close to 1:1.

As illustrated in Figure 26, secondary electrons possess very low energy, typically below 50 eV, with a peak distribution of 3-5 eV. Consequently, only secondary electrons within the top 50 nm of the surface can leave the surface and reach the detector. In contrast, backscattered electrons have much higher energy, nearly equal to the incident energy, and interact with a region up to 3 µm in diameter, resulting in a significant reduction of the technique's spatial resolution. The typical spatial resolution of SEM is approximately 50 nm in the secondary electron mode and greater than 100 nm in the backscattering electron mode.

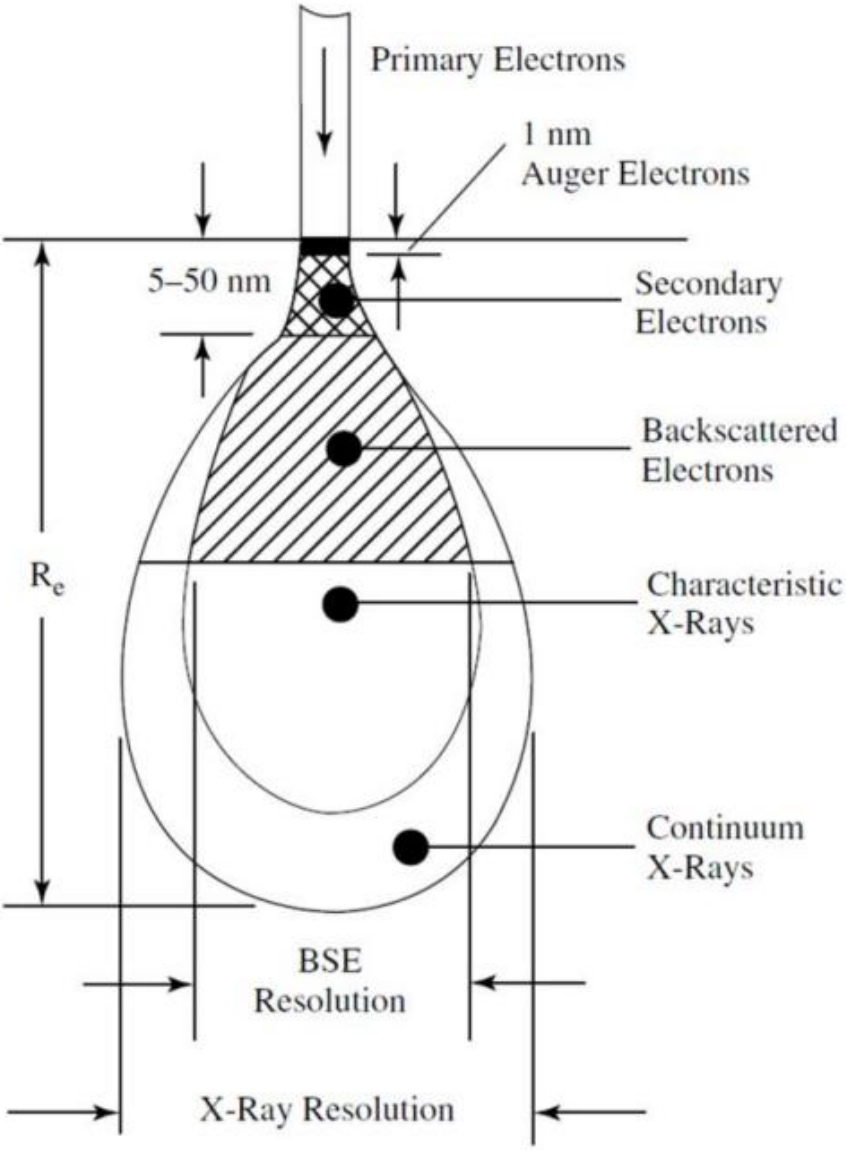

Figure 26. The figure shows the range and spatial resolution of secondary electrons, backscattered electrons, and X-ray emission in an electron microscopy system. Figure from ref. [92].

X-ray diffraction (XRD)

X-ray diffraction is a powerful non-destructive technique used for characterizing crystalline materials. It provides information about structures, phases, and crystal orientation, among other properties. According to Bragg's treatment, a plane-wave of X-rays, which is incident on a single Bravais lattice, is reflected from a set of parallel lattice planes, as depicted in Figure 27. Bragg's law describes the diffraction of X-rays by the sample, the reflections from each of the planes of a certain family will interfere constructively when the following condition is met:

$$2dsin\theta = n\lambda\,, \tag{6}$$

where *d* is the perpendicular distance between pairs of adjacent planes, θ is the angle of incidence, λ is the wavelength of the beam, and *n* denotes an integer number, known as the order of the reflection.

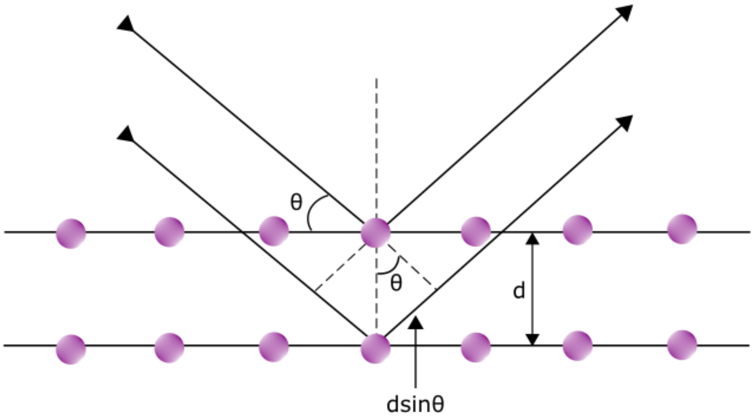

Figure 27. X-ray diffraction (XRD) works on the basis of Bragg's law, which states that a crystal lattice plane will diffract X-rays at an angle ϑ if the following condition is met: nλ = 2d sinϑ, where n is an integer, λ is the wavelength of the X-ray, d is the interplanar spacing of the crystal lattice, and ϑ is the angle of incidence of the X-ray beam on the lattice plane. This figure illustrates the geometrical condition for diffraction from lattice planes in XRD.

The powder method is the most commonly used technique for crystallographic XRD characterization, particularly for polycrystalline materials. In one version of this method, illustrated in Figure 28, the sample being analyzed remains stationary while the X-Ray source (monochromatic) and the counter rotate at an angle of θ each. As the angle meets Bragg's condition for one of the crystal planes, the counter detects a sharp peak of radiation. The resulting peaks on the 2θ axis represent different crystallographic planes or crystallite orientations. The peak amplitude corresponds to the number of grains or crystallites in the corresponding orientation with respect to the source.

By analyzing the precise angles at which radiation peaks are identified, it is possible to deduce both the texture of the material (preferred grain orientations) and the lattice constant. The lattice constant can be used to approximate the average residual strain, and consequently, the stress of the material. In Figure 29, an exemple of X-ray diffraction pattern of the SnS precursor powder is presented, both before and after a heat treatment. The pattern shows that the undesired phase was eliminated, and the treated material now only contains the SnS phase, which corresponds to ICSD number 52108. The phases of the SnS powder and the crystallographic orientation of the SnS platelets were analyzed by x-ray diffraction (XRD, Empyrean) with Cu Kα radiation using a θ/2θ scan.

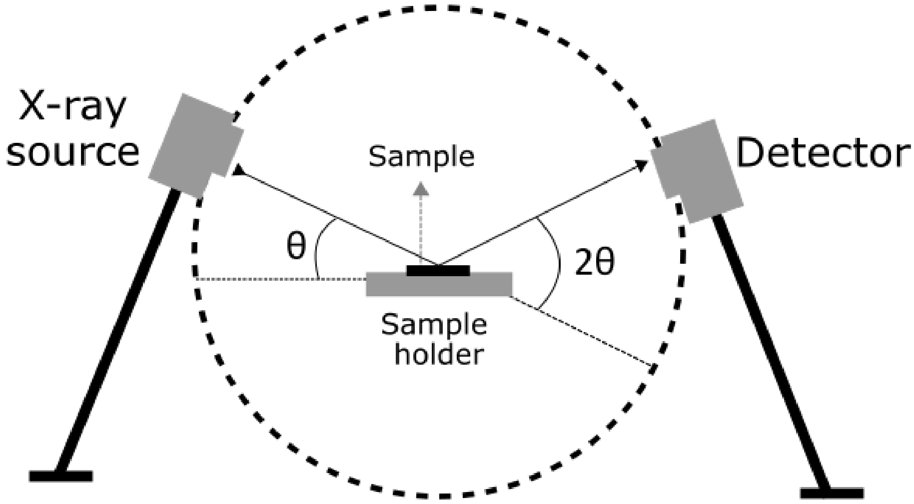

Figure 28. A simplified X-ray diffraction measurement schematic showing the X-ray source, sample, detector, and the angles of incidence (θ) and diffraction (2θ).

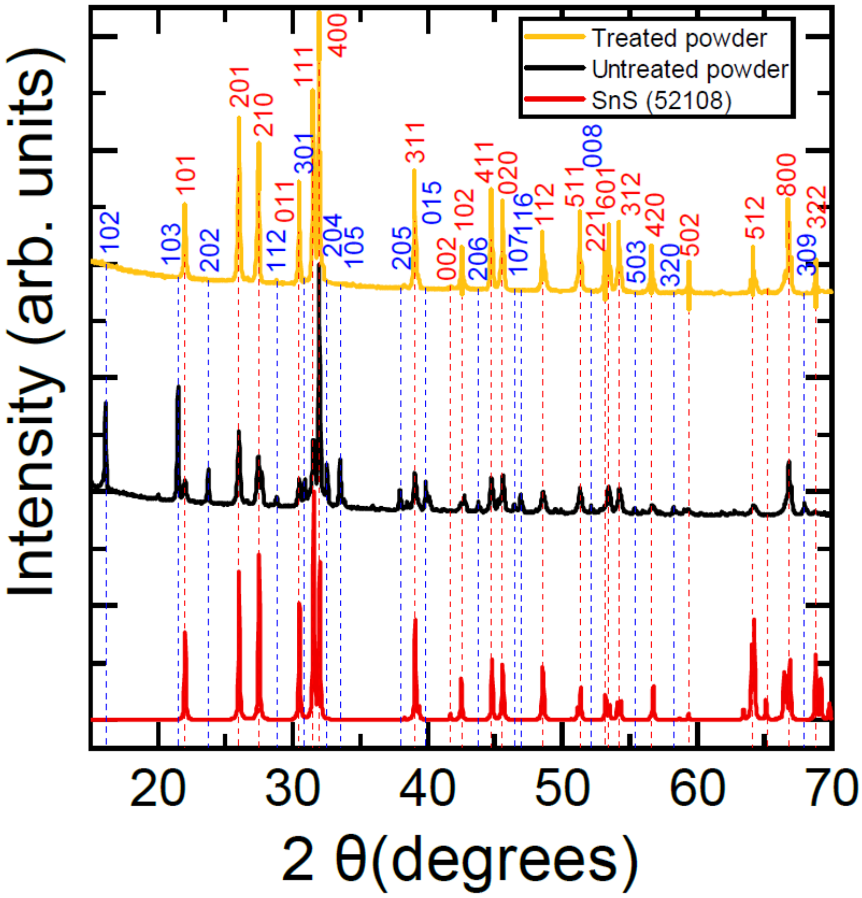

Figure 29. XRD data of SnS heat treated powder (yellow), untreated powder (black) and XRD data for SnS taken from ICSD number 52108. The vertical red dashed lines indicate the peaks for SnS and the blue dashed lines present peaks for Sn_2S_3.

4.4 Scanning tunneling microscopy and spectroscopy (STM/STS)

Binnig and Rohrer developed the scanning tunneling microscope in 1981 [93], which is a powerful experimental tool in surface science analysis. Based on the quantum phenomenon of tunneling, this technique allows the imaging of a surface through the variation of the tunneling current between a sharp conducting tip and the investigated conducting sample.

Tunneling is a quantum phenomenon in which a particle can propagate in a region where the potential barrier that is higher in energy than the particle's energy. According to classical mechanics, a particle with energy lower than the potential barrier cannot propagate through it. In the quantum regime, on the other hand, particles are described by Schrödinger's equation and have wavelike properties and, thus, can be associated with a wavefunction that must be continuous at the barrier limits. This wave exhibits an exponential decay inside the barrier, indicating that there is a finite probability of the particle tunneling through the barrier. Figure 30 summarizes the quantum tunneling through a potential barrier.

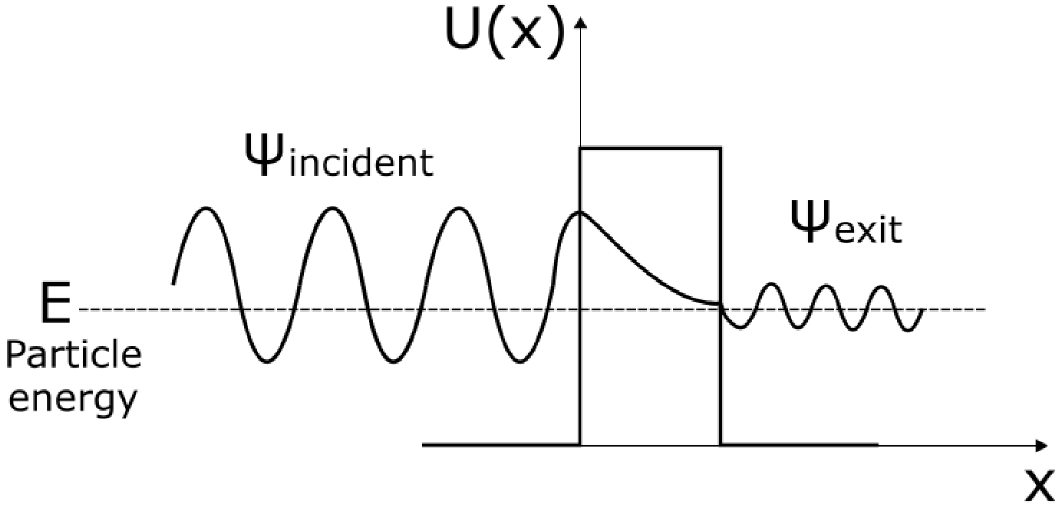

Figure 30. The figure illustrates the quantum tunneling effect, which is a quantum mechanical phenomenon that occurs when a particle is able to pass through a potential barrier despite not having enough energy to do so classically. This effect arises due to the exponential decay of the wave function of the particle within a one-dimensional potential barrier, which allows the particle to extend into the classically forbidden region. The figure provides a visual representation of this concept, showing how the wave function of the particle is damped within the potential barrier and how it extends beyond the barrier, indicating the possibility of the particle tunneling through the barrier.

To extend this quantum phenomenon to the STM, the operation of the microscope, used in this thesis, is described as follows: a sharp conducting tip, usually made of W or Pt-Ir, is connected to three piezoelectric motors in orthogonal directions *(x, y,* and *z)*. These motors, made of piezoelectric materials, contract or expand depending on the application of a voltage. This property makes this system able to scan the sample along its surface and vary its *z*-position (see Figure 31a). Once the tip and the sample are sufficiently close and in thermodynamic equilibrium, their Fermi levels must align (see Figure 32a). Electrons attempting to travel from sample to tip (or vice versa) will not succeed, due to the Pauli Exclusion Principle. Despite the tip and the sample Fermi levels being exactly aligned, there are no empty states on either side available for electrons to tunnel. If a voltage is applied to the tip (or sample), its energy levels will be shifted. Then the electrons can tunnel from the occupied states of the sample to the unoccupied states of the tip (see Figure 32b). The tunneling process thus depends on the available unoccupied electron states in the underlying sample in the energy window of the applied voltage. At negative tip bias, the detected current arises from the electrons that tunnel from occupied states of the tip into unoccupied states of the sample; at positive tip bias the electrons tunnel from occupied states of the sample into unoccupied states of the tip. Finally, a feedback loop system is required to monitor the distance between the tip and the sample, in order to maintain the tunneling current constant (constant current mode). If the tunneling current is greater (smaller) than a reference value, the feedback system, drives the tip away (closer) from the sample surface, thus decreasing (increasing) the tunneling current, to keep it constant (see Figure 31b). The process will result in the mapping of the sample's surface into topographic images. These images will be presented in a color-code that reflects a combination of both height and electronic variations. An example of an STM image of a SnS platelet is presented in Figure 33.

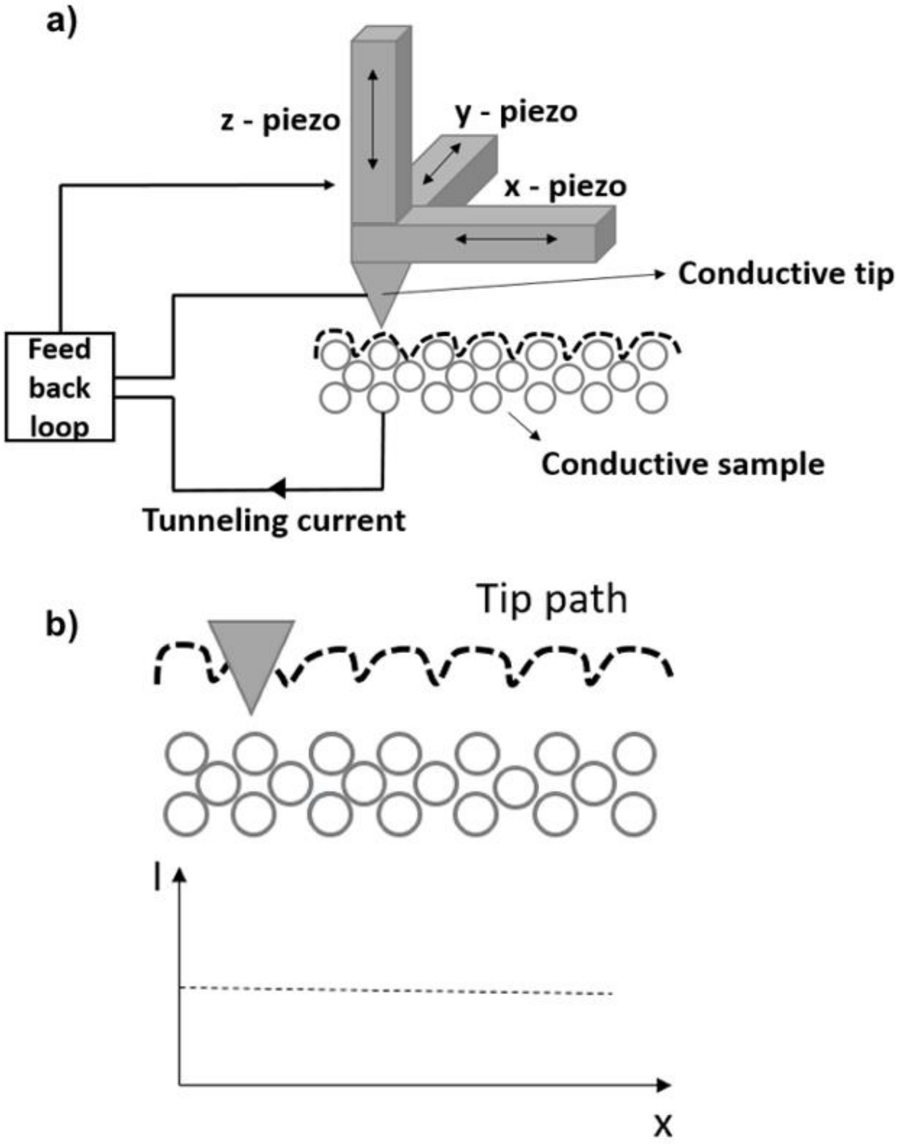

Figure 31. a) This figure shows a schematic of the scanning tunneling microscopy (STM) technique used in this particular thesis. b) The figure illustrates the constant current mode of STM, in which the tunneling current between the tip and the sample is kept constant while the distance between them is varied. This mode allows for the measurement of the sample's topography by monitoring the changes in the tip-sample distance.

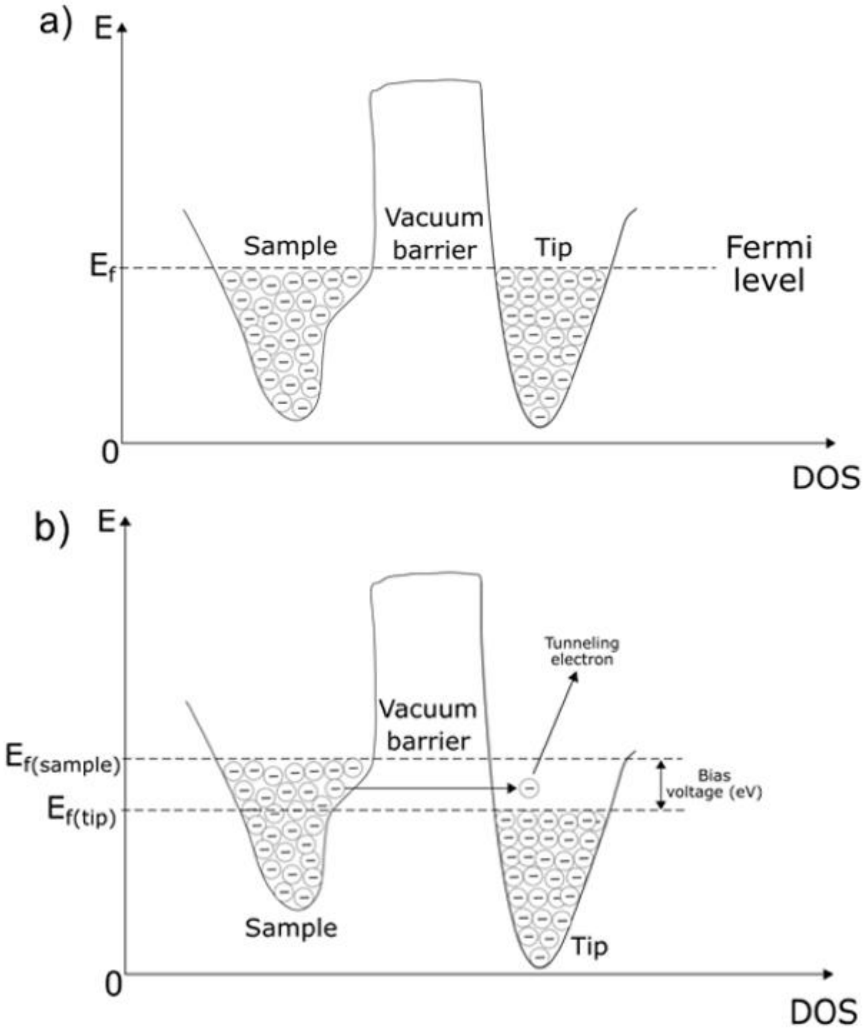

Figure 32. a) A representation of the electron configuration in the scanning tunneling microscopy (STM) setup. The electrons in the tip and the sample are separated by a vacuum barrier, which is necessary to maintain a stable and reliable tunneling current. b) The figure illustrates how the application of a bias voltage to the sample can raise the Fermi level of the sample. This generates empty states in the sample that are available for the tunneling of electrons from the tip into the sample. This phenomenon is the basis of the STM technique, which allows for the imaging and manipulation of surfaces with high spatial resolution.

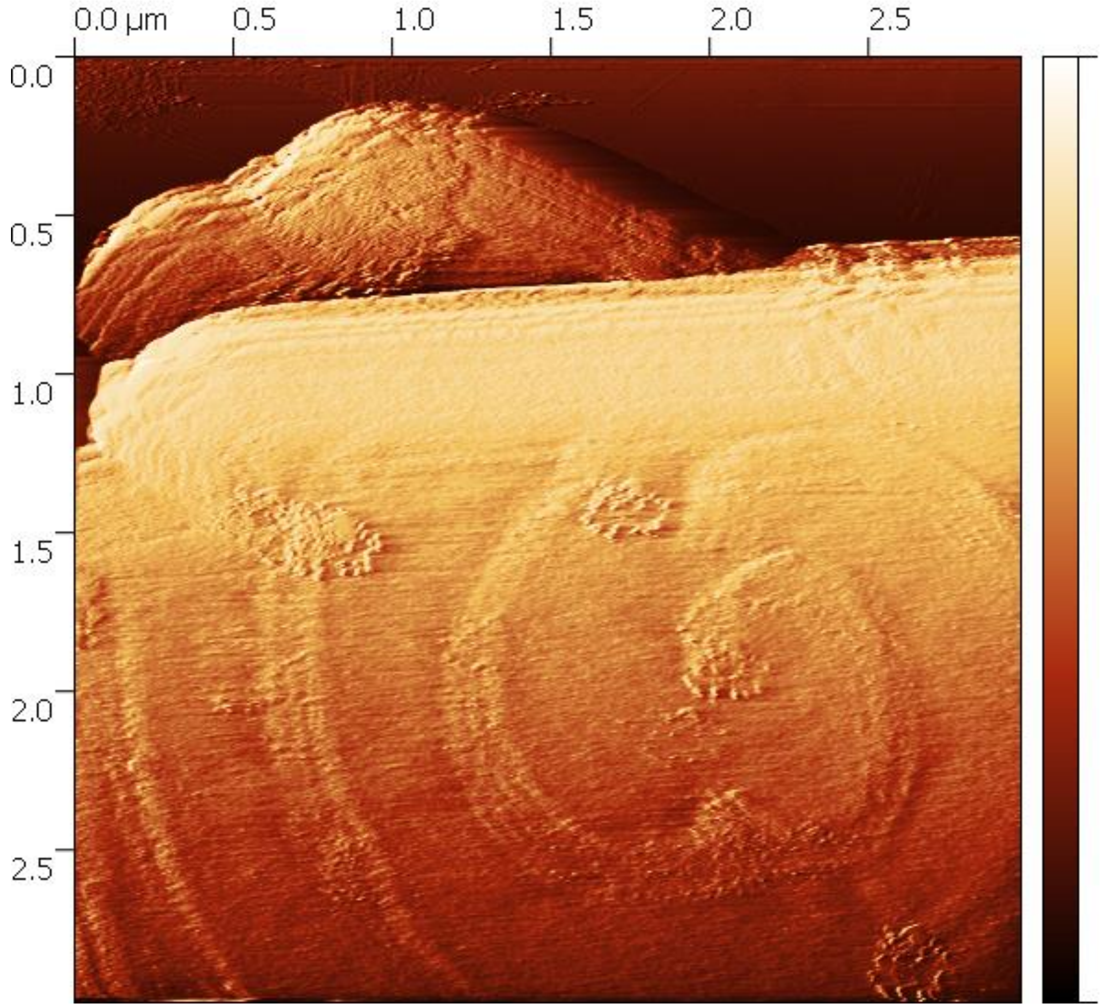

Figure 33. STM image of a spiral SnS platelet.

The STM image, obtained by scanning the sample surface is a combination of the electronic density of states (DOS) and topography of the system. For microscopy imaging, a sharp tip with few atoms is preferred as it facilitates the preferential tunneling to certain orbitals of the tip and improves the spatial resolution of the image. However, for STS, a domed tip is more appropriate to obtain an approximately constant DOS shown in Figure 34. On other hand, the DOS of the sample in general may have specific states for well-defined energies, which appear as peaks, having different complex structures that vary from sample to sample. Thus, the tunneling current will be mainly influenced by the density of states of the sample.

Spectroscopic measurements of the tunneling current at a single point in the sample give information about local conductivity I(V), and differential conductivity dI/dV as a function of V. Therefore, the tunneling spectrum, dI/dV or tunneling spectrum, gives us information about the local density of states of the sample, allowing the study of the electronic properties of different surfaces. Tunneling spectra are presented in Figure 35 as an example of information analyzed in this thesis. The electronic band gap and conductivity can be determined from these spectra. Figure 35a) depicts a portion of the platelet that behaves as an n-type semiconductor, denoted by the Fermi level shift toward the conduction band while Figure 35b) depicts a p-type semiconductor, with the Fermi level, shifted towards the valence band.

Scanning tunneling microscopy (STM) and spectroscopy (STS) were carried out to analyze the sample’s topography and electronic behavior, using an Omicron-GmbH VT-STM, operating in constant-current mode at room temperature (300 K) and ultrahigh vacuum conditions (better than 2.0 × 10− 10 mBar). After the sample was introduced into the load-lock vacuum chamber, it was heated up at 110 ◦C for 10 min for water degassing. STM/STS measurements were performed right after sample cooling to room temperature. dI/dV curves were measured using Stanford Model SR810 DSP Lock-In Amplifier, working at 3.000 KHz. The time constant was 100 ms and the sensitivity was set to 5 × 10− 4 V. The sin wave amplitude was set to 100 mV. Each tunneling spectrum presented in this work is an average value of five repetitions measured at the same position of the sample.

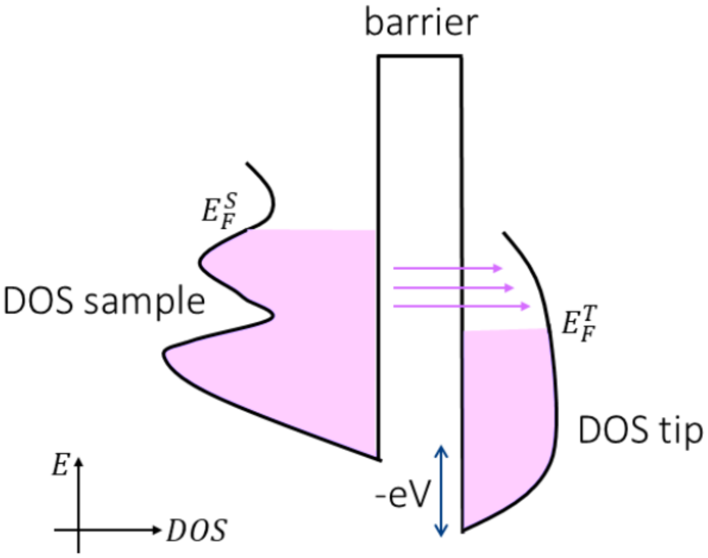

Figure 34. This figure shows a schematic representation of the tunneling process between the sample and the scanning tunneling microscope (STM) tip. The density of states (DOS) of both the tip and the sample are depicted, with the DOS of the tip assumed to be roughly constant. The tunneling phenomenon occurs due to the overlap of the DOS of the tip and the sample, resulting in a measurable current. This illustration was obtained from reference [94].

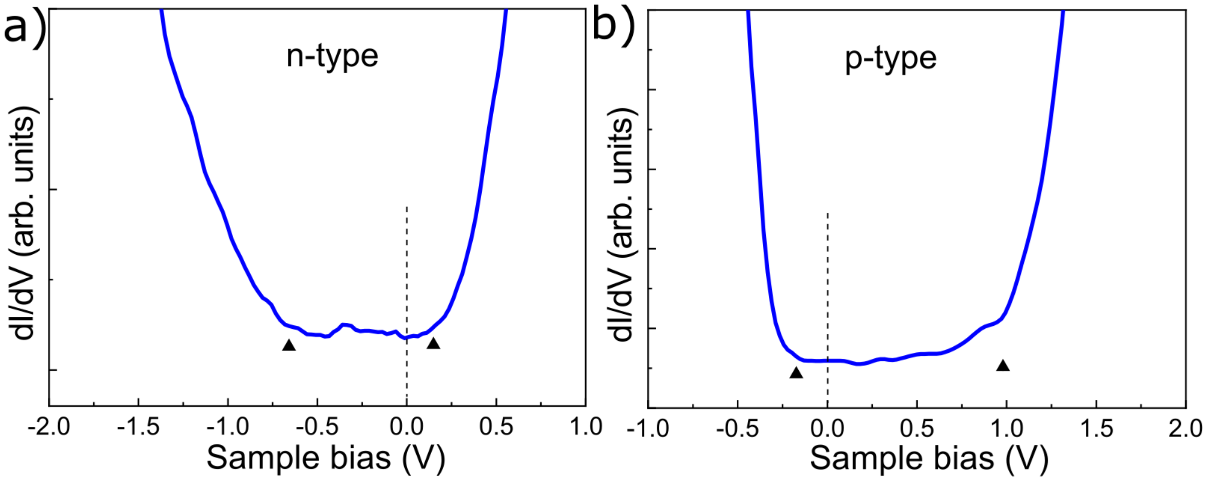

Figure 35. STS of a SnS platelet, with (c) indicating n-type conductivity and (d) indicating p-type conductivity. The band gap is defined by the region between the black triangles.

4.5 Transmission electron microscopy (TEM) and Selected area electron diffraction (SAED)

Transmission electron microscopy (TEM) is a powerful tool for obtaining microstructural and sub-microstructural information, including atomic orientation from the diffraction pattern of crystals. TEM has a resolution of about 0.1 nm. The sample must be transparent to electrons for imaging and obtaining phase-orientation information. The TEM directs an incident electron beam onto the sample, and the resulting signal is captured after the electron beam has interacted with and passed through the sample, as shown in Figure 36. For transmitted electrons, the sample must be thin enough to allow electrons to pass through it. Electrons can be transmitted without any interaction or can be elastically or inelastically scattered.

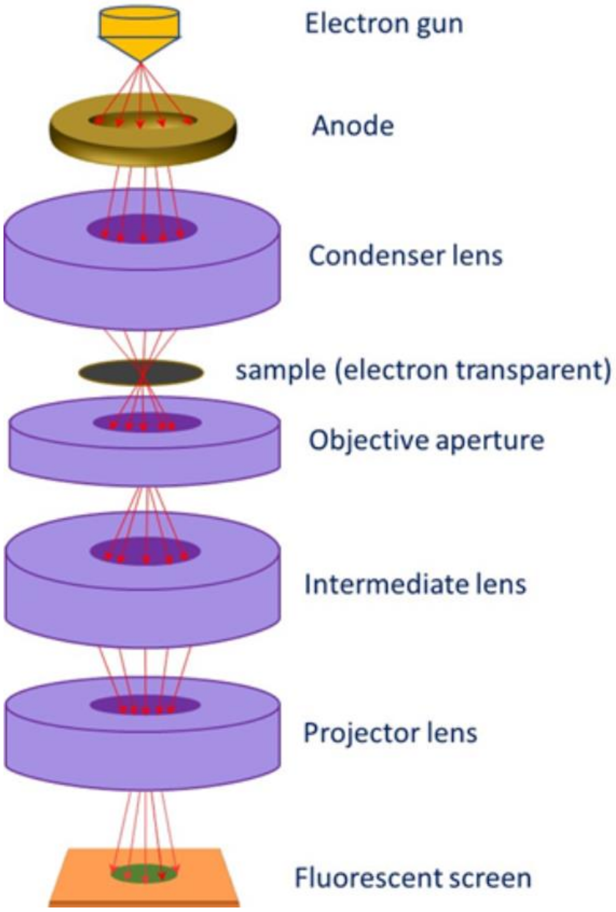

Figure 36. The figure caption illustrates the arrangement of the specimen and electromagnetic lenses in a transmission electron microscope, where the signal is detected after the electron beam has transmitted through the sample. Figure from: https://emb-iitk.vlabs.ac.in/exp/transmission-electron-microscope/theory.html

To perform TEM, an electron gun that generates electrons and a set of electromagnetic coils that control the beam's size and shape, as shown in Figure 36. Thermionic (W-filament) and field-emission (using LaB6, CeB6 filaments) are used to generate electrons. The anode repels the electrons to constrict the diverging beam, while the set of electromagnetic lenses (condenser lens) focuses the beam on the sample. To stabilize and prevent damage to the sample upon electron beam irradiation, it is kept in a cold chamber (in liquid nitrogen condition). A liquid nitrogen dewar provides condensation of ionized atoms in the vicinity to avoid interference with the sample imaging and characterization. The electron beam passes through the electron-transparent sample and falls on the objective lens. The objective lens is the most important lens as it generates the first image of the sample, which is then magnified using the projective lens.

The setup requires stable high voltage (ranging from 120 kV to 2 MV, with 200 kV typically used) and a high level of vacuum (10^{-6} to 10^{-8} torr). An electron gun generates and accelerates electrons to high energy. The resolution of TEM images (both bright field or dark field) and diffraction patterns depends on the electron wavelength, which is determined by the accelerating voltage. Increasing the accelerating voltage decreases the electron wavelength, which leads to higher resolution. Typical accelerating voltages are around 200 kV, while high-resolution TEMs may use up to 2 MeV energy (or 2 MV voltage).

A set of electromagnetic lenses form a condenser system, which can be adjusted to provide a parallel or convergent beam for imaging or diffraction. The objective lens is the most critical component of the TEM system as it forms the first intermediate image, which determines the resolution of the final image. The diffraction and intermediate lenses can be switched to obtain either a diffraction pattern or an image. The projection lens then forms the second intermediate image, which can be either a diffraction pattern or an image. To ensure a clean column tube (typically a few millimetres in diameter) through which the electron beam passes, the sample is kept under cryogenic conditions (usually under liquid nitrogen). This prevents the ionised material from scattering and forming poor signals. A liquid nitrogen dewar is often used to maintain low temperature near the TEM specimen. The final image or diffraction pattern can be observed on a viewing screen or camera.

The principles of TEM imaging can be understood through the ray diagram shown in Figure 37. In TEM, the aperture is placed at the back-focal plane of the objective lens to produce images. On the other hand, placing the aperture at the image plane of the objective lens results in diffraction patterns.

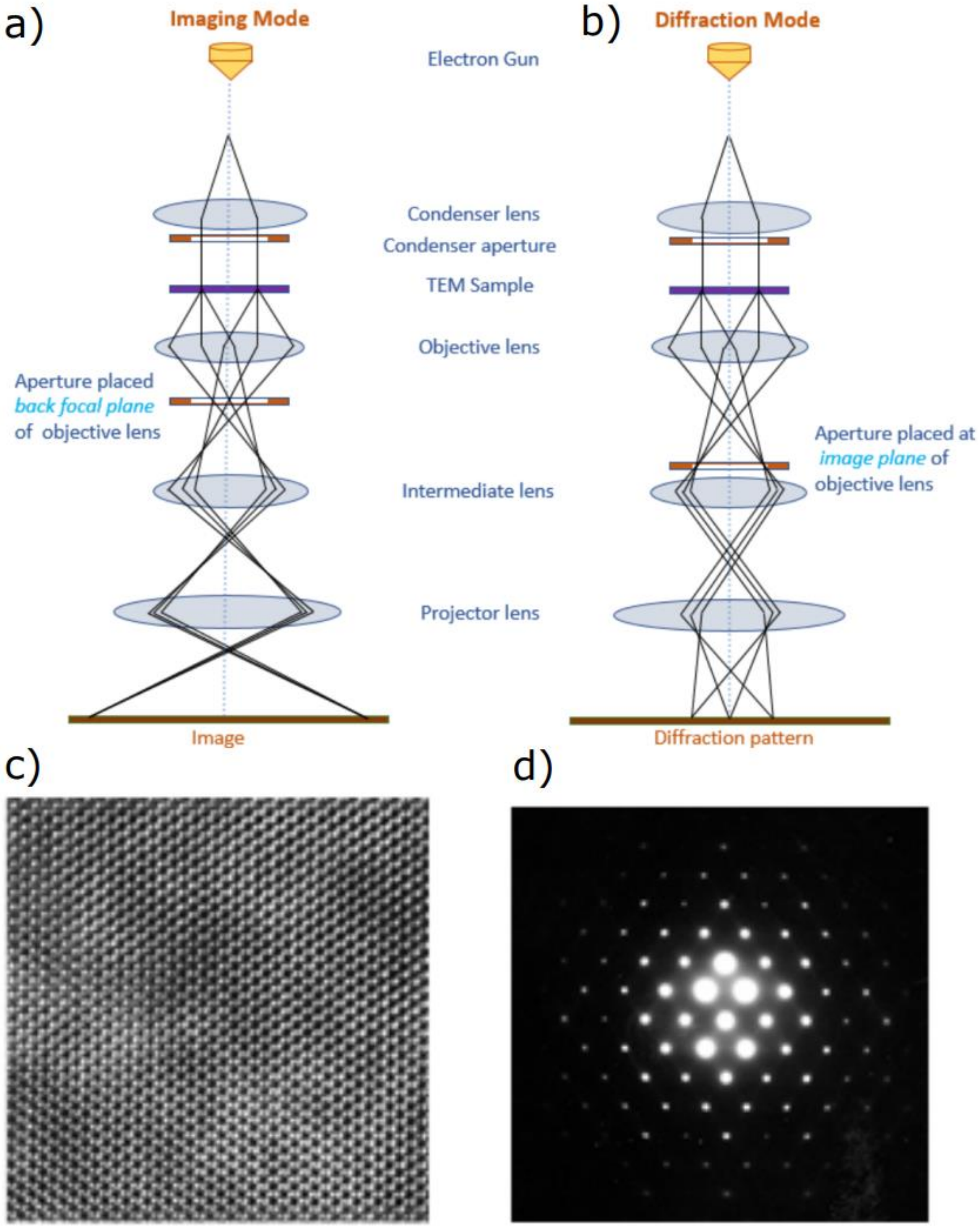

Figure 37. Ray-diagram that demonstrates the positioning of an aperture for obtaining either an image or a diffraction pattern. The figure a) shows the placement of the aperture to obtain an image, while the figure b) shows its placement to obtain a diffraction pattern (Figures from: https://emb-iitk.vlabs.ac.in/exp/transmission-electron-microscope/theory.html). Figure c) shows a high resolution TEM image of Si(110) and d) a selected area electron diffraction pattern (Figure from: https://www.toray-research.co.jp/en/technicaldata/techniques/TEM.html).

A bright field image is obtained when the aperture is placed at the back-focal plane of the objective lens (Figure 37a), while a diffraction pattern is produced when the aperture is located at the image plane of the objective lens. The diffraction can be captured from a specific area, known as selected area diffraction (Figure 37b), which shows a pattern consisting of individual spots from a single-crystal region, rings from a nanocrystalline region, or scattered overlapping spots from several different crystals. The bright field image displays bright features and appears dark, and the length units obtained are typically in nanometers (nm) (Figure 37c). In contrast, the diffraction image is obtained in reciprocal space, where the units observed are typically 1/nm. The diffraction pattern depends on how the electron beam interacts with the matter and how many crystals interact to provide the resulting image. The symmetry of the actual crystal determines the final pattern obtained in the diffraction image.

4.6 J-V characteristics system

The diagram in Figure 38 displays the internal workings of a solar simulator illumination source and optical pathway. An elliptical reflector is utilized to direct light generated by the source toward the second focal point and the first mirror. This mirror is either full spectrum or dichroic and reflects the light downwards to create an efficient and compact optical pathway. To achieve the desired output spectrum, the mirror guides the light through a set of spectrum-shaping filters. The homogenizing lenslets ensure that the illumination is evenly distributed, and adjustable spacing lenslet arrays permit minor adjustments to the size of the illuminated field. The shutter, located after the spectral and illumination enhancers, prevents light from reaching the work area without turning off the illumination source. The second 90° reflector folds the optical path back to a vertical orientation, and the light travels through a condenser lens for final collimation. This produces a uniformly distributed irradiance at the work plane within the specified range of working distance.

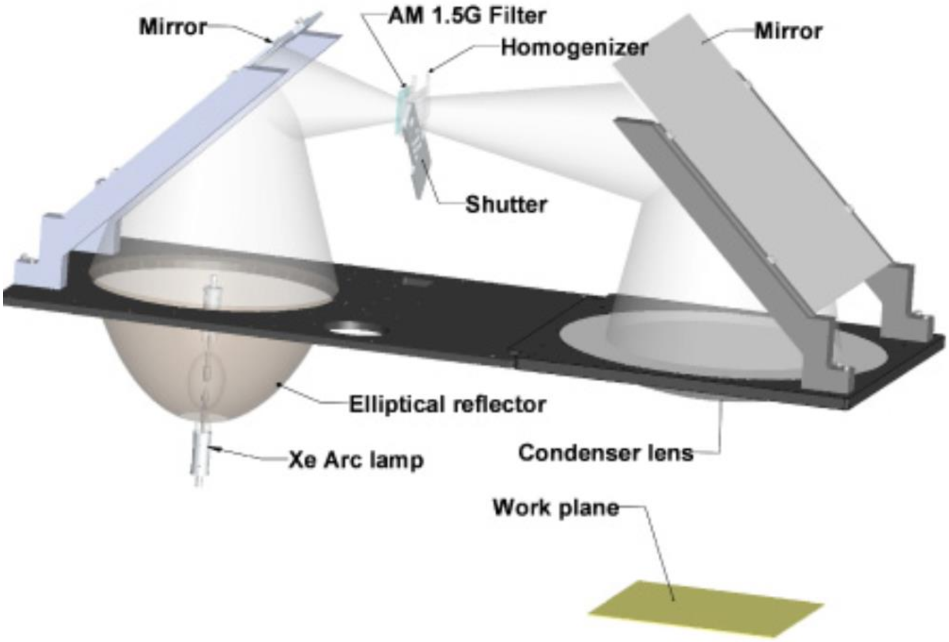

Figure 38. This figure presents a schematic view of the optical train for a solar simulator, which comprises a number of components, including a xenon arc lamp, elliptical reflector, principal mirrors, AM 1.5G filter, homogenizer, shutter, condenser lens, and work plane. The xenon arc lamp serves as the light source, and the elliptical reflector is used to collect and redirect the light emitted from the lamp towards the mirrors. The AM 1.5G filter is employed to simulate the solar spectrum. The homogenizer is then used to achieve uniform light intensity, and the shutter is used to control the light output. Finally, the condenser lens is used to focus the light onto the work plane. This figure, obtained from reference [95], provides a comprehensive overview of the optical system utilized in the solar simulator.

The light generated by the simulator is aimed at the solar cell, connected to a probe station, at the workplace. The Keitlhey 2400 sourcemeter, which acts as a bipolar power supply, is also connected to the probe. The device can change the bias voltage direction from forward to reverse and vice versa. The process is carried out at different light intensities, including the AM1.5G configuration, both in the absence of light and under illumination. The measurement involves applying a range of voltages to the device and measuring the current flowing through it at each voltage. This is done using the sourcemeter, a highly accurate device capable of simultaneously supplying voltage and measuring current. This process yields a J-V curve measurement. Figure 39 shows a schematic of the J-V measurement setup used in this thesis that represents a Keithley 2400 power supply and solar simulator (Abet Gen II).

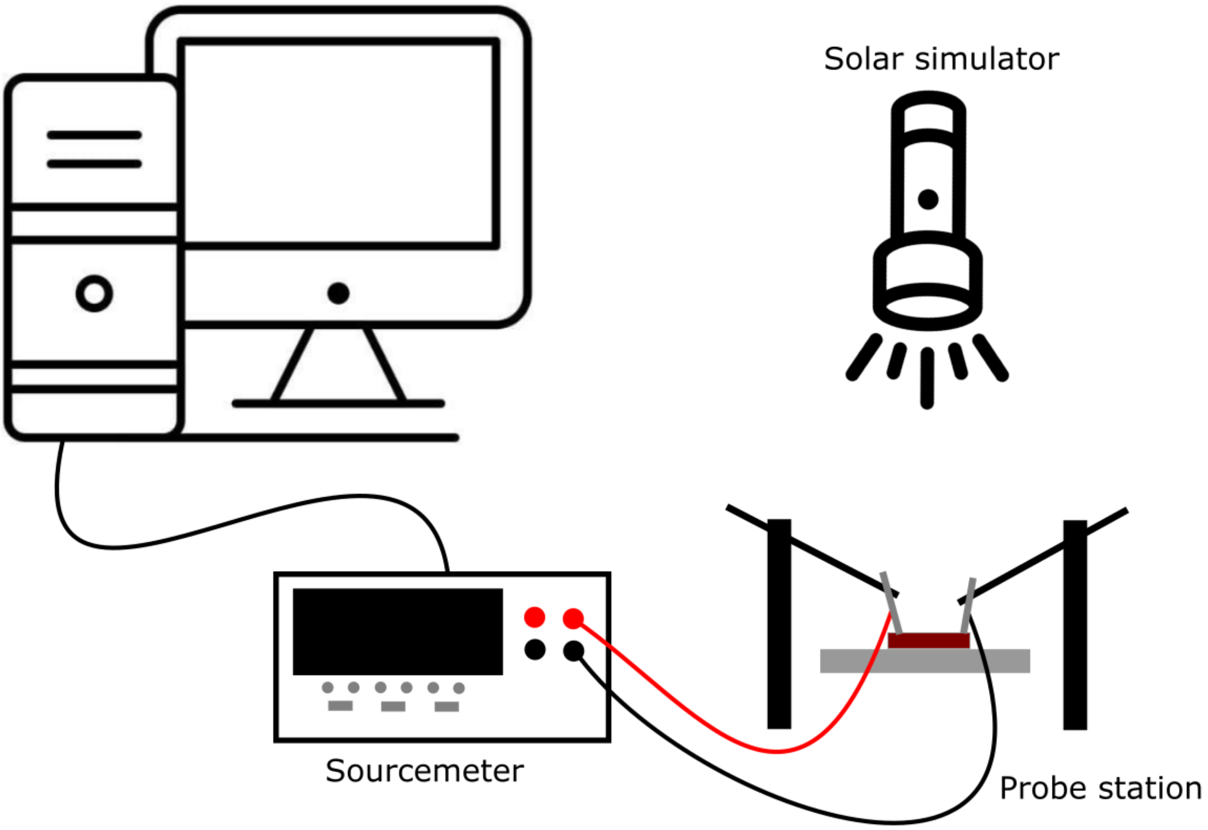

Figure 39. The figure represents a schematic of the J-V curve experiment, which involves measuring the current-voltage (J-V) characteristics of a solar cell. The solar cell is illuminated by a xenon arc lamp, which provides different light intensities. The solar cell is connected to a probe station, which enables precise positioning of the cell and measurement of the electrical parameters. The probe station is connected to a sourcemeter that supplies a known voltage to the cell and measures the resulting current. The sourcemeter is then connected to a computer, which records the current-voltage data and constructs the J-V curve. This figure provides a simplified overview of the experimental setup used to measure the J-V curve of a solar cell

Once the functioning of the equipment has been understood, it becomes possible to comprehend the physical model of a thin film cell and its relationship to the measurement carried out in this work. Fundamentally, the thin film solar cell operates as a diode, requiring a p-n junction. Its current density-voltage (J-V) characteristics follow the ideal diode equation:

$$J = J_0 \left[\exp\left(\frac{qV}{k_B T}\right) - 1 \right] - J_L \,, \tag{3}$$

where q is the elementary charge, k_B is the Boltzmann constant, T is the absolute temperature, J_L is the photocurrent generated and J_0 is the reverse-saturation current density.

However, solar cells can experience losses that are not considered in the ideal diode equation, due to the presence of series and shunt resistances. The shunt resistance (R_{sh}) is responsible for the charge carrier recombination near the dissociation site, while the series resistance (R_s) takes into account the average charge carrier mobility. Figure 40 depicts the equivalent circuit of a single junction thin film solar cell.

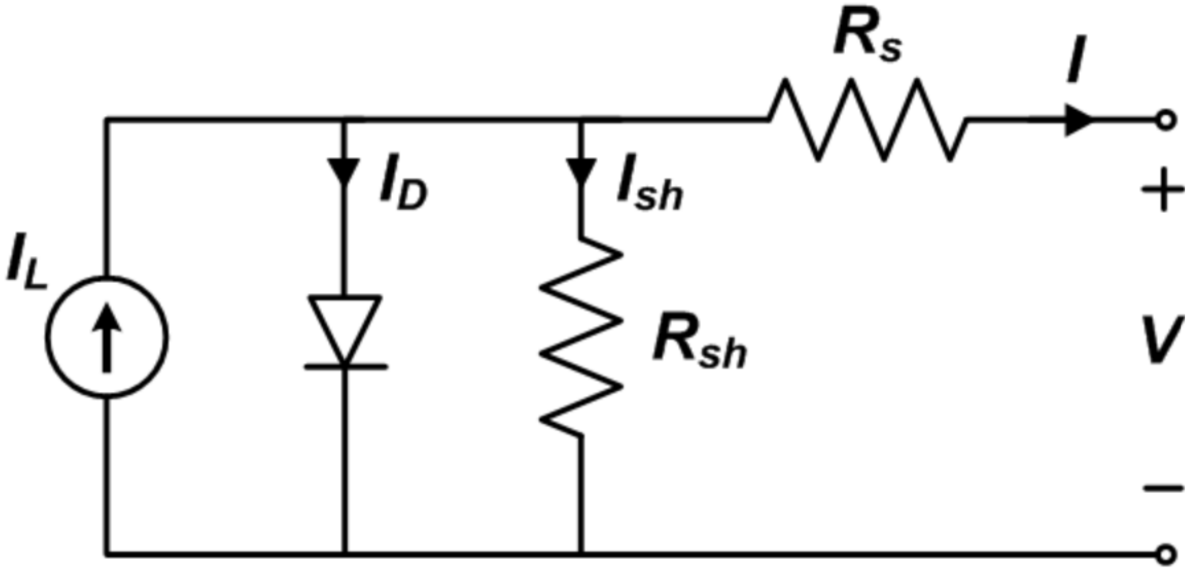

Figure 40. The equivalent circuit of a thin-film solar cell. I_L is the photocurrent generated in the cell and I_D is the voltage-dependent current lost to recombination. Reproduced from ref. [96].

Considering the circuit above and the ideal diode equation, the solar cell adapted equation for J-V characteristics can be written as:

$$J = J_0 \left[exp \left[\frac{q(V - JAR_S)}{nk_BT} \right] - 1 \right] + \frac{V - JAR_S}{R_{sh}A} - J_{ph} \;, \qquad (4)$$

where A is the active area of the device and n is the ideality factor. Note that if R_s = 0 and R_{sh} = ∞, Eq. 4 -> Eq. 3 for the ideal case.

The J-V response curve of a solar cell is obtained by plotting the current density as a function of the voltage. This curve yields three useful parameters: short-circuit current density (J_{SC}), open-circuit voltage (V_{OC}), and fill factor (*FF*). J_{SC} occurs at zero applied bias, V_{OC} occurs when the current density is zero, and the fill factor is a measure of a device's deviation from the ideal maximum power, where $P_{ideal} = J_{SC} \times V_{OC}$. Figure 41 illustrates these three metrics, together with J_{MMP} and V_{MMP}, which represent the current density and voltage at the device's maximum power (MMP = max power point).

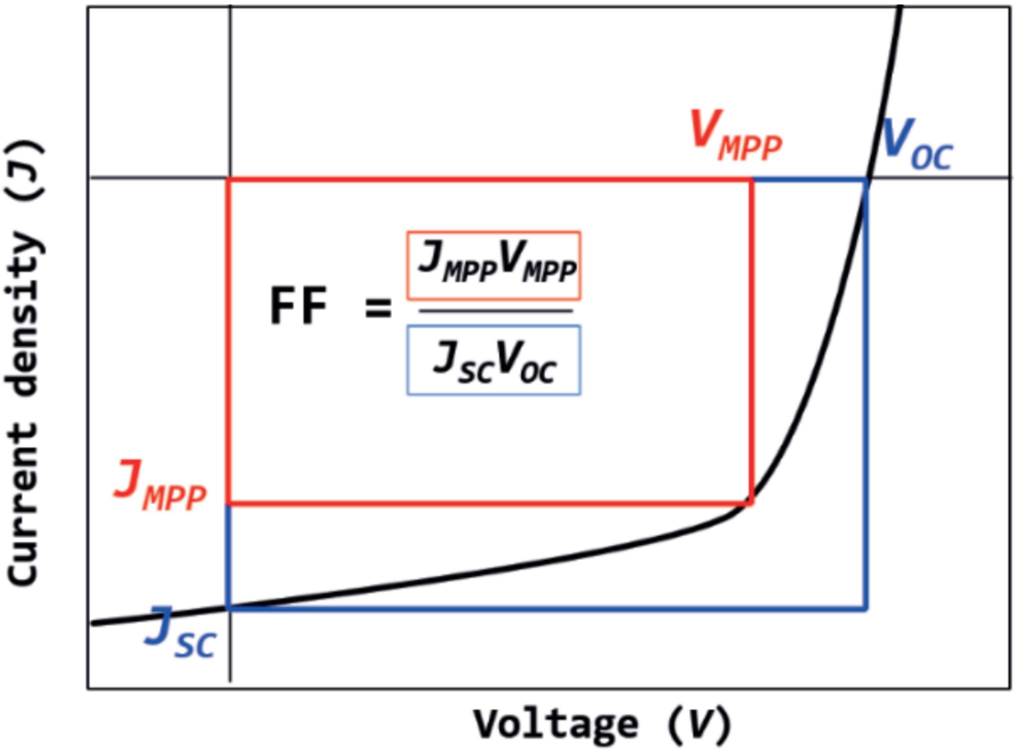

Figure 41. J-V curves illustrating the performance metrics: J_{SC}, V_{OC} and calculated fill factor. Figure from ref. [97].

Finally, the overall conversion efficiency of a solar cell can be calculated using the following equation:

$$\eta = \frac{P_{ideal}\,FF}{P_{in}} = \frac{J_{SC}\,V_{OC}\,FF}{P_{in}}\,, \tag{5}$$

where $P_{in} = 100\ mW/cm^2$ corresponding to Sun power in AM1.5G configuration and $FF = P_{MMP}/P_{ideal}$.

4.7 External Quantum efficiency (EQE) system

This section describes the operation of a quantum efficiency system, which involves several steps. The system utilizes a xenon lamp to produce broadband white light, a monochromator with a frequency chopper, and a lock-in amplifier. The monochromator is illuminated with continuous wavelength white light, and then generates monochromatic light of a specific wavelength using different optical techniques such as prism, bandpass filter or grating. The generated monochromatic light is modulated into a specific frequency AC light source by an optical chopper, and the radiation energy of the incident monochromatic light is calibrated using a photodetector. The same amount of incident photons is then illuminated on the solar cell under test, and the generated photocurrent signal is demodulated and read out by the lock-in amplifier. By dividing the incident photon energy and generated photon current, the spectral response value is obtained. The SR spectrum of the device under test is obtained by continuously changing the different wavelengths, and then the EQE spectrum is obtained by unit conversion. Figure 42 shows the system setup. In this theisis the EQE measurements were performed using a PV Measurements QEX10 system. Spectral response was measured between 300 and 1200 nm in dc mode with a step size of 10 nm and calibrated using a standard silicon reference solar cell.

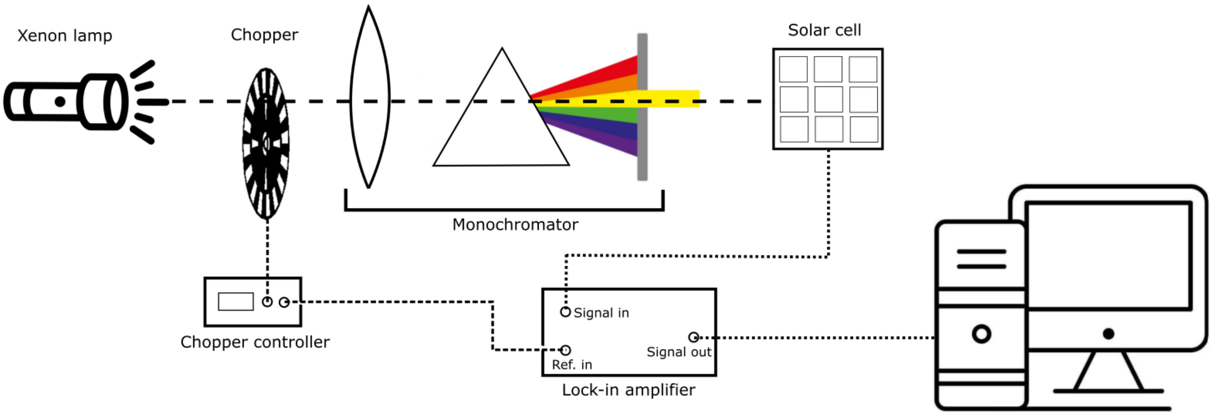

Figure 42. A diagrammatic representation of the optical arrangement utilized in the EQE system. The system utilizes a xenon lamp to produce broadband white light, which is chopped at a frequency that can be detected by a lock-in amplifier. The modulated light is then directed through a monochromator to select a specific wavelength and reaches the solar cell device. The resulting signal generated by the solar cell is passed through the lock-in amplifier, which is modulated by the chopper controller to improve the signal-to-noise ratio. Finally, the processed digital signal is applied to the computer's processor for analysis.

Prior to conducting any measurements, it is necessary to calibrate the EQE system using a reference device. This calibrated reference device is essential for accurately measuring the EQE of the solar cell being tested. The calibration of the EQE system is crucial, as it involves comparing the quantum efficiency of the solar cell under test to the response of a calibrated silicon or germanium photodiode.

As mentioned, the EQE measures the fraction of photons that are converted into electrons by the solar cell. It is expressed as a ratio of the number of electrons generated to the number of incident photons on the solar cell per second:

$$EQE = \frac{electrons/second}{photon/second}\,. \tag{6}$$

EQE measurements are conducted at J_{SC}, where the voltage across the cell is zero. It indicates the amount of photocurrent produced by the cell when it is illuminated by monochromatic light at different wavelengths. The ideal EQE graph maintains a constant value across all measured wavelengths. However, the EQE for most solar cells suffers from external and internal losses, where charge carriers are not able to reach an external circuit. External losses refer to reflection and absorption in the optical stack of layers that come before the absorber. Differently, internal losses are due to incomplete absorption and electrical recombination effects that occur within the absorber layer. Figure 43 depicts the EQE for an ideal and crystalline silicon standard cell.

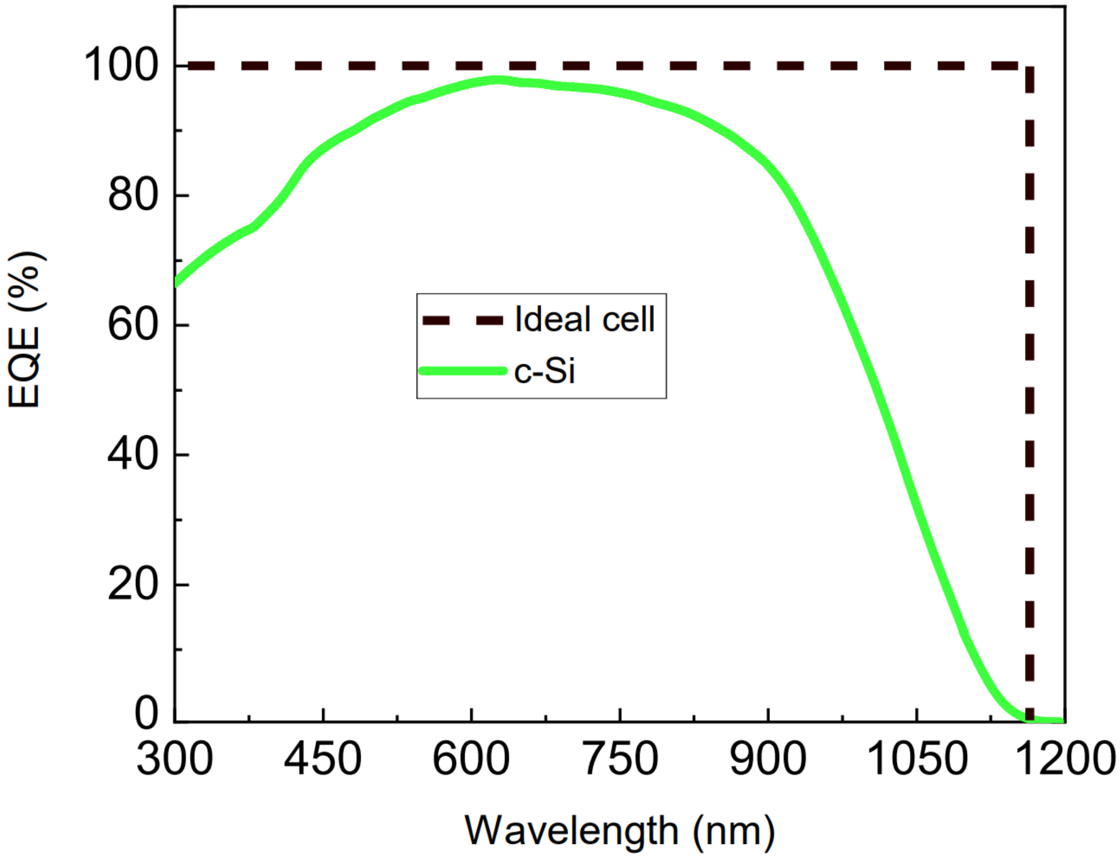

Figure 43. Quantum efficiency spectra of crystalline silicon standard solar cell (green) and ideal ideal cell (dashed line).

5. Electronic gap stability of two-dimensional tin monosulfide phases: Towards optimal structures for electronic device applications

5.1 Introduction

In this work, we present a STM-STS and electron diffraction study of SnS platelets grown on highly oriented pyrolytic graphite (HOPG) using vapor phase deposition, which has already been established as a reliable growth technique for this compound[87,98–101]. These characterization techniques revealed the presence of two types of platelet-shaped SnS crystals. The first one consists of nearly square-shaped platelets with atomically flat surfaces (hereafter called flat platelets). The second type exhibits spiral morphology at the platelet surface, with height steps of a few atomic layers in their centers (hereafter referred to as spiral platelets). Flat platelets are previously known to correspond to the orthorhombic in the α-SnS phase[88] and we demonstrate here that spiral platelets are in the π–SnS phase, which is cubic. This phase has been recently studied by several techniques, but a deeper understanding using a technique that is sensitive to both electronic and atomic structure (such as STM/STS) has not been performed so far [102–105]. The morphologic and electronic properties of SnS and its effects on physical properties are discussed in detail using an ensemble of complementary characterization methods.

5.2 Experimental methods

SnS isolated and spiral platelets grown on HOPG substrates and studied in this work were synthesized using vapor phase deposition. These substrates were chosen since they provide an atomically flat surface termination with suitable conductivity and known spectroscopic response for STM/STS measurements. Additionally, HOPG provides a flat, weakly reactive surface condition, assuring that the SnS system phase and morphology depend mostly on the growth temperature [50,88,99,101]. The growth process was performed in a 110 cm long tube reactor with a diameter of 3 cm in a two-zone tubular furnace. The SnS powder source was acquired from MKnano with 99.5% purity and presented an undesired Sn_2S_3 phase. In order to eliminate this phase the powder was thermally treated at 500°C for 1 hour. The X-ray diffraction scans of the powder before and after the treatment indicated that the other spurious phase was eliminated and the treated material contains only the SnS phase according to ICSD number 52108, as shown in Figure 44.

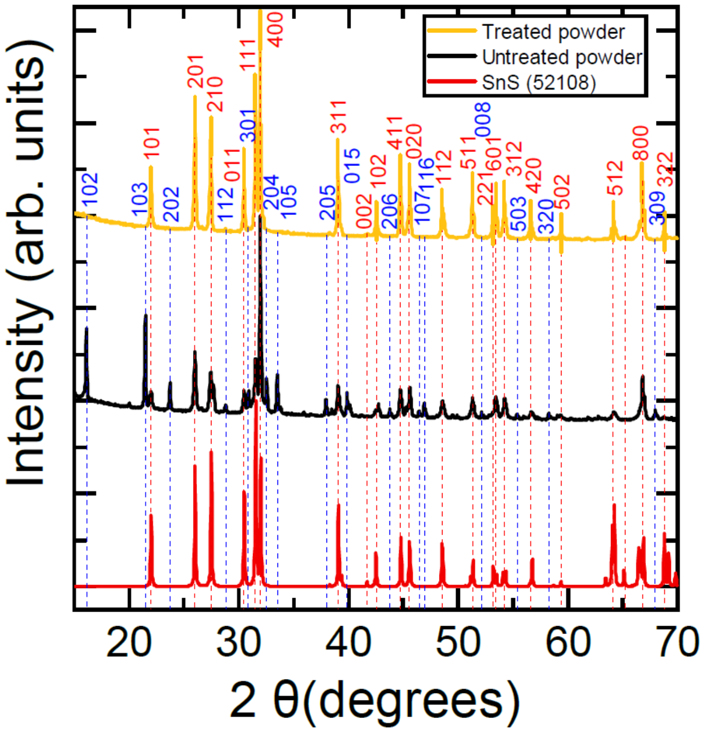

Figure 44. XRD data of SnS heat treated powder (yellow), untreated powder (black) and XRD data for SnS taken from ICSD number 52108. The vertical red dashed lines indicate the peaks for SnS and the blue dashed lines present peaks for Sn_2S_3.

In order to synthesize SnS platelets and films 600 mg of the purified SnS powder was placed at the center of the furnace hot zone (zone 1 – see Figure 45a) in an alumina boat. The HOPG substrate, with dimensions of 1.2 × 1.2 cm^2, was placed at a distance of 8 cm downstream from the SnS source. The tube reactor was connected to a vacuum pump and ultrapure argon was injected with a flow rate of 200 sccm for 20 min, to purge the chamber. Afterward, the argon flux was decreased to 110 sccm and the pressure was stabilized to approximately 72 Pa. Subsequently the furnace was heated with a 30-minute ramp to reach 550°C at zone 1 and 250°C at zone 2. In this configuration, the temperature varied from approximately 550°C to 520°C along the HOPG substrate in the longitudinal axis direction(see Figure 45a). The system was heated for 10 min while SnS vapor was carried downstream and deposited on the substrate. Finally, the system was then naturally cooled to room temperature. The schematic of the synthesis is shown in Figure 45.

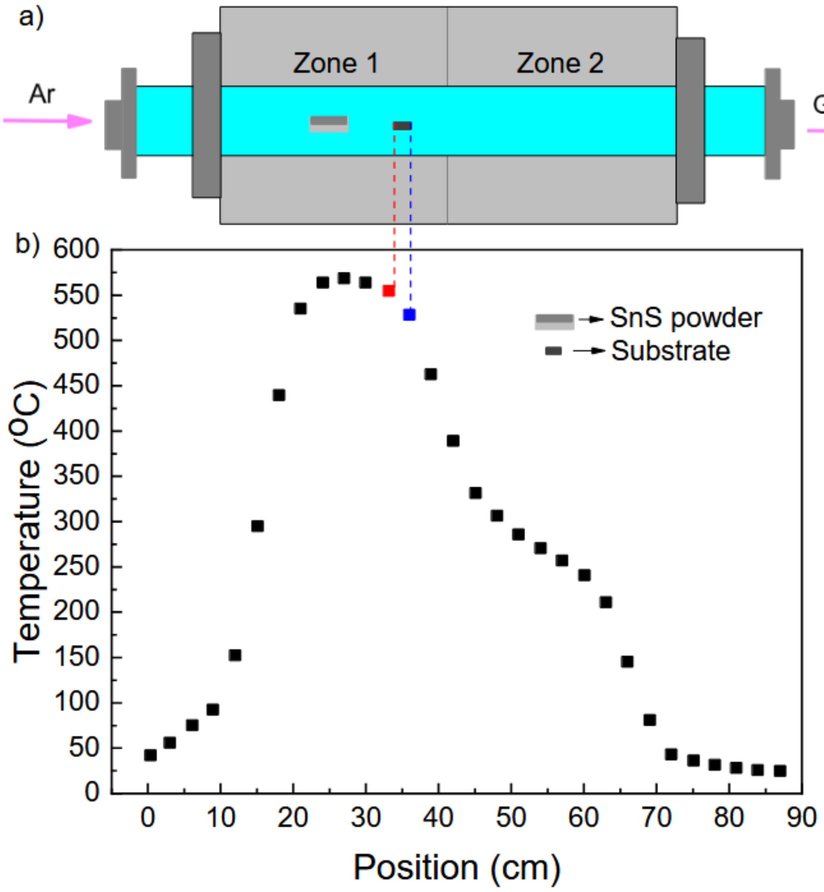

Figure 45. a) Schematic representation of the experimental setup for growth of SnS samples. The vertical red and blue dashed lines indicate the regions where flat and spiral platelets appear, respectively. b) Measured temperature profile of the furnace along its horizontal axis for conditions used in this work.

5.3 Results and discussion

Two major SnS morphologies observed in our samples, grown under temperature gradient conditions (see growth details in the experimental section), are shown in Figure 46a-d. In the region of the substrate closer to the SnS source, where the temperature was 550ºC, flat SnS platelets, with lateral dimensions of 1.5–3 µm and an approximately square shape, were formed (see Figure 46a). These platelets can be seen in better detail in the inset of Figure 46a. The density of platelets increases in the regions further away from the source (with a smaller nominal temperature of 520ºC). Spiral platelets with less homogeneous morphologies were observed (see Figure 46c). In the inset in this panel one of the spiral platelets is magnified for better visualization. Figure 46b and 42d present EDS analysis for SnS-isolated flat and spiral platelets, respectively. Sn:S atomic ratios close to 1:1 were retrieved in both cases, indicating that the synthesized materials have SnS stoichiometry, albeit the observed morphological differences. This indicates the absence of other sulfur-rich tin sulfide phases. The platelet thickness was later obtained for each phase using STM. We anticipate here that an average thickness of ~100 nm is found for flat platelets, which exhibit atomically flat exposed surfaces, while spiral platelets exhibit similar thicknesses but with surface steps ranging from 3 nm to 8 nm.

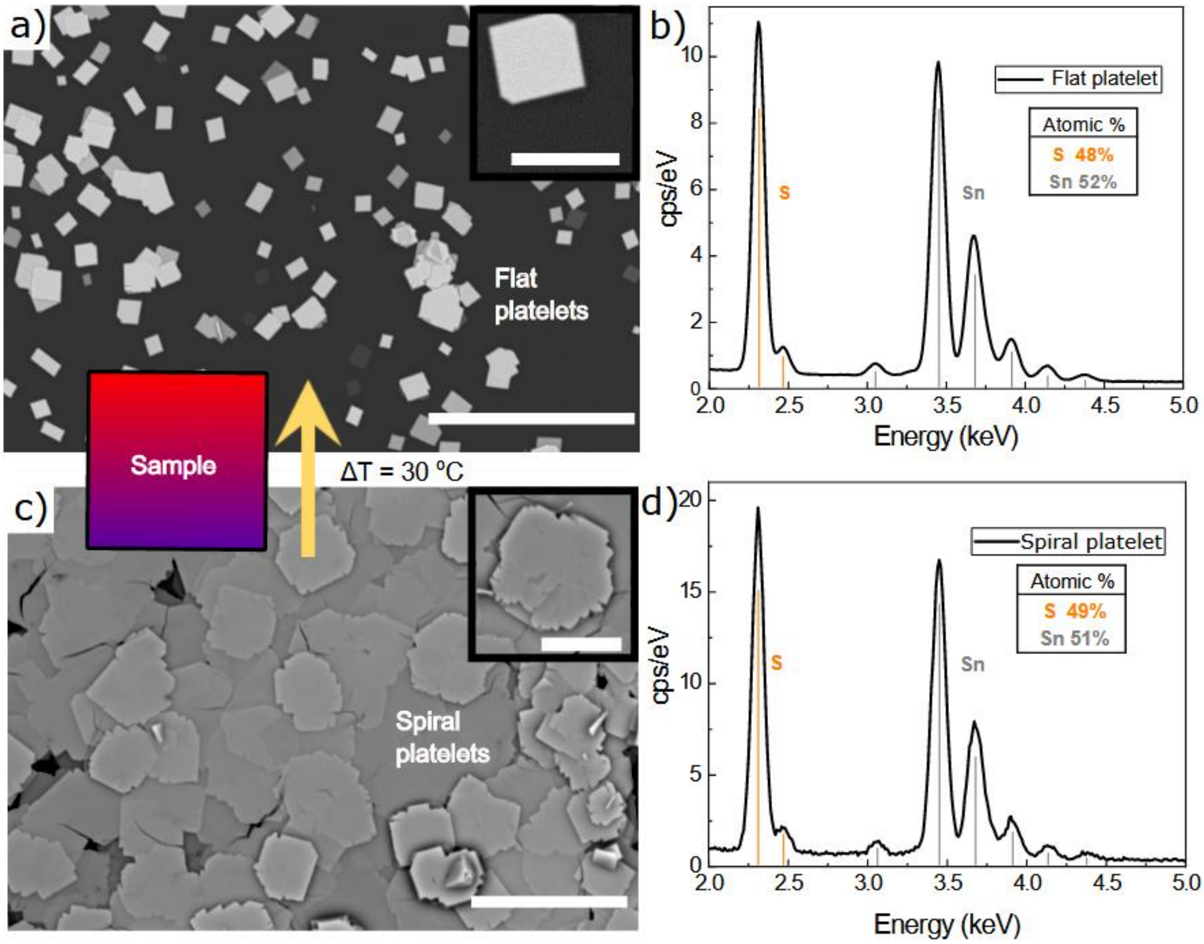

Figure 46. SEM images of HOPG with sample schematic representation of temperature gradient (colored square connecting images (a) and (c)) indicating temperature variation of ΔT = 30 ◦C between different regions of the substrate. a) HOPG region close to the source (higher growth temperature) with isolated SnS flat platelets. b) EDS spectrum of isolated flat SnS platelets. c) HOPG region futher away from the source, exhibiting spiral platelets with irregular shapes. d) EDS spectrum of spiral SnS platelets. In SEM figures scale bars are: a): 20 µm (inset: 5 µm) and c): 10 µm (inset: 5 µm).

Such variation in platelet morphology along the substrate surface can be attributed to the gas phase supersaturation [107]. In the region close to the SnS source, the supersaturation decreases the surface mobility of atoms. The SnS material produced in this region is forced to follow the registry of initial layers, resulting in defects whenever the stacking registry is lost (local compensation of stacking faults). Away from the SnS source, the saturation decreases, increasing the surface mobility of adatoms, which fills up possible vacancies and point defects. The imperfect registry is then compensated globally (and not locally) by the appearance of spiral-shaped steps.

In order to identify the compound formed in each region of the sample we have carried out micro-Raman measurements. Figure 47a shows a spectrum acquired at a single flat platelet, exhibiting characteristic peaks of the orthorhombic SnS phase [88]. On the other hand, the Raman spectrum measured on a spiral platelet shows broad peaks, decomposed in Gaussian contributions in Figure 47b. The resulting spectrum in this case is compatible with previous results on cubic SnS phase [105,108], indicating that a structural change may lead to distinct platelet morphologies.

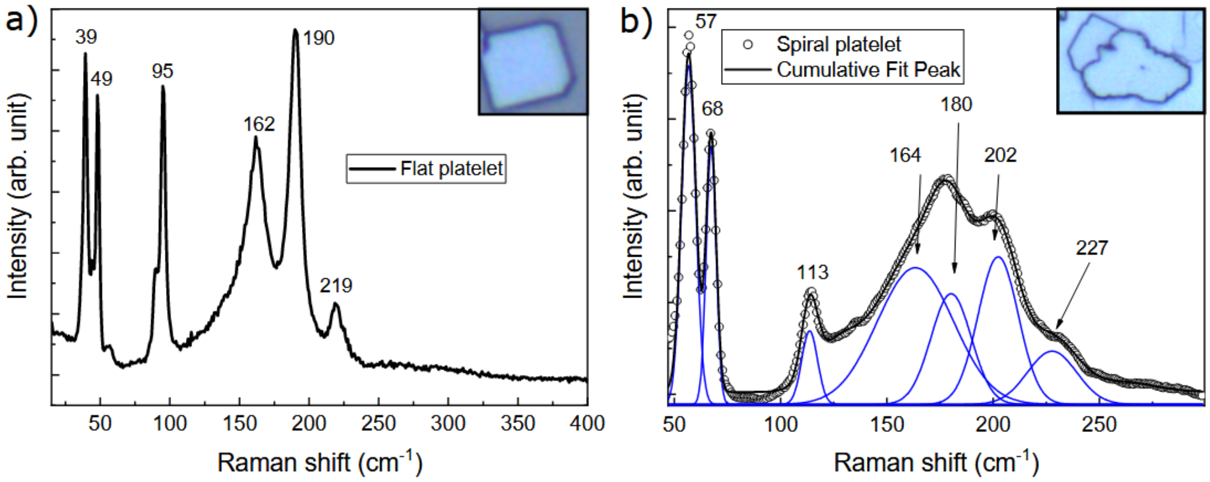

Figure 47. Raman spectra of the two types of platelets grown on HOPG. a) Raman spectrum of flat platelet where sharp peaks are observed at positions that indicate the formation of α-SnS phase. b) Raman spectrum of a spiral platelet (open dots), with background subtraction and cumulative fit peak (black line), showing frequency peaks (blue lines) that corresponds to π -SnS phase.

Furthermore, according to the data presented in Figure 48, Raman spectra were obtained from various regions of the HOPG substrate. Where (a) is the farthest to de SnS source and (d) is the closest region. The number density of platelets increases in the regions further away from the SnS vapor source. The findings indicate that changes in temperature lead to a phase transition from π-SnS (a) to α-SnS (d).

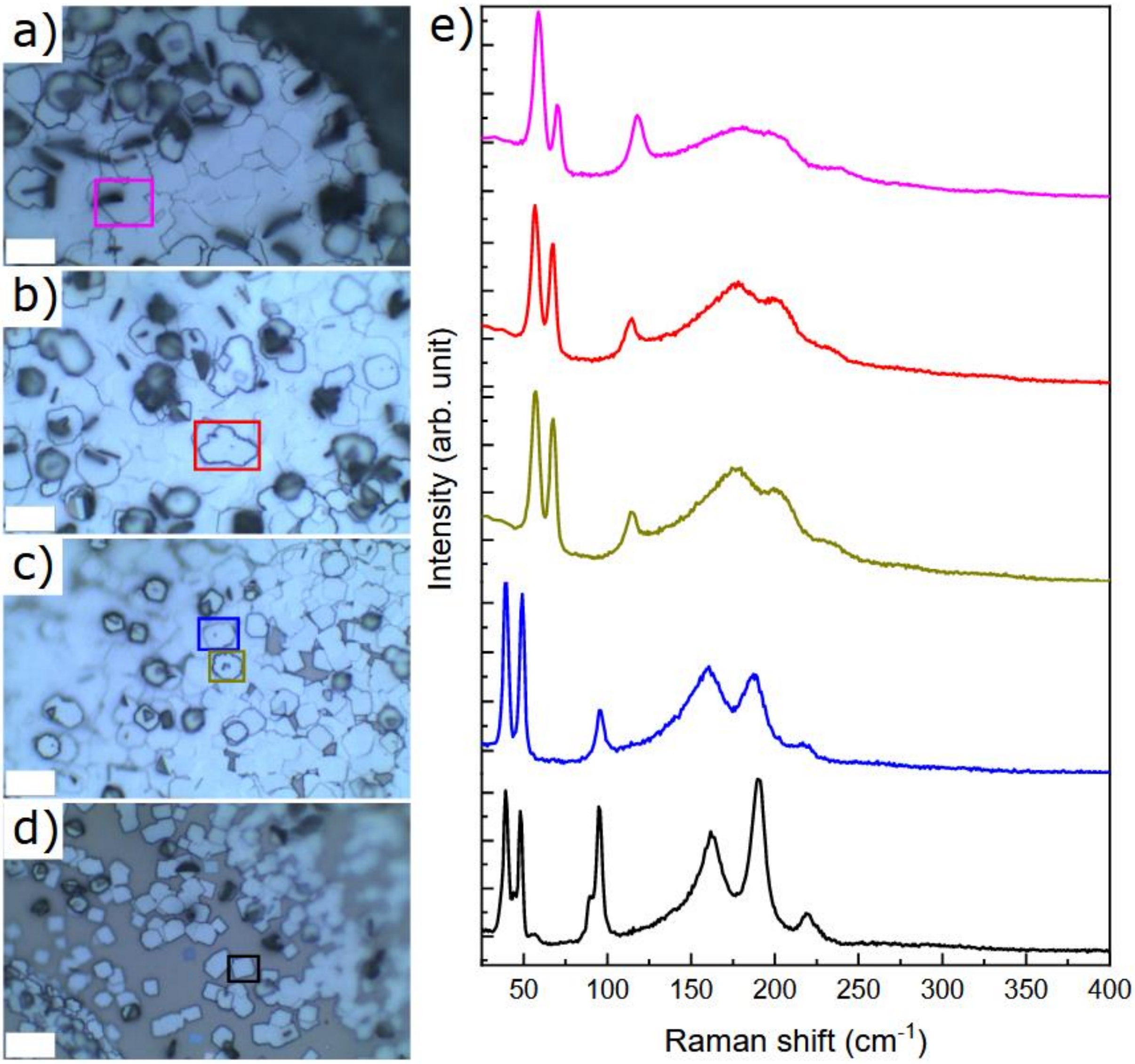

Figure 48. Optical microscopy of different parts of the HOPG substrate, where (a) is the farthest to de SnS source and (d) is the closest region. e) Raman spectra measured at the marked squares represented in optical images.

Figure 49a shows an STM topographic image of an isolated SnS flat platelet, with an orthorhombic shape and lateral size of 2.3 µm (grown in the region shown in Figure 46a). This platelet presents the typical SnS shape which is commonly observed in previous works [88,109,110], with corner angles of ~85° and ~95° due to the preferential growth facets as discussed by Tritsaris *et. al.* using surface energy arguments [111].

In order to investigate the electronic behavior of these SnS flat platelets, tunneling spectra were measured at different points of the structure as depicted in Figure 49a. In Figure 49b, one observes the tunneling spectra measured at the points marked with the blue and orange squares at the top of the platelet as depicted in Figure 49a. These spectra exhibit a semiconducting behavior, in agreement with the band structure of SnS. However, our results show an electronic band gap of 1.62 eV at the center and 0.85 eV close to the edge. As is known, STS measurements are proportional to the local electronic density of states of the sample surface.

To further analyze this phenomenon, tunneling spectra were measured along selected paths to elucidate intermediate conditions across the platelet edge, as shown in Figure 49c. These results are depicted in Figure 49d for regions inside and outside the platelet (with a HOPG spectrum at the bottom). These measurements show a significant electronic bandgap variation along the edge, varying from 0.80 up to 1.62 eV. Figure 50 shows a guideline of how the bandgap is measured in the tunneling spectrum. Such behavior was also observed at different platelet borders. These results were corroborated by similar measurements taken from other platelets. The electronic band structure variation may be related to sulfur vacancies, tin vacancies, or other point defects. As reported by Jahangirli *et al*. [112], vacancies lead to dangling bonds on the neighboring atoms and result in a variation in the local density of states.

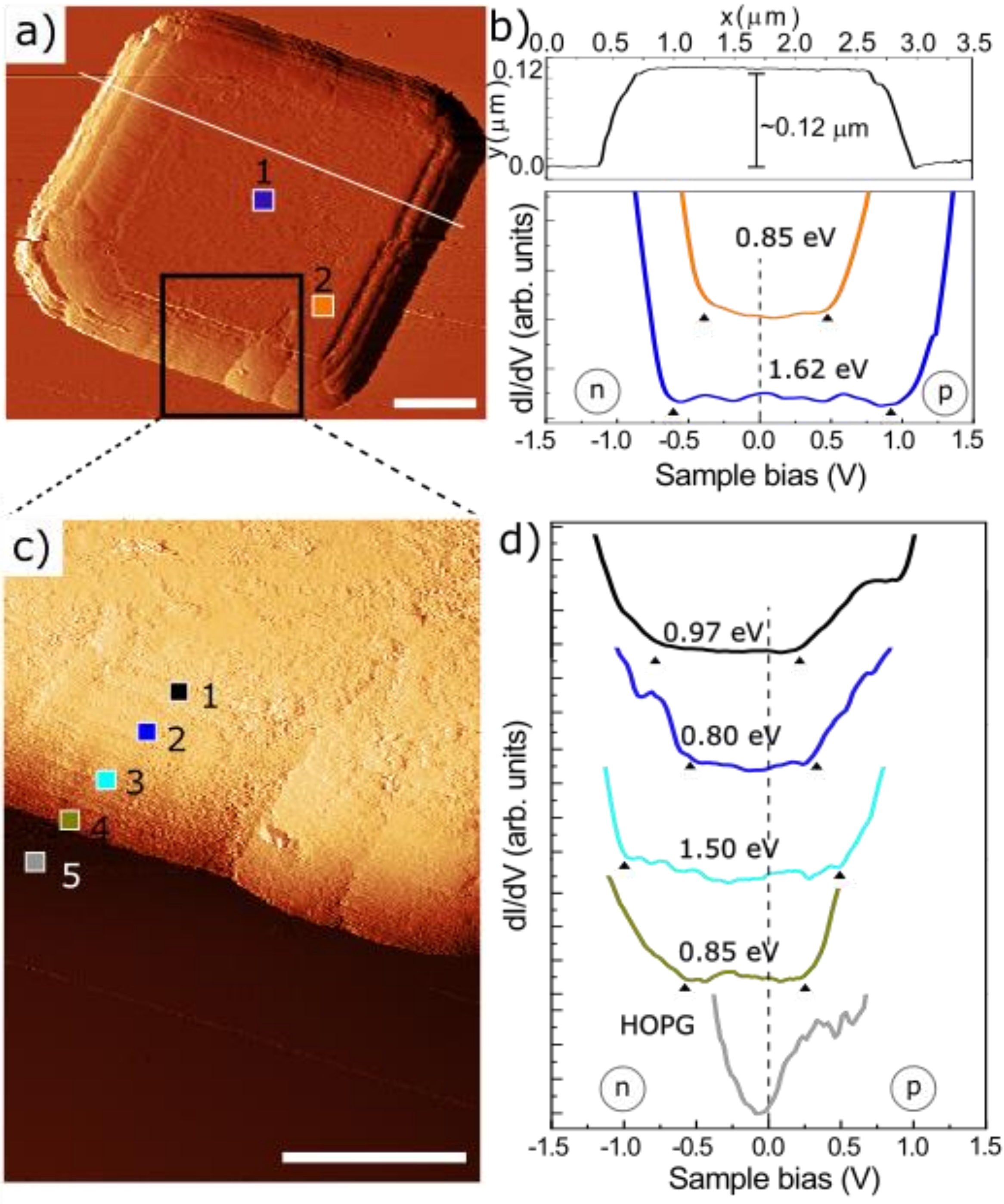

Figure 49. a) STM topography image of an isolated SnS flat platelet grown on HOPG with indications of the tunneling spectra taken (blue and orange square). b) Line profile of topography image Fig. 45a (white line) and STS measurements carried out close to the center (blue curve) and border (orange curve) of the platelet. c) STM image of platelet border with indications of line-scan tunneling spectra along the platelet border (colored squares). d) STS line-scan carried out along the platelet border. In these figures, scale bars are: a): 500 nm and c): 50 nm.

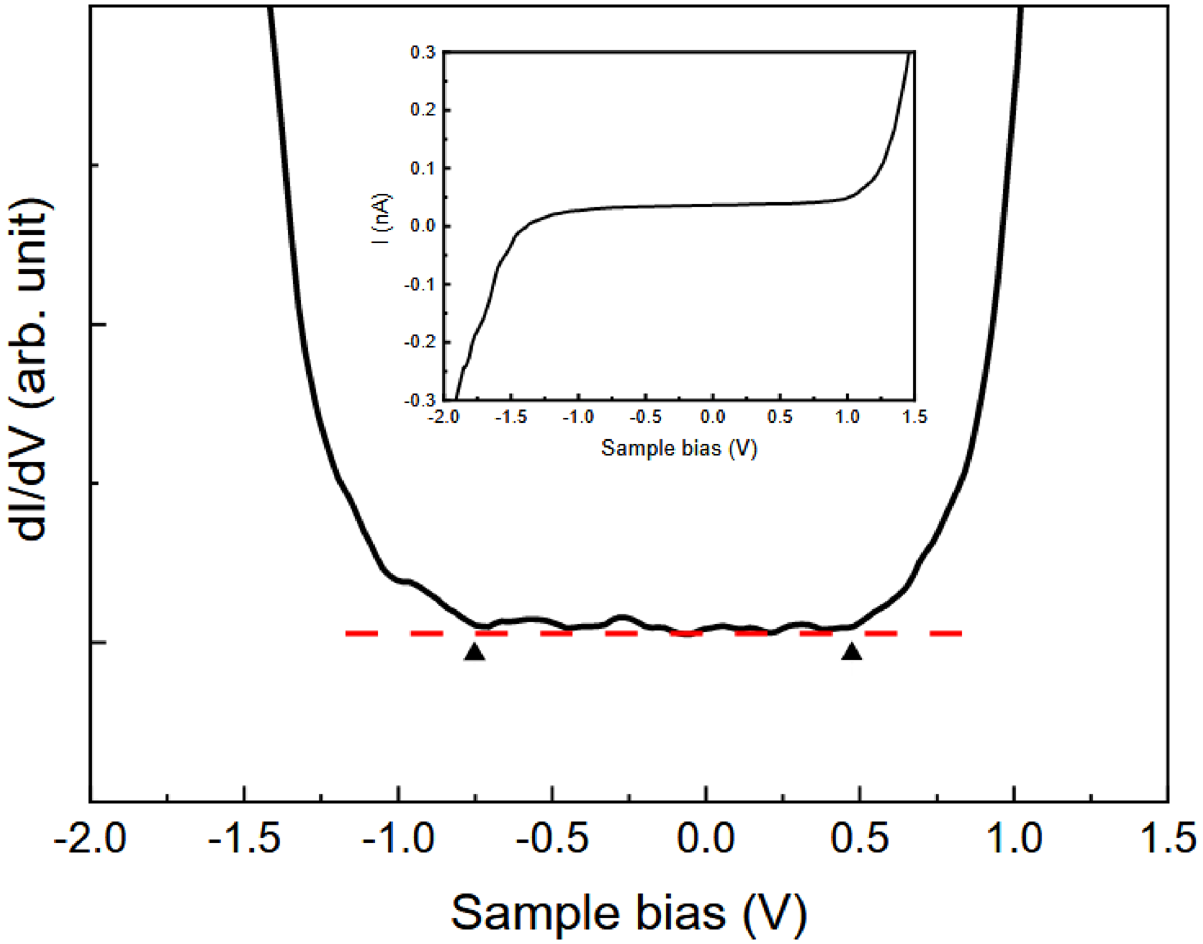

Figure 50. Typical scanning tunneling spectra measured at SnS sample, indicating how the band gap is defined. Inset figure is the equivalent I x V curve.

Vacancy formation plays also a crucial role in determining the conductivity type of the material. A majority of groups have measured PVD-grown SnS with p-type conductivity [14,98,100,101]. Such conductivity arises due to the presence of tin vacancy defects, which generate shallow acceptor-like levels [113]. Figure 51 presents tunneling spectra measured in two distinct parts of a single flat platelet. These platelets are found in isolated conditions, sketched in Figure 51a, or with neighboring flat platelets with a clear boundary, as represented in Figure 51b. Figure 51c depicts a tunneling spectrum typical of an n-type semiconductor behavior, while in Figure 51d, a p-type semiconductor behavior is retrieved. These behaviors are denoted by the Fermi level shift toward the conduction band and the valence band, respectively.

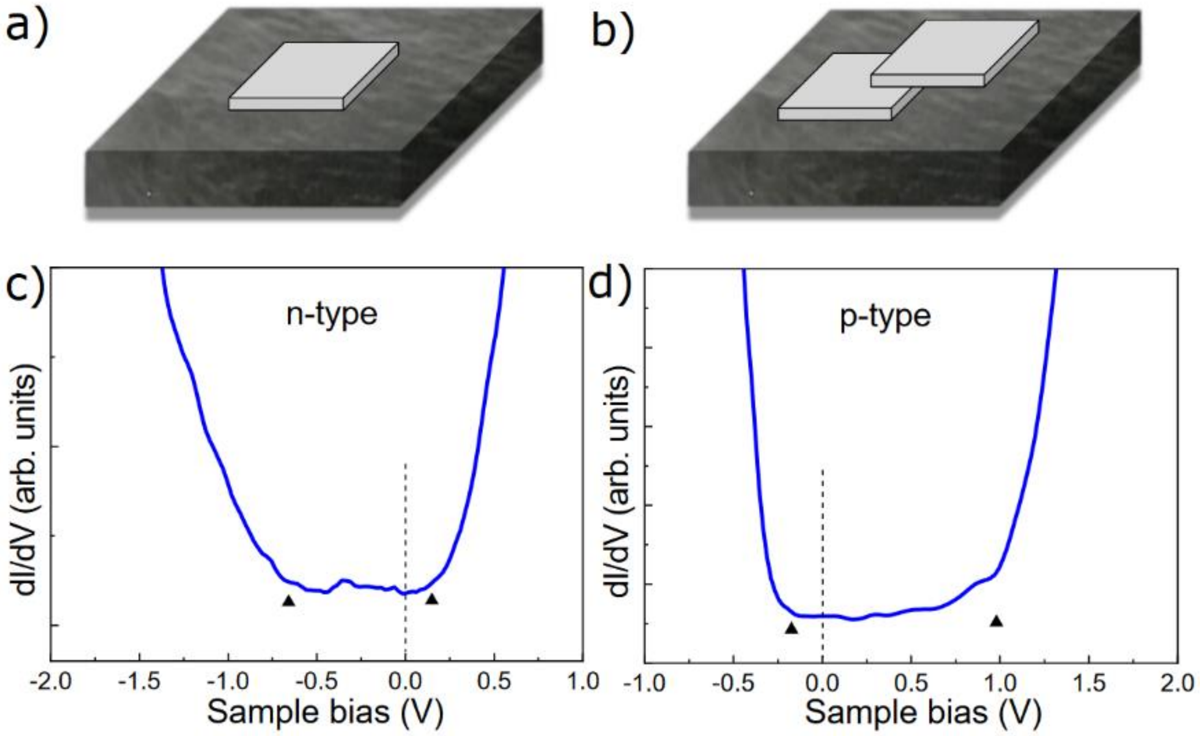

Figure 51. Schematic representation of flat platelets found in isolated condition (a) and with neighbor flat platelets with a clear boundary (b). STS of isolated SnS platelet indicating (c) n-type conductivity and (d) p-type conductivity.

With the doping and bandgap information described in the previous paragraphs, we have carried out grid-like measurements that provide a mapping of these properties along a single flat platelet step. The region defined by a black square limit in Figure 52a and zoomed-in Figure 52b was chosen for the analysis shown here. It provides an overview of two distinct platelets sharing a boundary represented by the white dashed line in Figure 52b. An electronic bandgap map Figure 52c) and a conductivity type map (Figure 52d) were performed by crossing the boundary between flat platelets, in a condition similar to the one sketched in Figure 51b. These plots evidence significant variations in both parameters. Bandgap mapping resulted in a grid with strong variations, ranging from 0.6 eV to 1.5 eV, without any clear correlation with the vicinity of the boundary between platelets or with one of the defined sides. Since for SnS platelets synthesized in this work, one cannot intentionally define p- or n-type semiconductor behavior, the STS minima observed for different measured regions present a considerably strong non-deterministic shift. An approximately equal number of spectra, denoting p- and n-type behavior was found for the mapped region (see Figure 52d). In both STS maps, we have denoted as “contact” grid elements in which a constant-slope curve was observed for a large bias range. Since grid measurements are automated, this condition is compatible with the response of physical contact between probe and sample (see Figure 53 for spectra details).

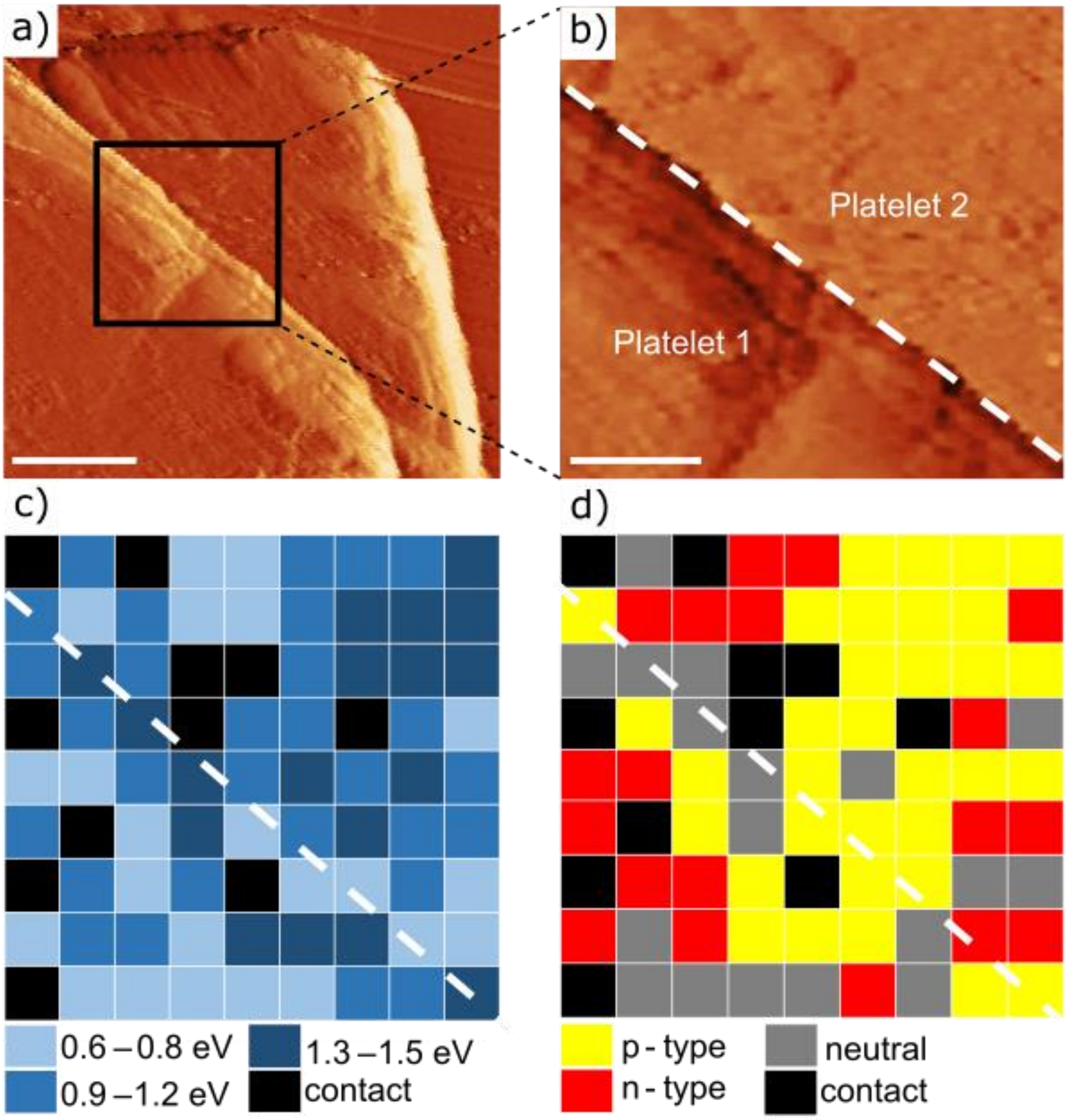

Figure 52. a) STM imaging of a step on a flat SnS platelet. b) Zoomed-in STM image of platelet step (domain boundary highlighted by the white dashed line). c) Electronic band gap map and d) conductivity type map carried out along the platelet step with black dashed line indicating the platelet border. Grid elements in (c) and (d) referred as “contact” indicates positions in which the tip established physical contact with the sample. In these figures, scale bars are: a): 500 nm and b): 200 nm.

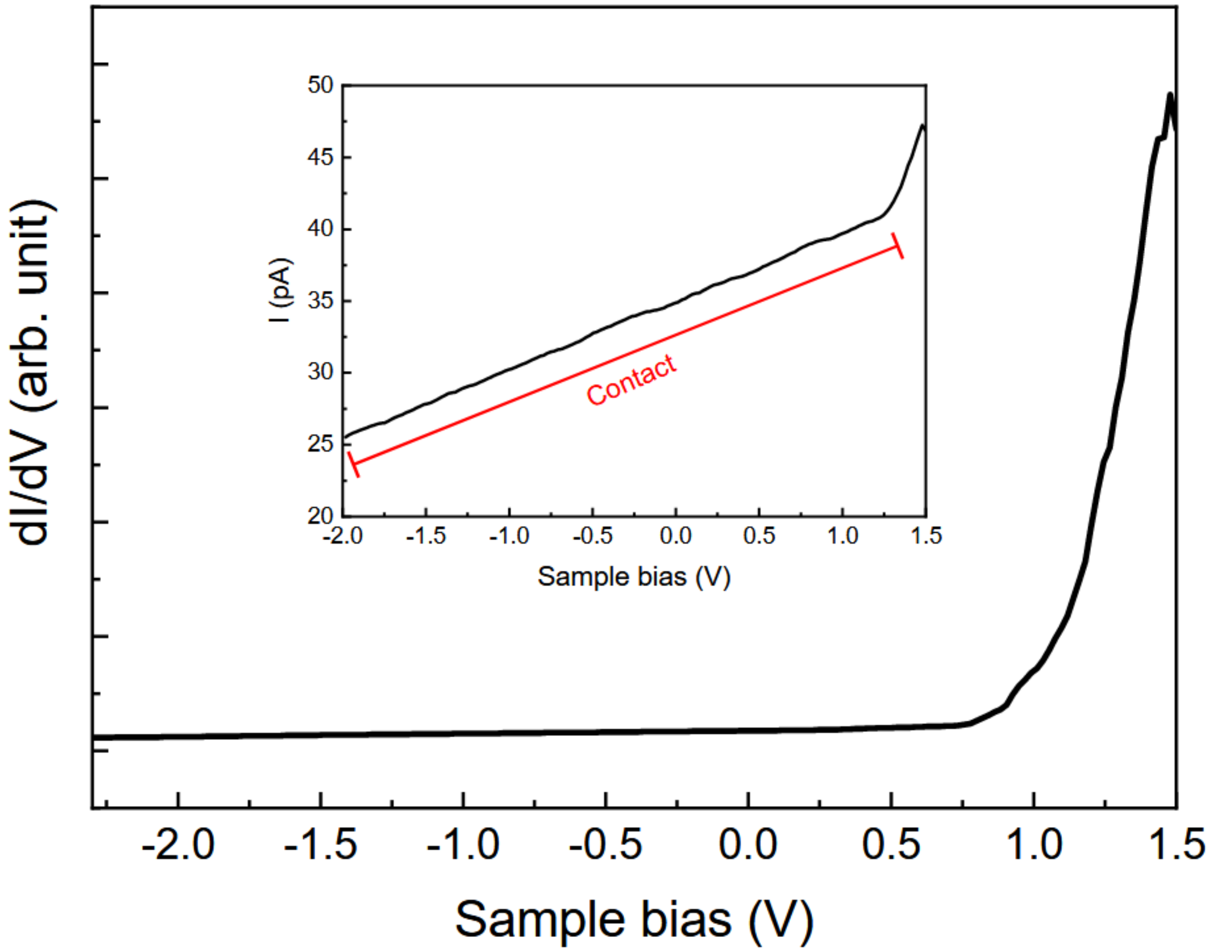

Figure 53. Scanning tunneling spectra and I x V curve (inset) measured at SnS sample, indicating the physical contact between the tip and the sample.

On the opposite side of the same substrate (where the synthesis took place at a lower temperature of 510°C), SnS spiral platelets were grown, as shown in Figure 46c. An STM topographic image is shown in Figure 54a and Figure 54b (zoomed-in image). These platelets exhibit the previously mentioned spiral structure, with monolayer steps. Such structure shape may result from the growth of cubic SnS along the (111) direction. In this axis, the stacking of adjacent SnS layers is irregular, due to the irregular hexagonal symmetry observed in the unit cell [further discussed in Figure 57 (g - h)]. Besides our topographic studies, STS analyses were also carried out for SnS spiral platelets. Figure 54b shows the representation of STS spectral line scans measured at a chosen path across a spiral platelet. The tunneling spectra (Figure 54c) also exhibit a semiconducting behavior, but with a small electronic gap variation.

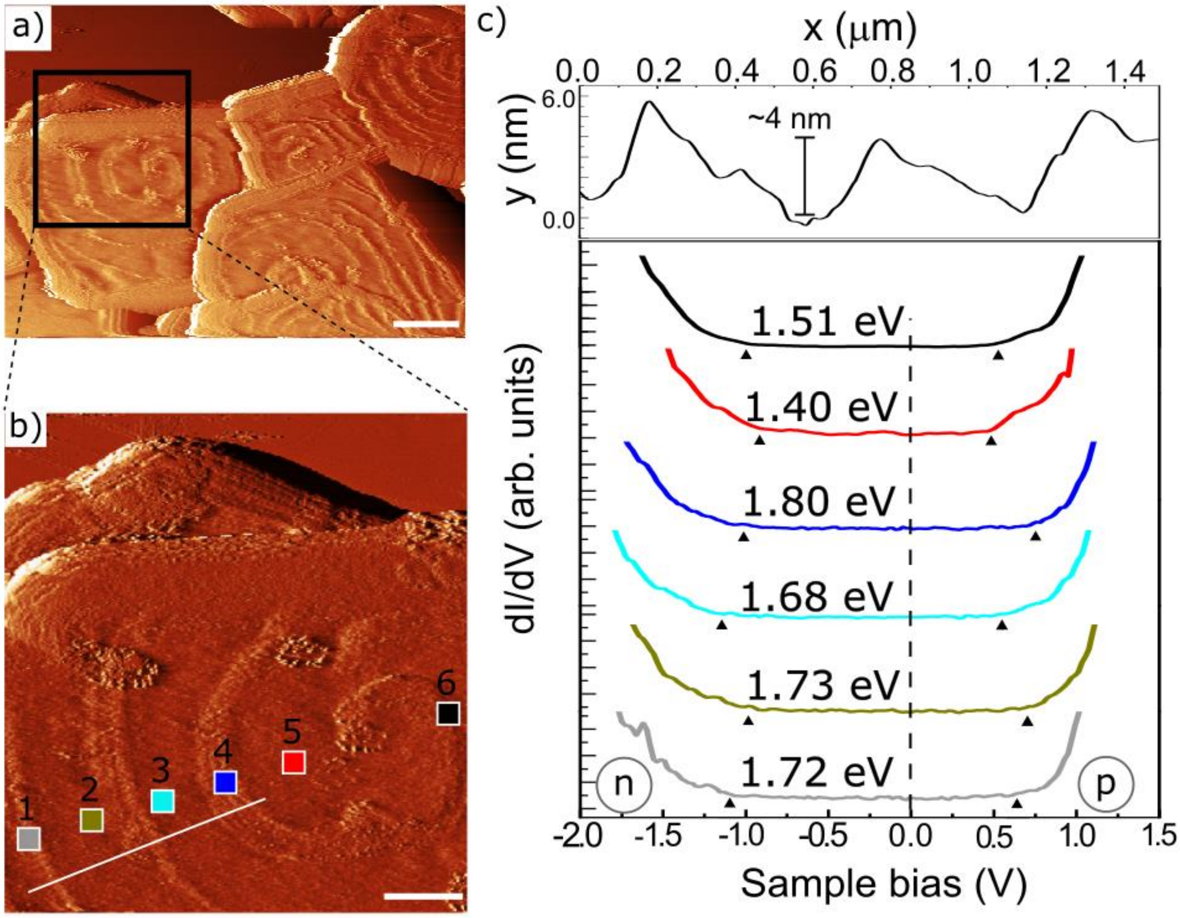

Figure 54. a) STM topography image of SnS spiral platelets. b) Zoomed-in STM topography image of the spiral platelet defined by a black square limit in Fig. 50a with indications of tunneling spectra taken along the surface (colored squares). c) Line profile of topography image Fig. 50b (white line) and STS line-scan carried out along the platelet surface. In this figure scale bars is: a): 1000 nm and b): 500 nm.

Similarly, for the procedure used in Figure 52, an electronic bandgap map and a conductivity map were also produced for the spiral platelets (see Figure 55). Unlike flat platelets, spiral platelets exhibit STS minima denoting a vast majority of semiconducting n-type behavior and a much more homogeneous electronic bandgap along the surface. Such homogeneity condition is mandatory for the development of applications that depend on both electronic properties.

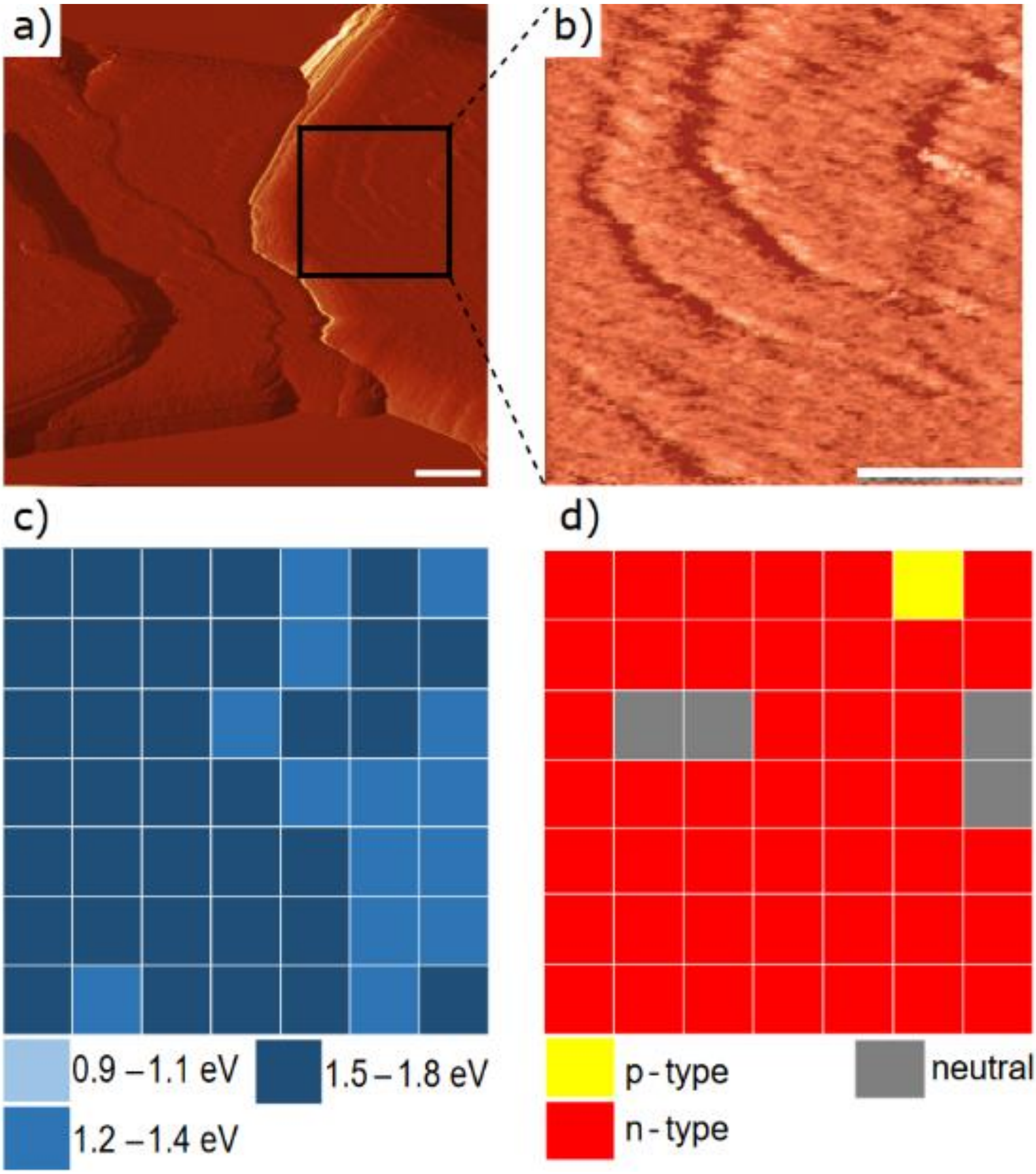

Figure 55. a) STM imaging of a step on a spiral SnS platelet. b) Zoomed-in STM image of spiral platelet. c) Electronic band gap map and d) conductivity type map carried out along the platelet surface with black dashed line indicating the platelet border. In these figures scale bars are: a): 1000 nm and b): 500 nm.

An overall statistical result over several platelets of each type is provided by the histograms of Figure 56. Near 100 platelets were probed for the flat (103 platelets) and spiral (98 platelets) platelet shapes. The retrieved gaps for each phase are shown in Figure 56a and

52c, exhibiting a narrower distribution for the cubic phase (spiral platelets), centered at 1.7 eV. Similar histograms of the Fermi level shift (doping type) were also produced. In these results, shown in Figure 56b and 52d, spiral platelets exhibit a narrow distribution centered at -0.15 eV, indicating better stability of the cubic phase. Platelets with the orthorhombic phase show broad and less defined distributions for gap and Fermi level shift energy values, which impacts their suitability for device fabrication.

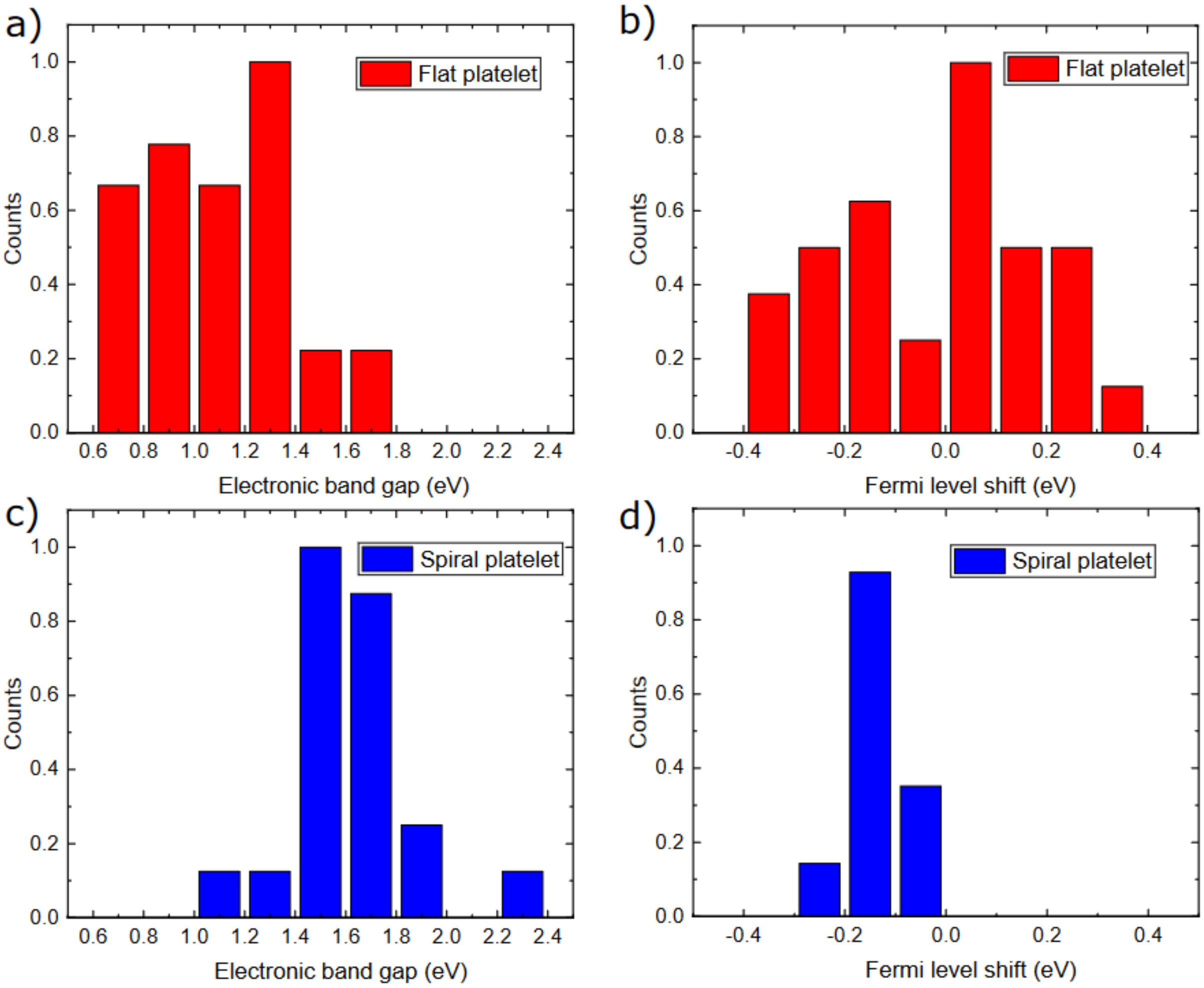

Figure 56. Normalized histograms of electronic band gap and doping type distribution for flat platelets (a and b) and spiral platelets (c and d), respectively.

In order to assure the crystal structure of both types of platelets, TEM and SAED measurements were performed in a group of 10 platelets of each kind. In Figure 57a, TEM results obtained for a typical SnS flat platelet are shown. The dark fringes seen from the platelet are likely due to the bending of the structure and are common to very thin materials.

A zoomed-in TEM image shows the crystallographic orientation of SnS flat platelet in Figure 57b. The diffraction pattern presented in Figure 57c corresponds to the SAED measurement from the same flat platelet shown in Figure 57a. The indices shown in this figure are consistent with the [0 0 1] zone axis, corresponding to the orthorhombic c-axis of the α-SnS phase. It reveals that these rectangular structures are single crystalline and consistent with the α-SnS phase [114], as represented in Figure 57d.

In Figure 57e, a TEM image of a spiral platelet is shown. We observed an inhomogeneous morphology, which is the result of a combination of several individual smaller platelets. Figure 57f, which is a zoomed-in TEM image of Figure 57e, shows these small platelets are in different crystallographic orientations and phases (α-SnS and π-SnS). Different platelets exhibited different SAED patterns. Figure 57g presents a SAED measurement at the region delimited by the blue line in Figure 57f, with a hexagonal diffraction pattern that enabled us to unambiguously determine the correct phase of SnS. We observed that this SAED measurement corresponds to the pattern produced by the less common π-SnS cubic phase in the [1 1 1] direction, as reported recently by several authors [105,115]. The atomic structure of the cubic phase in [1 1 1] orientation is presented in Figure 57h, with a red dashed hexagon that delimits the SnS atoms with the same format and corroborates the SAED analysis. In both cases, the lattice parameters were retrieved with values compatible with reference crystallographic data [116], with a = 0.3978 nm, b = 0.4251 nm, and c = 1.1082 nm for the orthorhombic phase ($\alpha = \beta = \gamma = 90^o$) and a = 1.1506 nm for the cubic phase.

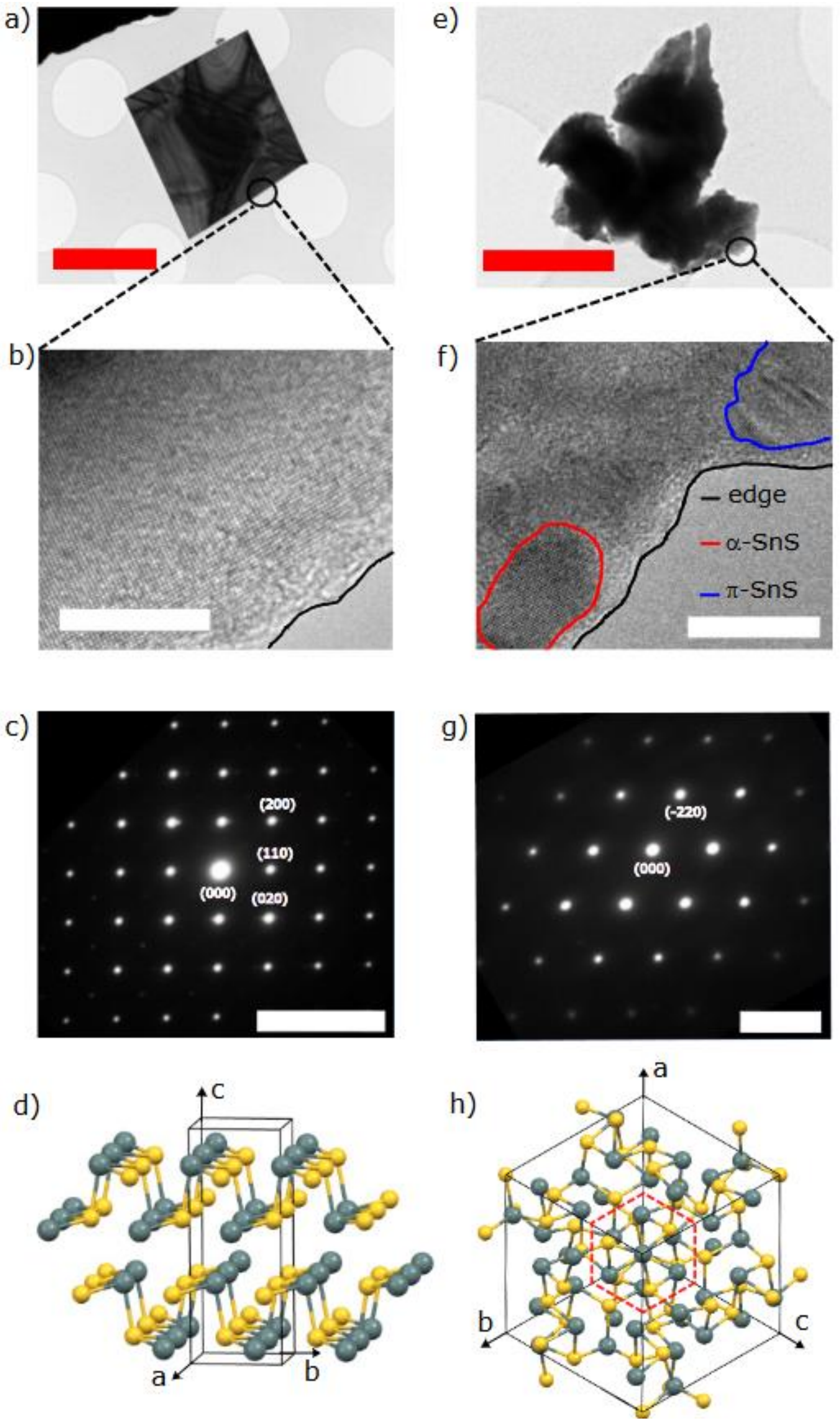

Figure 57. TEM results for both flat (a, b, c, d) and spiral (e, f, g, h) platelets. Fig. 53a and 53e show bright field images of sample pieces containing flat and spiral platelets, respectively. Fig. 53b and 53f are zoomed-in images of Fig. 53a and 53e, respectively. Fig. 53c and 53g present the respectives SAED patterns, indicating that flat plaletets are orthorombic single crystals grown in the [001] direction as well as the cubic crystalline phase in the spiral platelets, measured at region delimited by blue line in Fig. 53f, grown in the [111] direction. Unit cells of orthorombic and cubic ([111] direction) SnS phases are shown in Fig. 53d and 53h, respectively. The red dashed hexagon presented in Fig. 53h delimits SnS atoms in [111] direction that form a hexagon. In these figures scale bars are: a): 2 µm, b): 10 nm, c): 10 1/nm, e): 1 µm, f): 20 nm, g): 10 1/nm.

5.4 Conclusions

In summary, we have synthesized flat and spiral two-dimensional platelets of SnS on a HOPG substrate using vapor phase deposition. EDS and Raman analysis evidenced the absence of other stoichiometric Sn_xS_y phases, while SEM images allowed us to examine the microstructure of the samples. The topographical and electronic properties of the grown structures were studied by STM and STS techniques. Tunneling microscopy measurements revealed the occurrence of flat and spiral SnS platelets. Tunneling spectroscopy measurements evidenced a significant and undesirable variation of electronic bandgap and conductivity for flat platelets. On the other hand, spiral platelets grown at lower synthesis temperatures present better homogeneity of bandgap and conductivity values. Raman spectroscopy, TEM, and SAED measurements demonstrated that the two types of platelets are composed of different SnS structural phases, albeit with the same stoichiometry. Flat platelets are in the α-SnS phase and spiral ones are in the π-SnS one. These results corroborate the STS analysis that indicated that spiral platelets are in the π-SnS phase, with an energy band gap of ~1.7 eV [115].

The observed local electronic bandgap variation and doping fluctuation of flat platelets (α-SnS) may be the most significant cause of the low efficiency of SnS solar cells [14,66,100]. In contrast, the π-SnS phase, due to its homogeneous bandgap and doping, is of potential interest for the production of more efficient SnS-based solar cells and other optoelectronic devices.

6. Experimental demonstration of an environmental-friendly solar cell based on two-dimensional materials GeS and SnS_2

6.1 Introduction

The search for new materials for the production of solar cells has recently become of utmost importance due to the need for environmentally friendly energy. At the same time, the discovery of novel two-dimensional materials has opened the opportunity for alternative solar cells. In particular, the manufacturing of these devices may be facilitated by the ease of production of two-dimensional semiconductors using simple experimental techniques. In this work, we have produced a novel environmentally friendly solar cell based on germanium sulfide (GeS) and tin disulfide (SnS_2). We have used a simple vapor transport method to produce layers with nearly atomically flat surface steps. We have first characterized these materials using STM and energy dispersive electron spectroscopy (EDS). We found that stoichiometric films of these two materials can be easily produced. STS measurements showed that the electronic properties (concerning both bandgap and conductivity type) of the films are close to those expected for bulk materials. The measured electronic bandgaps are especially uniform close to those expected by theoretical modeling. Scanning electron microscopy (SEM) cross-sectional images revealed the thickness of the device's layers. Solar cells using these materials and gold/indium tin oxide (ITO) as contacts have resulted in stable solar cells. These results were based on the density of current versus voltage (J-V) measurements and time-dependent photocurrent response. Remarkably, our solar cells present an intense quantum efficiency (QE), where the crystalline silicon solar cells exhibit a diminished response. Therefore, the use of optimized tandem GeS/SnS_2-silicon solar cells may render cost-effective environmentally friendly devices.

6.2 Experimental methods

N-type SnS_2 buffer layers grown on ITO/glass substrates and studied in this work were synthesized using vapor phase deposition. The process was carried out in a 110 cm long tube reactor with a diameter of 3 cm in a two-zone tubular furnace. The SnS powder source was acquired from MKnano with 99.5% purity and presented an undesired Sn_2S_3 phase. In order to suppress this phase, the powder was thermally treated and purified at 500^oC for 1 h. This procedure was previously optimized and is discussed in detail in ref[88]. To synthesize SnS_2 films, 500 mg of the purified SnS powder was placed at the center of the furnace hot zone (zone 1) in an alumina boat. An ITO/glass substrate, with dimensions of 2×2 cm^2, was placed at a distance of 8 cm downstream from the SnS source. The tube reactor was connected to a vacuum pump and ultrapure argon was injected with a flow rate of 200 sccm for 20 min, to purge the chamber. Afterward, the argon flux was decreased to 110 sccm and the pressure was stabilized to approximately 10^{-1} torr. Subsequently, the furnace was heated with a 30-minute ramp to reach 500^oC at zone 1 and 250^oC at zone 2. In this configuration, the temperature was found to vary from 550^oC to 520^oC along the substrate in the tube longitudinal axis direction. The system was heated for 10 min while SnS vapor was carried downstream and deposited on the substrate. Finally, the system was naturally cooled to room temperature.

A similar process was used to deposit a p-type GeS absorber layer on the SnS_2 buffer layer to obtain a p-n heterojunction. GeS crystals were synthesized through the Bridgman-Stockbarger method. The crystals were transformed into powder and used as precursors to vapor phase deposition. The GeS powder was placed at the center of the furnace hot zone (zone 1) in an alumina boat. The ITO/glass substrate, covered with SnS_2 film, was placed at a distance of 7 cm downstream from the GeS source. The tube reactor was connected to a vacuum pump and ultrapure argon was injected with a flow rate of 200 sccm for 20 min, to purge the chamber. Subsequently, the argon flux was decreased to 50 sccm and the pressure was stabilized in 3.0×10^{-1} torr. The furnace was then heated with a 20-minute ramp to reach 450^oC at zone 1 and 250^oC at zone 2. The system was heated for 10 min while GeS vapor was carried downstream and deposited on the substrate. Finally, the system was naturally cooled to room temperature. The devices were completed by depositing contact metal pads of Au by evaporation.

6.3 Results and discussion

GeS and SnS_2 films grown as described in the experimental methods section by vapor phase deposition were first analyzed by STM and EDS techniques. Figure 58a and 60b present the STM topographic images of both films with indications of height profiles taken along the black and red lines. The black line height profiles indicate a step height of 0.52 nm for GeS (Figure 58c) and 0.60 nm (two steps of 0.30 nm) for SnS_2 (Figure 58d) along the paths marked in the STM images. GeS step value corresponds to a monolayer of atoms (see Figure 15a), while for the SnS_2 a bilayer is measured (see Figure 17a). Furthermore, height profiles along the red lines of STM images indicate a step height of 1.04 nm (two steps of 0.52 nm) for GeS (Figure 58e) and 0.90 nm (three steps of 0.30 nm) for SnS_2 (Figure 58f) that correspond to bilayer and trilayer stacks, respectively. These values are in good agreement with the lattice parameters of both materials [22,117]. These results were corroborated by EDS analysis. Figure 58g and 55h depict the EDS spectra of GeS and SnS_2, respectively. Ge:S and Sn:S atomic ratios close to 1:1 and 1:2 were retrieved, respectively, indicating that the synthesized materials have GeS and SnS_2 stoichiometry and the absence of other undesired phases.

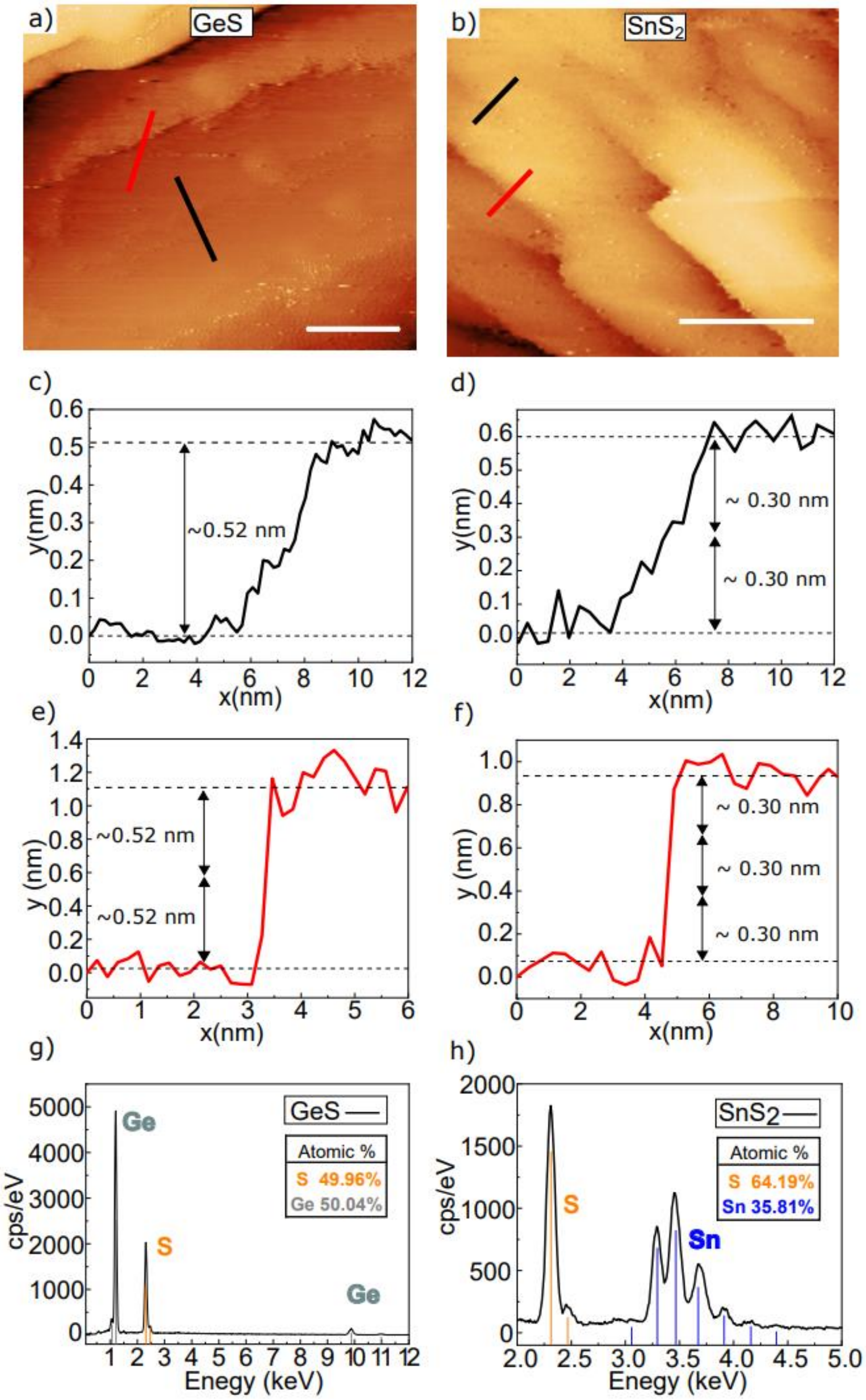

Figure 58. STM and EDS analysis of GeS and SnS_2 films. a) and b) show the STM topography images of GeS and SnS_2 films with indications of height profiles extracted along the black and red lines. c) and d) height profiles retrieved along the black lines in STM images, indicating a monolayer step for GeS and bilayer step of atoms for SnS_2, respectively. e) and f) height profiles taken along the red lines in STM images, presenting a bilayer for GeS and trilayer of atoms for SnS_2, respectively. EDS spectra of (g) GeS and (h) SnS_2 films. In this figure, scale bars (white lines) are a): 10 nm and b) 20 nm.

In order to investigate the electronic behavior of GeS and SnS_2 films, tunneling spectra were measured in several points of both films as depicted in Figure 59. Figure 59a presents 10 representative tunneling spectra (color lines) that were taken along the GeS film surface and their average value (thick grey line). These spectra indicate the electronic behavior of a p-type semiconductor, denoted by the Fermi level shift toward the valence band. Furthermore, an electronic bandgap of 1.28 eV is retrieved, and delimited by the red triangle (bottom of the conduction band) and the green triangle (top of the valence band). On the other hand, for SnS_2, 10 representative tunneling spectra (colored lines) and their average (thick blue line) indicate an *n-type* semiconductor behavior (Figure 59b), with the Fermi level, shifted towards the conduction band. The electronic bandgap (~ 2.27 eV) was also measured similarly to GeS and it agrees with expected experimental values [26]. Using these results we built an energy level diagram presented in Figure 59c, allowing us to visualize the band positions along the interface between the GeS and SnS_2.

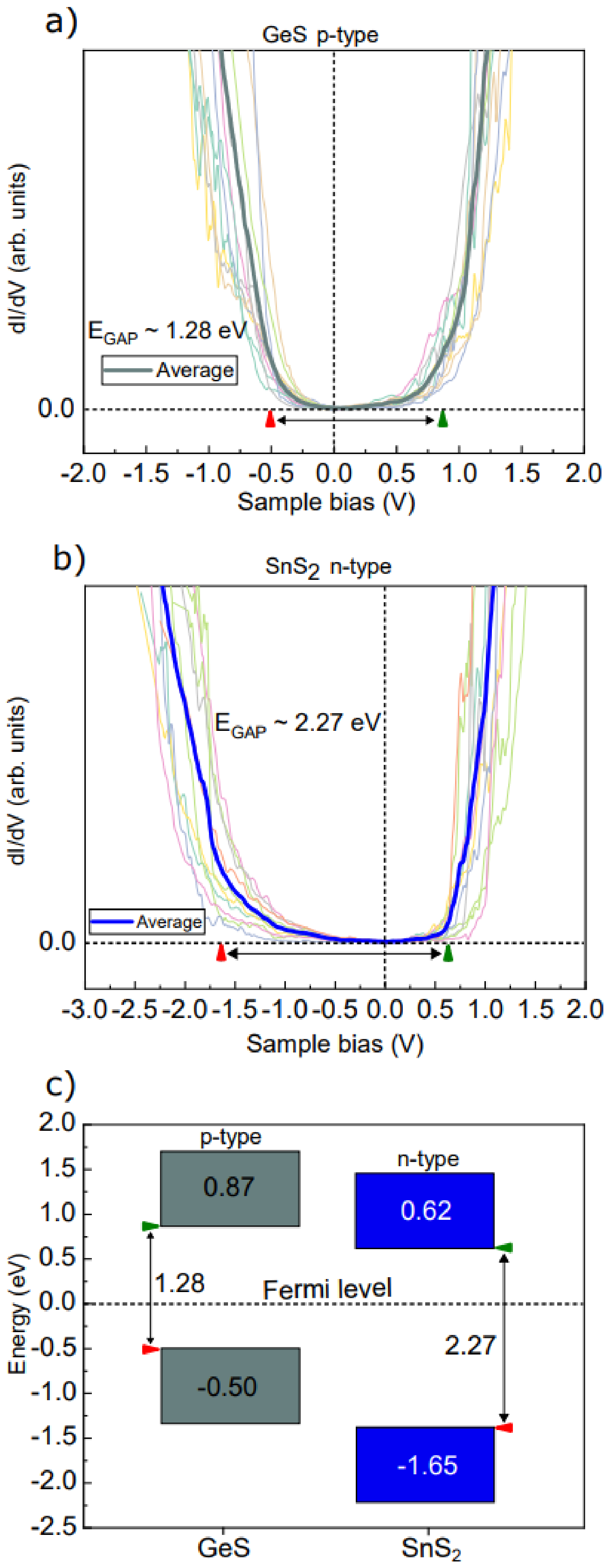

Figure 59. STS of (a) GeS and (b) SnS_2 films. Color lines show individual measurements. The thick line in each panel represents the average value of these curves, indicating (a) p-type GeS films and (b) n-type doping for SnS_2 films. The green and red triangle indicate the bottom of the conduction band and the top of the valence band, respectively c) Schematic energy level diagram of GeS and SnS_2 based on tunneling spectra.

The structure of the final single pn junction solar cell (Au/p-GeS/n-SnS_2/ITO/glass) is presented in Figure 60, with a (a) schematic diagram and a (b) cross-sectional SEM image of the device. Given the interesting properties previously described for GeS, it was taken as the absorber layer. The GeS layer thickness is about 1000 nm (Figure 60b), which was shown to be enough to absorb most of the incident light [17]. As shown in Figure 59c, the SnS_2 layer presents energy band positions that couple well with energy band positions of GeS, forming a p-n junction with an optimal band offset that facilitates the charge collection by the electrodes.

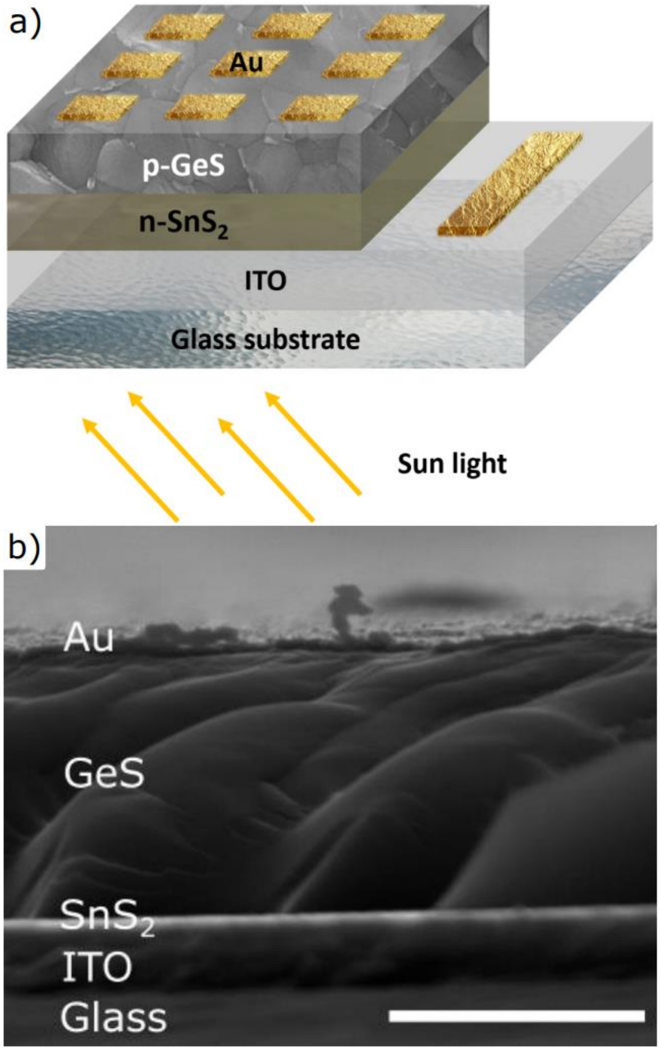

Figure 60. a) Schematic representation of GeS/SnS_2 solar cell structure showing Au contacts atop a p-type GeS layer that interfaces an n-type SnS_2 layer. The system is deposited on a glass substrate covered with an ITO thin film. The cell is illuminate from the bottom side of our representation (yellow arrows). b) Cross-sectional SEM image of a device structure. In this figure, scale bar is b): 1000 nm

Figure 61a shows the systematic variation of J-V curves of a GeS solar cell grown for this work, with respect to the illumination intensity of a solar simulator. The result includes the dark condition and the standard AM1.5G illumination (100 mW cm^{-2}). Forward and reverse curves show no hysteresis. The device presented here exhibits a short-circuit current density (J_{SC}) of 15.8 μAcm^{-2}, an open-circuit (V_{OC}) of 0.42 V, a fill factor (FF) of 24%, and a conversion efficiency (η) of 0.0008%. We also measured the current of our device as a function of time under the AM1.5G illumination. The result is shown in Figure 61b, where 5 cycles of alternating behavior of the current with the light on and off. The reproducibility of photocurrent values indicates the high stability of the device.

Changes in solar cell parameters (J_{SC}, V_{OC}, FF, η) with respect to the amount of GeS powder used during the deposition process are summarized in Figure 62a-d. These results indicate that the amount of powder has a significant influence on the device's performance. Some parameters are modified non-monotonically for the sample series. While V_{OC} decreases from 0.42 to 0.007 V and FF increases from 24 to 32% with the amount of GeS powder. J_{SC} initially decreases significantly from 2000 to 1.15 μAcm^{-2} as the amount of powder increases from 10 to 30 mg. η decreases from 0.002 to 0.000075% along the 10 to 30 mg range. In contrast, albeit all these variations, Tauc plots, depicted in Figure 62e, show identical bandgap values, independently of the used GeS film thickness. Band gaps for our devices were calculated from these Tauc plots using the equation $(\alpha h\nu)^2 = K (h\nu - E_{GAP})$, where K is a constant, h is Planck's constant, ν is the frequency of incident photon, and α = absorbance/thickness. This analysis leads to similar results for electronic bandgap to 1 μm, 600 nm and 500 nm, indicating bulk-like behavior.

The resulting low solar cell efficiency in our prototype cells must be overcome by detailed studies with respect to crystalline domain size, interface quality, and band alignment between the two materials. These issues are known to facilitate photoelectron recombination, reducing the J_{SC} current density. Other optimization issues may arise from growth processes (that may require additional refinement), as well as from the electrode interfaces, which must be optimized for the thin film morphology obtained in our depositions.

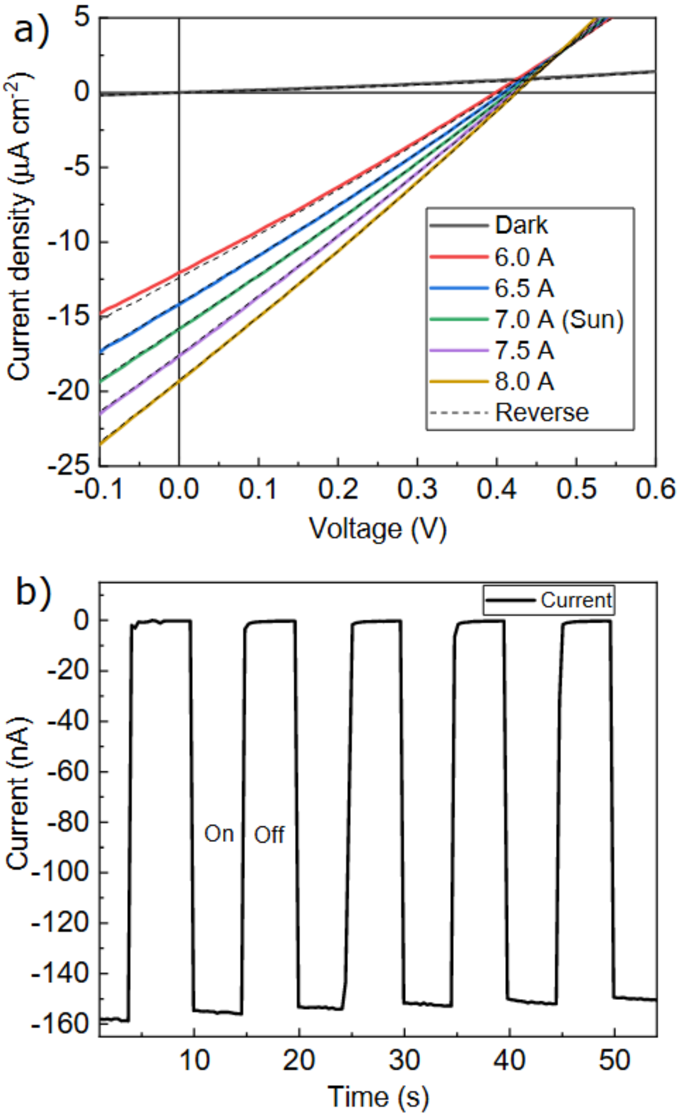

Figure 61. a) J-V curves of GeS device in dark and under different light irradiance, including AM 1.5G illumination. Reverse curves are represented by dashed lines. b) Time-dependent photocurrent response of the device recorded by alternating bright and dark conditions with AM 1.5G illumination.

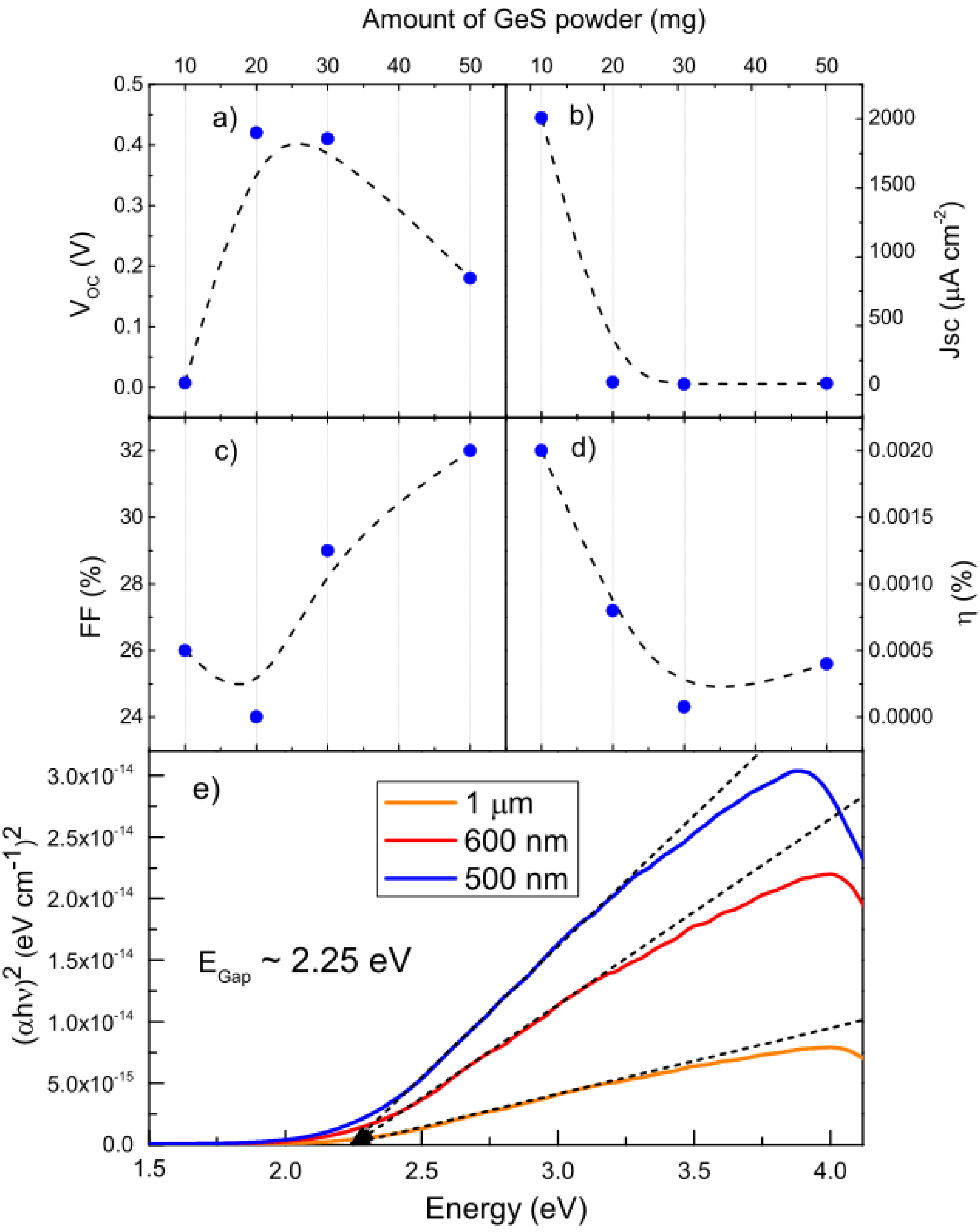

Figure 62. Effect of amount of GeS powder on device parameters under 1-sun illumination for a) V_{OC}, b) J_{SC}, c) FF and d) η e) Tauc plots of GeS/SnS$_2$/ITO/Glass with different estimation GeS film thickness.

Figure 63 shows the solar spectral irradiance at AM1.5G (black) overlapped with the measured quantum efficiencies of our device (GeS/SnS$_2$) (blue) and standard calibrated crystalline silicon (c-Si) (green) solar cell. c-Si solar cells exhibited a broad response in the range of 300 – 1000 nm. Importantly, the GeS/SnS$_2$ device presented an intense response in the vicinity of 400 nm, which corresponds to long-wave ultraviolet (UVA) radiation, where the c-Si device had its quantum efficiency response reduced. These results indicated that if these two cells were put together in tandem cells, one could expect high QE values in a wide range, improving the overall performance of a combined cell with respect to their original junctions.

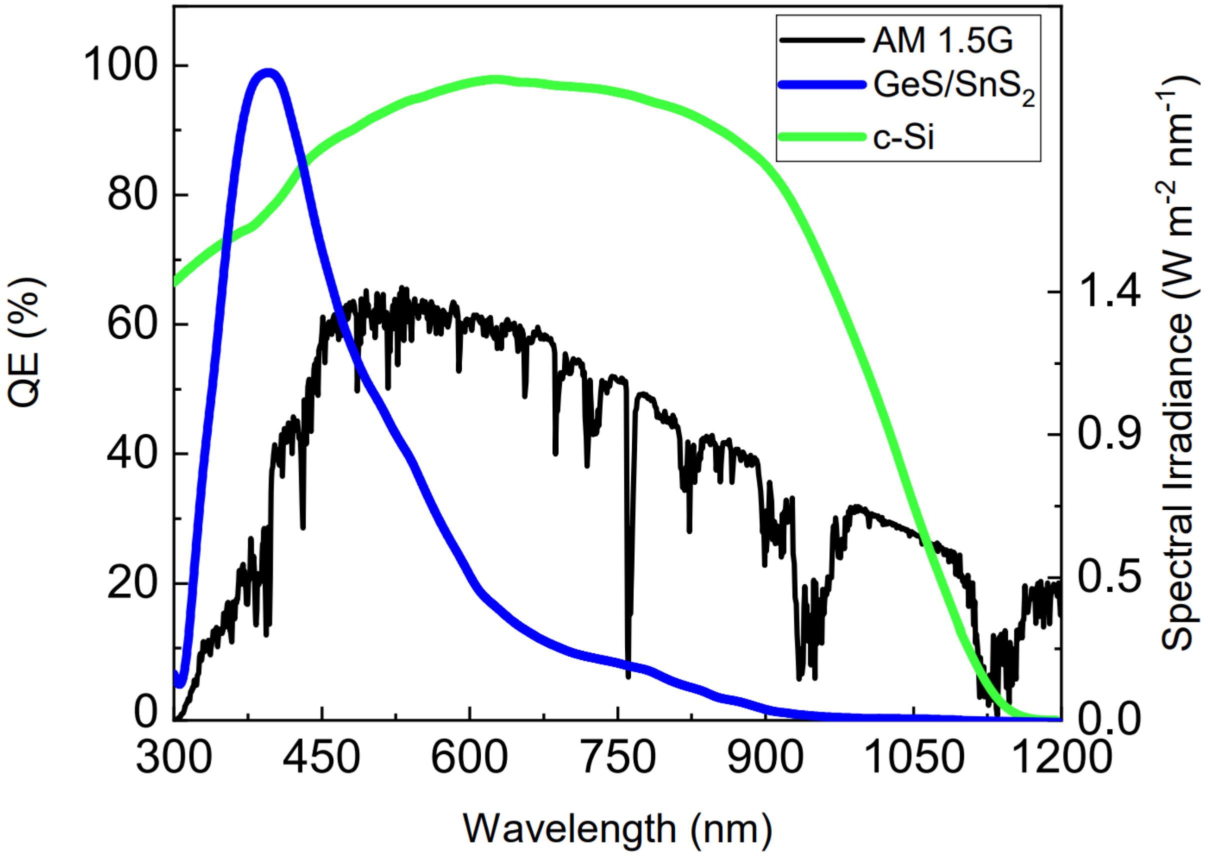

Figure 63. Solar spectral irradiance at AM 1.5G overlapped with measured quantum efficiencies (QE) of GeS/SnS$_2$ and standard calibrated crystalline silicon (c-Si) solar cells.

6.4 Conclusions

In summary, we have produced a solar cell based on environmentally friendly materials (GeS and SnS_2) using a relatively simple vapor phase deposition method. The topographical properties of both films were studied using STM and correlated to the phases discussed here. Chemical composition was corroborated by EDS analysis, indicating the absence of undesired phases for both films. The energy bandgap and conductivity type of each material were measured using STS. SEM cross-sectional images allowed us to measure film thickness. In addition, the photovoltaic properties were analyzed for the GeS/SnS_2 device by varying the GeS thickness. The optimization of the device structure demonstrates that the absorber thickness is 1000 nm. This configuration produces an open circuit (V_{OC}) of 0.42 V, a short circuit current density (JSC) of 15.8 μAcm^{-2}, a fill factor (FF) of 24%, and conversion efficiency (η of 0.0008%, under AM1.5G illumination. Quantum efficiency (QE) measurements of GeS/SnS_2 device evidenced high-energy photon absorption near the long-wave ultraviolet (UVA) radiation of 400 nm. Considering the crystalline Si cells response in the range of 300-1000 nm with diminished QE for values below 450 nm, our results indicate that GeS/SnS_2 can be used as the front cell of tandem devices complementarily to c-Si. This results are a proof of concept for a prototype environmentally friendly based on GeS and SnS_2, Cd-free solar cells. They can be made of two cost-effective binary compounds synthesized by green processes, answering the actual challenge of the use of low-toxicity compounds.

7. Summary and Outlooks

In this thesis, a combination of experimental techniques was used to investigate the synthesis and the structural and electronic properties of SnS, GeS, and SnS_2. Additionally, a solar cell based on a GeS/SnS_2 heterostructure was developed and thoroughly characterized.

In summary, the initial project presented here aimed to investigate SnS grown on HOPG substrates. No other Sn_xS_y phases were detected through EDS and Raman analyses. Additionally, SEM images were used to examine the microstructure of the samples. Scanning tunneling microscopy revealed the occurrence of flat and spiral SnS platelets. While tunneling spectroscopy measurements demonstrated a noteworthy and unfavorable variation in the electronic bandgap and conductivity for flat platelets, spiral platelets, grown at lower temperatures, exhibited better uniformity in bandgap and conductivity values. Raman spectroscopy, TEM, and SAED measurements confirmed that the two types of platelets consist of distinct SnS structural phases, despite sharing the same stoichiometry: α-SnS and π-SnS. These set of results indicates that the observed variations in the bandgap and doping levels of the flat platelets may be the primary reason for the low efficiency of SnS solar cells.

In the second project, a new type of solar cell using GeS and SnS_2 was developed. Our findings indicated that producing stoichiometric films of these two materials is a simple process. These materials were investigated with STS, which revealed that the electronic properties, including bandgap and conductivity type, of the films are comparable to those of the corresponding bulk materials. The thickness of the device layers was measured through cross-sectional images obtained by SEM. Once the electronic and structural properties of these materials were characterized, a prototype solar cell with an Au/p-GeS/n-SnS_2/ITO/glass structure was fabricated. Despite its low efficiency, the solar cell has demonstrated stability, as confirmed by J-V measurements and time-dependent photocurrent response. Furthermore, our solar cells display a high quantum efficiency near long-wave ultraviolet radiation of 400 nm, while the response of crystalline silicon solar cells is reduced for values below 450 nm. This suggests that optimized tandem GeS/SnS_2-silicon solar cells could provide a cost-effective and environmentally-friendly option for use on Earth's surface.

The results obtained here suggest numerous avenues for additional research and experimentation. Specifically, regarding the SnS platelets, there is still potential to refine the recipe for synthesizing both the α and π phases in a precise manner. By altering the growth variables such as pressure, annealing temperatures, and deposition time, it would be possible to investigate how these nanostructures react to such changes. One possible approach to verify this would be to analyze STM images of the as-grown samples. Additionally, by analyzing atomic resolution STM images, it would be possible to gain a deeper understanding of the role played by Sn and S vacancies, as well as other surface defects in SnS and how these factors prevent a better performance of α-SnS-based solar cells and consequently, optimize them.

Regarding the work on GeS/SnS_2 solar cells, it would be beneficial to conduct studies on the interfacial defect states present at the interface between these two materials, using X-ray photoelectron spectroscopy and diffraction. Such defects can act as recombination centers, which can negatively affect the rectification of the J-V curve and ultimately diminish the device's performance. Hall effect measurements could provide insights into the doping density of both the GeS (holes) and SnS_2 (electrons) films. Utilizing this information, one could explore the correlation between the doping density and the observed V_{OC} loss in our device. By enhancing the quality of the films and contacts, it may be possible to improve these parameters, as well as the *FF*, through the synthesis process. Furthermore, introducing an intermediate layer between the SnS_2 film and ITO may enhance adhesion, alleviate tensile strain, and improve the quality of the interface contact.

8. List of publications

The following list contains the works published or submitted until now:

- **Carvalho Ribeiro, T.**; Oliveira, M. H.; Magalhães-Paniago, R.; Ferlauto, A. S. From Thin Films to Shaped Platelets: Effects of Temperature Gradient on SnS Synthesis. *Thin Solid Films* **2021**, *721*, 138507. https://doi.org/10.1016/j.tsf.2020.138507

- **Ribeiro, T. C**.; Reis, R.; Ferreira, D. C.; Miquita, D. R.; Ribeiro, G. A. S.; Mazzoni, M. S. C.; Malachias, A.; Chagas, T.; Magalhaes-Paniago, R. Electronic Gap Stability of Two-Dimensional Tin Monosulfide Phases: Towards Optimal Structures for Electronic Device Applications. *Appl. Surf. Sci.* **2022**, *591* (March), 153153. https://doi.org/10.1016/j.apsusc.2022.153153

- **Ribeiro, T. C.**; Fonseca D.; Reis, R.; Pereira-Andrade E.; Miquita, D. R.; Chagas, T., Malachias, A.; Magalhaes-Paniago, R. Experimental demonstration of an environmental-friendly solar cell based on two-dimensional materials GeS and SnS_2 (submitted to Solar Energy Materials and Solar Cells).

- Reis, R.; **Ribeiro, T. C.**; Fonseca D.; Pereira-Andrade E.; Miquita, D. R.; Chagas, T., Malachias, A.; Magalhaes-Paniago, R. Increased capacitance in few-layer Germanium Monsulfide observed by scanning tunneling microscopy and spectroscopy (to be submitted to Electronic Structure IOP).

- Reis, R.; **Ribeiro, T. C.**; Fonseca D.; Pereira-Andrade E.; Miquita, D. R.; Chagas, T., Malachias, A.; Magalhaes-Paniago, R. Interplay between surface termination and topological gaps in Sb_4Te_3 (to be submitted to Journal of Physical Chemistry Letters).

References

[1] N. Mariotti, M. Bonomo, L. Fagiolari, N. Barbero, C. Gerbaldi, F. Bella, C. Barolo, Recent advances in eco-friendly and cost-effective materials towards sustainable dye-sensitized solar cells, Green Chem. 22 (2020) 7168–7218. https://doi.org/10.1039/D0GC01148G.

[2] M.B. Hayat, D. Ali, K.C. Monyake, L. Alagha, N. Ahmed, Solar energy-A look into power generation, challenges, and a solar-powered future, Int. J. Energy Res. 43 (2019) 1049–1067. https://doi.org/10.1002/er.4252.

[3] G.W. Crabtree, N.S. Lewis, Solar energy conversion, Phys. Today. 60 (2007) 37–42. https://doi.org/10.1063/1.2718755.

[4] A. Slade, V. Garboushian, 27.6% Efficient Silicon Concentrator Solar Cells for Mass Production, Tech. Dig. 15th Int. …. (2005) 1–2. https://www.researchgate.net/publication/267779112%0Ahttps://www.researchgate.net/publication/267779112%0Ahttp://amonix.com/technical_papers/2005/Paper for PVSEC-15 proceedings .pdf.

[5] T.C. Ribeiro, R. Reis, D.C. Ferreira, D.R. Miquita, G.A.S. Ribeiro, M.S.C. Mazzoni, A. Malachias, T. Chagas, R. Magalhaes-Paniago, Electronic gap stability of two-dimensional tin monosulfide phases: Towards optimal structures for electronic device applications, Appl. Surf. Sci. 591 (2022) 153153. https://doi.org/10.1016/j.apsusc.2022.153153.

[6] X. Zhou, L. Gan, Q. Zhang, X. Xiong, H. Li, Z. Zhong, J. Han, T. Zhai, High performance near-infrared photodetectors based on ultrathin SnS nanobelts grown via physical vapor deposition, J. Mater. Chem. C. 4 (2016) 2111–2116. https://doi.org/10.1039/C5TC04410C.

[7] V. Krishnamurthi, H. Khan, T. Ahmed, A. Zavabeti, S.A. Tawfik, S.K. Jain, M.J.S. Spencer, S. Balendhran, K.B. Crozier, Z. Li, L. Fu, M. Mohiuddin, M.X. Low, B. Shabbir, A. Boes, A. Mitchell, C.F. McConville, Y. Li, K. Kalantar-Zadeh, N. Mahmood, S. Walia, Liquid-Metal Synthesized Ultrathin SnS Layers for High-Performance Broadband Photodetectors, Adv. Mater. 32 (2020) 2004247. https://doi.org/10.1002/adma.202004247.

[8] J. Vidal, S. Lany, M. D'Avezac, A. Zunger, A. Zakutayev, J. Francis, J. Tate, M. D'Avezac, A. Zunger, A. Zakutayev, J. Francis, J. Tate, Band-structure, optical properties, and defect physics of the photovoltaic semiconductor SnS, Appl. Phys. Lett. 100 (2012) 10–14. https://doi.org/10.1063/1.3675880.

[9] P. Sinsermsuksakul, J. Heo, W. Noh, A.S. Hock, R.G. Gordon, Atomic Layer Deposition of Tin Monosulfide Thin Films, Adv. Energy Mater. 1 (2011) 1116–1125. https://doi.org/10.1002/aenm.201100330.

[10] M. Patel, A. Chavda, I. Mukhopadhyay, J. Kim, A. Ray, Nanostructured SnS with inherent

anisotropic optical properties for high photoactivity, Nanoscale. 8 (2016) 2293–2303. https://doi.org/10.1039/C5NR06731F.

[11] D. Avellaneda, M.T.S. Nair, P.K. Nair, Polymorphic Tin Sulfide Thin Films of Zinc Blende and Orthorhombic Structures by Chemical Deposition, J. Electrochem. Soc. 155 (2008) D517. https://doi.org/10.1149/1.2917198.

[12] R.E. Banai, H. Lee, M.A. Motyka, R. Chandrasekharan, N.J. Podraza, J.R.S. Brownson, M.W. Horn, Optical Properties of Sputtered SnS Thin Films for Photovoltaic Absorbers, IEEE J. Photovoltaics. 3 (2013) 1084–1089. https://doi.org/10.1109/JPHOTOV.2013.2251758.

[13] S. Hori, T. Suzuki, T. Suzuki, T. Suzuki, S. Nonomura, Synthesis and characterization of tin monosulfide nanosheets, Jpn. J. Appl. Phys. 53 (2014) 021801. https://doi.org/10.7567/JJAP.53.021801.

[14] V. Steinmann, R. Jaramillo, K. Hartman, R. Chakraborty, R.E. Brandt, J.R. Poindexter, Y.S. Lee, L. Sun, A. Polizzotti, H.H. Park, R.G. Gordon, T. Buonassisi, 3.88% Efficient Tin Sulfide Solar Cells using Congruent Thermal Evaporation, Adv. Mater. 26 (2014) 7488–7492. https://doi.org/10.1002/adma.201402219.

[15] P. Ramasamy, D. Kwak, D.-H. Lim, H.-S. Ra, J.-S. Lee, Solution synthesis of GeS and GeSe nanosheets for high-sensitivity photodetectors, J. Mater. Chem. C. 4 (2016) 479–485. https://doi.org/10.1039/C5TC03667D.

[16] E. Sutter, B. Zhang, M. Sun, P. Sutter, Few-Layer to Multilayer Germanium(II) Sulfide: Synthesis, Structure, Stability, and Optoelectronics, ACS Nano. 13 (2019) 9352–9362. https://doi.org/10.1021/acsnano.9b03986.

[17] M. Feng, S.-C. Liu, L. Hu, J. Wu, X. Liu, D.-J. Xue, J.-S. Hu, L.-J. Wan, Interfacial Strain Engineering in Wide-Bandgap GeS Thin Films for Photovoltaics, J. Am. Chem. Soc. 143 (2021) 9664–9671. https://doi.org/10.1021/jacs.1c04734.

[18] X. Fan, L. Su, F. Zhang, D. Huang, D.K. Sang, Y. Chen, Y. Li, F. Liu, J. Li, H. Zhang, H. Xie, Layer-Dependent Properties of Ultrathin GeS Nanosheets and Application in UV–Vis Photodetectors, ACS Appl. Mater. Interfaces. 11 (2019) 47197–47206. https://doi.org/10.1021/acsami.9b14663.

[19] E. Sutter, P. Sutter, 1D Wires of 2D Layered Materials: Germanium Sulfide Nanowires as Efficient Light Emitters, ACS Appl. Nano Mater. 1 (2018) 1042–1049. https://doi.org/10.1021/acsanm.7b00053.

[20] P. Sutter, C. Argyropoulos, E. Sutter, Germanium Sulfide Nano-Optics Probed by STEM-Cathodoluminescence Spectroscopy, Nano Lett. 18 (2018) 4576–4583. https://doi.org/10.1021/acs.nanolett.8b01840.

[21] P. Sutter, S. Wimer, E. Sutter, Chiral twisted van der Waals nanowires, Nature. 570 (2019) 354–357. https://doi.org/10.1038/s41586-019-1147-x.

[22] R.K. Ulaganathan, Y.-Y. Lu, C.-J. Kuo, S.R. Tamalampudi, R. Sankar, K.M. Boopathi, A. Anand, K. Yadav, R.J. Mathew, C.-R. Liu, F.C. Chou, Y.-T. Chen, High photosensitivity and broad spectral response of multi-layered germanium sulfide transistors, Nanoscale. 8 (2016) 2284–2292. https://doi.org/10.1039/C5NR05988G.

[23] C. Lan, C. Li, Y. Yin, H. Guo, S. Wang, Synthesis of single-crystalline GeS nanoribbons for high sensitivity visible-light photodetectors, J. Mater. Chem. C. 3 (2015) 8074–8079. https://doi.org/10.1039/C5TC01435B.

[24] S.C. Dhanabalan, J.S. Ponraj, H. Zhang, Q. Bao, Present perspectives of broadband photodetectors based on nanobelts, nanoribbons, nanosheets and the emerging 2D materials, Nanoscale. 8 (2016) 6410–6434. https://doi.org/10.1039/C5NR09111J.

[25] C. Mondal, M. Ganguly, J. Pal, A. Roy, J. Jana, T. Pal, Morphology controlled synthesis of SnS2 nanomaterial for promoting photocatalytic reduction of aqueous Cr(VI) under visible light, Langmuir. 30 (2014) 4157–4164. https://doi.org/10.1021/la500509c.

[26] Z. Wu, Y. Xue, Y. Zhang, J. Li, T. Chen, SnS2 nanosheet-based microstructures with high adsorption capabilities and visible light photocatalytic activities, RSC Adv. 5 (2015) 24640–24648. https://doi.org/10.1039/c5ra00395d.

[27] Z. Mutlu, R.J. Wu, D. Wickramaratne, S. Shahrezaei, C. Liu, S. Temiz, A. Patalano, M. Ozkan, R.K. Lake, K.A. Mkhoyan, C.S. Ozkan, Phase Engineering of 2D Tin Sulfides, Small. 12 (2016) 2998–3004. https://doi.org/10.1002/smll.201600559.

[28] R.J. Chang, H. Tan, X. Wang, B. Porter, T. Chen, Y. Sheng, Y. Zhou, H. Huang, H. Bhaskaran, J.H. Warner, High-Performance All 2D-Layered Tin Disulfide: Graphene Photodetecting Transistors with Thickness-Controlled Interface Dynamics, ACS Appl. Mater. Interfaces. 10 (2018) 13002–13010. https://doi.org/10.1021/acsami.8b01038.

[29] S. Gedi, S. Alhammadi, J. Noh, V.R. Minnam Reddy, H. Park, A.M. Rabie, J.-J. Shim, D. Kang, W.K. Kim, SnS2 Nanoparticles and Thin Film for Application as an Adsorbent and Photovoltaic Buffer, Nanomaterials. 12 (2022) 282. https://doi.org/10.3390/nano12020282.

[30] A. Sánchez-Juárez, A. Tiburcio-Silver, A. Ortiz, Fabrication of SnS2/SnS heterojunction thin film diodes by plasma-enhanced chemical vapor deposition, Thin Solid Films. 480–481 (2005) 452–456. https://doi.org/10.1016/j.tsf.2004.11.012.

[31] C. Fan, Y. Li, F. Lu, H.-X. Deng, Z. Wei, J. Li, Wavelength dependent UV-Vis photodetectors from SnS 2 flakes, RSC Adv. 6 (2016) 422–427. https://doi.org/10.1039/C5RA24905H.

[32] J.Z. Ou, W. Ge, B. Carey, T. Daeneke, A. Rotbart, W. Shan, Y. Wang, Z. Fu, A.F. Chrimes, W. Wlodarski, S.P. Russo, Y.X. Li, K. Kalantar-zadeh, Physisorption-Based Charge Transfer in Two-Dimensional SnS 2 for Selective and Reversible NO 2 Gas Sensing, ACS Nano. 9 (2015) 10313–10323. https://doi.org/10.1021/acsnano.5b04343.

[33] D. Chao, P. Liang, Z. Chen, L. Bai, H. Shen, X. Liu, X. Xia, Y. Zhao, S. V. Savilov, J. Lin, Z.X. Shen, Pseudocapacitive Na-Ion Storage Boosts High Rate and Areal Capacity of Self-Branched 2D Layered Metal Chalcogenide Nanoarrays, ACS Nano. 10 (2016) 10211–10219. https://doi.org/10.1021/acsnano.6b05566.

[34] N. Parveen, S.A. Ansari, H.R. Alamri, M.O. Ansari, Z. Khan, M.H. Cho, Facile Synthesis of SnS 2 Nanostructures with Different Morphologies for High-Performance Supercapacitor Applications, ACS Omega. 3 (2018) 1581–1588. https://doi.org/10.1021/acsomega.7b01939.

[35] Y. Wang, L. Huang, Z. Wei, Photoresponsive field-effect transistors based on multilayer SnS 2 nanosheets, J. Semicond. 38 (2017) 034001. https://doi.org/10.1088/1674-4926/38/3/034001.

[36] M.A. Green, Solar Cells Operating Principles Technology and System Applications, Prentice Hall. (1982). https://doi.org/https://doi.org/10.3390/ma15165542.

[37] R. Williams, Becquerel Photovoltaic Effect in Binary Compounds, J. Chem. Phys. 32 (1960) 1505–1514. https://doi.org/10.1063/1.1730950.

[38] N. Amin, S. Ahmad Shahahmadi, P. Chelvanathan, K.S. Rahman, M. Istiaque Hossain, M.D. Akhtaruzzaman, Solar Photovoltaic Technologies: From Inception Toward the Most Reliable Energy Resource, in: Encycl. Sustain. Technol., Elsevier, 2017: pp. 11–26. https://doi.org/10.1016/B978-0-12-409548-9.10092-2.

[39] J. Pastuszak, P. Węgierek, Photovoltaic Cell Generations and Current Research Directions for Their Development, Materials (Basel). 15 (2022) 5542. https://doi.org/10.3390/ma15165542.

[40] J.F. Geisz, R.M. France, K.L. Schulte, M.A. Steiner, A.G. Norman, H.L. Guthrey, M.R. Young, T. Song, T. Moriarty, Six-junction III–V solar cells with 47.1% conversion efficiency under 143 Suns concentration, Nat. Energy. 5 (2020) 326–335. https://doi.org/10.1038/s41560-020-0598-5.

[41] W. Metaferia, K.L. Schulte, J. Simon, S. Johnston, A.J. Ptak, Gallium arsenide solar cells grown at rates exceeding 300 µm h−1 by hydride vapor phase epitaxy, Nat. Commun. 10 (2019) 3361. https://doi.org/10.1038/s41467-019-11341-3.

[42] M. Nakamura, K. Yamaguchi, Y. Kimoto, Y. Yasaki, T. Kato, H. Sugimoto, Cd-Free Cu(In,Ga)(Se,S) 2 Thin-Film Solar Cell With Record Efficiency of 23.35%, IEEE J. Photovoltaics. 9 (2019) 1863–1867. https://doi.org/10.1109/JPHOTOV.2019.2937218.

[43] C. Prouskas, A. Mourkas, G. Zois, E. Lidorikis, P. Patsalas, A New Type of Architecture of Dye-Sensitized Solar Cells as an Alternative Pathway to Outdoor Photovoltaics, Energies. 15 (2022) 2486. https://doi.org/10.3390/en15072486.

[44] M. Jošt, L. Kegelmann, L. Korte, S. Albrecht, Monolithic Perovskite Tandem Solar Cells: A Review of the Present Status and Advanced Characterization Methods Toward 30% Efficiency, Adv. Energy Mater. 10 (2020) 1904102. https://doi.org/10.1002/aenm.201904102.

[45] W. Shockley, H.J. Queisser, Detailed Balance Limit of Efficiency of p-n Junction Solar Cells, J. Appl. Phys. 32 (1961) 510–519. https://doi.org/10.1063/1.1736034.

[46] D.K. Schroder, MATERIAL AND DEVICE SEMICONDUCTOR MATERIAL AND DEVICE Third Edition, John Wiley & SonS, Inc., Hoboken, NJ, USA, 2005.

[47] A. Polman, M. Knight, E.C. Garnett, B. Ehrler, W.C. Sinke, Photovoltaic materials: Present efficiencies and future challenges, Science (80-.). 352 (2016) aad4424–aad4424. https://doi.org/10.1126/science.aad4424.

[48] J. Wang, Open-circuit voltage, fill factor, and heterojunction band offset in semiconductor diode solar cells, EcoMat. 4 (2022) 1–10. https://doi.org/10.1002/eom2.12263.

[49] S. Li, Z. Peng, J. Zheng, F. Pan, Optimizing CdTe–metal interfaces for high performance solar cells, J. Mater. Chem. A. 5 (2017) 7118–7124. https://doi.org/10.1039/C7TA00698E.

[50] Z. Tian, C. Guo, M. Zhao, R. Li, J. Xue, Two-Dimensional SnS: A Phosphorene Analogue with Strong In-Plane Electronic Anisotropy, ACS Nano. 11 (2017) 2219–2226. https://doi.org/10.1021/acsnano.6b08704.

[51] V. Stevanović, K. Hartman, R. Jaramillo, S. Ramanathan, T. Buonassisi, P. Graf, Variations of ionization potential and electron affinity as a function of surface orientation: The case of orthorhombic SnS, Appl. Phys. Lett. 104 (2014) 211603. https://doi.org/10.1063/1.4879558.

[52] R. Guo, X. Wang, Y. Kuang, B. Huang, First-principles study of anisotropic thermoelectric transport properties of IV-VI semiconductor compounds SnSe and SnS, Phys. Rev. B - Condens. Matter Mater. Phys. 92 (2015) 1–13. https://doi.org/10.1103/PhysRevB.92.115202.

[53] A.R. Garcia-Angelmo, R. Romano-Trujillo, J. Campos-Álvarez, O. Gomez-Daza, M.T.S. Nair, P.K. Nair, Thin film solar cell of SnS absorber with cubic crystalline structure, Phys. Status Solidi. 212 (2015) 2332–2340. https://doi.org/10.1002/pssa.201532405.

[54] O. V. Bilousov, Y. Ren, T. Törndahl, O. Donzel-Gargand, T. Ericson, C. Platzer-Björkman,

M. Edoff, C. Hägglund, Atomic Layer Deposition of Cubic and Orthorhombic Phase Tin Monosulfide, Chem. Mater. 29 (2017) 2969–2978. https://doi.org/10.1021/acs.chemmater.6b05323.

[55] I.Y. Ahmet, M.S. Hill, A.L. Johnson, L.M. Peter, Polymorph-Selective Deposition of High Purity SnS Thin Films from a Single Source Precursor, Chem. Mater. 27 (2015) 7680–7688. https://doi.org/10.1021/acs.chemmater.5b03220.

[56] M. Patel, A. Chavda, I. Mukhopadhyay, J. Kim, A. Ray, Nanostructured SnS with inherent anisotropic optical properties for high photoactivity, Nanoscale. 8 (2016) 2293–2303. https://doi.org/10.1039/c5nr06731f.

[57] A. Javed, N. Khan, S. Bashir, M. Ahmad, M. Bashir, Thickness dependent structural, electrical and optical properties of cubic SnS thin films, Mater. Chem. Phys. 246 (2020) 122831. https://doi.org/10.1016/j.matchemphys.2020.122831.

[58] K. Jeganath, N.J. Choudhari, G. Shruthi Pai, A. Rao, Y. Raviprakash, Role of substrate temperature on spray pyrolysed metastable π-SnS thin films, Mater. Sci. Semicond. Process. 113 (2020) 105050. https://doi.org/10.1016/j.mssp.2020.105050.

[59] K.O. Hara, S. Suzuki, N. Usami, Formation of metastable cubic phase in SnS thin films fabricated by thermal evaporation, Thin Solid Films. 639 (2017) 7–11. https://doi.org/10.1016/j.tsf.2017.08.025.

[60] M.S. Mahdi, N.M. Ahmed, A. Hmood, K. Ibrahim, M. Bououdina, Comprehensive photoresponse study on high performance and flexible π-SnS photodetector with near-infrared response, Mater. Sci. Semicond. Process. 100 (2019) 270–274. https://doi.org/10.1016/j.mssp.2019.05.019.

[61] S.U. Rehman, F.K. Butt, B. Ul Haq, S. AlFaify, W.S. Khan, C. Li, Exploring novel phase of tin sulfide for photon/energy harvesting materials, Sol. Energy. 169 (2018) 648–657. https://doi.org/10.1016/j.solener.2018.05.006.

[62] V.E. González-Flores, R.N. Mohan, R. Ballinas-Morales, M.T.S. Nair, P.K. Nair, Thin film solar cells of chemically deposited SnS of cubic and orthorhombic structures, Thin Solid Films. 672 (2019) 62–65. https://doi.org/10.1016/j.tsf.2018.12.044.

[63] R.D. Engelken, H.E. McCloud, C. Lee, M. Slayton, H. Ghoreishi, Low Temperature Chemical Precipitation and Vapor Deposition of Sn x S Thin Films, J. Electrochem. Soc. 134 (1987) 2696–2707. https://doi.org/10.1149/1.2100274.

[64] M. Ristov, G. Sinadinovski, I. Grozdanov, M. Mitreski, Chemical deposition of TIN(II) sulphide thin films, Thin Solid Films. 173 (1989) 53–58. https://doi.org/10.1016/0040-6090(89)90536-1.

[65] S. Rühle, Tabulated values of the Shockley–Queisser limit for single junction solar cells,

Sol. Energy. 130 (2016) 139–147. https://doi.org/10.1016/j.solener.2016.02.015.

[66] P. Sinsermsuksakul, L. Sun, S.W. Lee, H.H. Park, S.B. Kim, C. Yang, R.G. Gordon, Overcoming Efficiency Limitations of SnS-Based Solar Cells, Adv. Energy Mater. 4 (2014) 1–7. https://doi.org/10.1002/aenm.201400496.

[67] H. Yun, B. Park, Y.C. Choi, J. Im, T.J. Shin, S. Il Seok, Efficient Nanostructured TiO 2 /SnS Heterojunction Solar Cells, Adv. Energy Mater. 9 (2019) 1901343. https://doi.org/10.1002/aenm.201901343.

[68] J.D. Wiley, A. Breitschwerdt, E. Schönherr, Optical absorption band edge in single-crystal GeS, Solid State Commun. 17 (1975) 355–359. https://doi.org/10.1016/0038-1098(75)90311-7.

[69] J.D. Wiley, S. Pennington, E. Schönherr, Anisotropy of the intrinsic photoconductivity of GeS, Phys. Status Solidi. 96 (1979) K43–K46. https://doi.org/10.1002/pssb.2220960163.

[70] R. Fei, W. Kang, L. Yang, Ferroelectricity and Phase Transitions in Monolayer Group-IV Monochalcogenides, Phys. Rev. Lett. 117 (2016) 097601. https://doi.org/10.1103/PhysRevLett.117.097601.

[71] M. Wu, X.C. Zeng, Intrinsic Ferroelasticity and/or Multiferroicity in Two-Dimensional Phosphorene and Phosphorene Analogues, Nano Lett. 16 (2016) 3236–3241. https://doi.org/10.1021/acs.nanolett.6b00726.

[72] R. Fei, W. Li, J. Li, L. Yang, Giant piezoelectricity of monolayer group IV monochalcogenides: SnSe, SnS, GeSe, and GeS, Appl. Phys. Lett. 107 (2015) 173104. https://doi.org/10.1063/1.4934750.

[73] C. Li, L. Huang, G.P. Snigdha, Y. Yu, L. Cao, Role of Boundary Layer Diffusion in Vapor Deposition Growth of Chalcogenide Nanosheets: The Case of GeS, ACS Nano. 6 (2012) 8868–8877. https://doi.org/10.1021/nn303745e.

[74] Y. Chen, M. Zhang, Large-area growth of SnS 2 nanosheets by chemical vapor deposition for high-performance photodetectors, RSC Adv. 11 (2021) 29960–29964. https://doi.org/10.1039/D1RA05779K.

[75] Z. HADEF, K. KAMLI, Effect of molar concentration on the properties of SnS2 thin films prepared by spray pyrolysis, Mater. Today Proc. 49 (2022) 1079–1083. https://doi.org/10.1016/j.matpr.2021.09.330.

[76] B. Eghbalifar, H. Izadneshan, G. Solookinejad, L. Separdar, Investigating In2S3 as the buffer layer in CZTSSe solar cells using simulation and experimental approaches, Solid State Commun. 343 (2022) 114654. https://doi.org/10.1016/j.ssc.2022.114654.

[77] G.R. Gopinath, K.T. Ramakrishna Reddy, Growth of Polycrystalline In 2 S 3 Thin Films by Chemical Bath Deposition Using Acetic Acid as a Complexing Agent for Solar Cell Application, ISRN Condens. Matter Phys. 2013 (2013) 1–6. https://doi.org/10.1155/2013/140230.

[78] T. Miyawaki, M. Ichimura, Fabrication of ZnS thin films by an improved photochemical deposition method and application to ZnS/SnS heterojunction cells, Mater. Lett. 61 (2007) 4683–4686. https://doi.org/10.1016/j.matlet.2007.03.006.

[79] M.M. Islam, S. Ishizuka, A. Yamada, K. Sakurai, S. Niki, T. Sakurai, K. Akimoto, CIGS solar cell with MBE-grown ZnS buffer layer, Sol. Energy Mater. Sol. Cells. 93 (2009) 970–972. https://doi.org/10.1016/j.solmat.2008.11.047.

[80] D. Agrawal, D. Suthar, R. Agarwal, Himanshu, S.L. Patel, M.S. Dhaka, Achieving desired quality of ZnS buffer layer by optimization using air annealing for solar cell applications, Phys. Lett. A. 384 (2020) 126557. https://doi.org/10.1016/j.physleta.2020.126557.

[81] B. Ghosh, M. Das, P. Banerjee, S. Das, Fabrication of the SnS/ZnO heterojunction for PV applications using electrodeposited ZnO films, Semicond. Sci. Technol. 24 (2009) 025024. https://doi.org/10.1088/0268-1242/24/2/025024.

[82] H.-K. Kim, K.-B. Chung, J. Kal, Comparison of ZnO buffer layers prepared by spin coating or RF magnetron sputtering for application in inverted organic solar cells, J. Alloys Compd. 778 (2019) 487–495. https://doi.org/10.1016/j.jallcom.2018.11.240.

[83] Y. Wang, H. Gong, B. Fan, G. Hu, Photovoltaic Behavior of Nanocrystalline SnS/TiO 2, J. Phys. Chem. C. 114 (2010) 3256–3259. https://doi.org/10.1021/jp9075756.

[84] P.P. Rajbhandari, T.P. Dhakal, Low temperature ALD growth optimization of ZnO, TiO 2 , and Al 2 O 3 to be used as a buffer layer in perovskite solar cells, J. Vac. Sci. Technol. A. 38 (2020) 032406. https://doi.org/10.1116/1.5139247.

[85] T. Ikuno, R. Suzuki, K. Kitazumi, N. Takahashi, N. Kato, K. Higuchi, SnS thin film solar cells with Zn1−xMgxO buffer layers, Appl. Phys. Lett. 102 (2013) 193901. https://doi.org/10.1063/1.4804603.

[86] J.Y. Cho, S. Kim, R. Nandi, J. Jang, H.-S. Yun, E. Enkhbayar, J.H. Kim, D.-K. Lee, C.-H. Chung, J. Kim, J. Heo, Achieving over 4% efficiency for SnS/CdS thin-film solar cells by improving the heterojunction interface quality, J. Mater. Chem. A. 8 (2020) 20658–20665. https://doi.org/10.1039/D0TA06937J.

[87] J.Y. Cho, S. Sinha, M.G. Gang, J. Heo, Controlled thickness of a chemical-bath-deposited CdS buffer layer for a SnS thin film solar cell with more than 3% efficiency, J. Alloys Compd. 796 (2019) 160–166. https://doi.org/10.1016/j.jallcom.2019.05.035.

[88] T. Carvalho Ribeiro, M.H. Oliveira, R. Magalhães-Paniago, A.S. Ferlauto, From thin films

to shaped platelets: effects of temperature gradient on SnS synthesis, Thin Solid Films. 721 (2021) 138507. https://doi.org/10.1016/j.tsf.2020.138507.

[89] M. Schmidt, R. Kusche, B. von Issendorff, H. Haberland, Irregular variations in the melting point of size-selected atomic clusters, Nature. 393 (1998) 238–240. https://doi.org/10.1038/30415.

[90] M. Li, Y. Wu, T. Li, Y. Chen, H. Ding, Y. Lin, N. Pan, X. Wang, Revealing anisotropy and thickness dependence of Raman spectra for SnS flakes, RSC Adv. 7 (2017) 48759–48765. https://doi.org/10.1039/C7RA09430B.

[91] D.B.W. and C.B. Carter, Transmission Electron Microscopy, Springer US, 2009.

[92] L.S. J. Goldstein, D. E. Newbury, D. C. Joy, C. E. Lyman, P. Echlin, E. Lifshin, and J.R. Michael, Scanning Electron Microscopy and X-ray Microanalysis, 3rd ed., Springer US, 2003.

[93] G. Binnig, H. Rohrer, Scanning tunneling microscopy, Surf. Sci. 126 (1983) 236–244. https://doi.org/10.1016/0039-6028(83)90716-1.

[94] T. Chagas, TUNNELING SPECTROSCOPY OF 2D MATERIALS : UNRAVELING THEIR DENSITY OF STATES AND THE RELATIONSHIP WITH Thaís Chagas Peixoto Silva TUNNELING SPECTROSCOPY OF 2D MATERIALS : UNRAVELING THEIR DENSITY OF STATES AND THE RELATIONSHIP WITH Thaís Chagas Peixoto Sil, (2020). https://www.fisica.ufmg.br/posgraduacao/defesas/defesa-de-tese-de-doutorado-368-thais-chagas-peixoto-silva-17-04-2020/.

[95] Solar Simulator Elements, (n.d.). https://abet-technologies.com/solar-simulators/solar-simulator-elements/ (accessed October 3, 2023).

[96] J. Cubas, S. Pindado, C. De Manuel, Explicit expressions for solar panel equivalent circuit parameters based on analytical formulation and the lambert W-function, Energies. 7 (2014) 4098–4115. https://doi.org/10.3390/en7074098.

[97] N.Y. Doumon, The degradation of organic solar cells: from chemistry to device physics through materials, University of Groningen, 2019. https://doi.org/10.33612/diss.98539626.

[98] H.S. Lee, J.Y. Cho, R. Nandi, P.S. Pawar, K.E. Neerugatti, C.T.K. Mai, D.-K. Lee, J. Heo, Influence of the Temperature Ramping Rate on the Performance of Vapor Transport Deposited SnS Thin-Film Solar Cells, ACS Appl. Energy Mater. (2020). https://doi.org/10.1021/acsaem.0c01164.

[99] P.S. Pawar, J.Y. Cho, K.R.E. Neerugatti, S. Sinha, T.R. Rana, S.J. Ahn, J. Heo, Solution-Processed ZnxCd1-xS Buffer Layers for Vapor Transport-Deposited SnS Thin-Film Solar Cells: Achieving High Open-Circuit Voltage, ACS Appl. Mater. Interfaces. 12 (2020)

7001–7009. https://doi.org/10.1021/acsami.9b14329.

[100] D. Lim, H. Suh, M. Suryawanshi, G.Y. Song, J.Y. Cho, J.H. Kim, J.H. Jang, C.W. Jeon, A. Cho, S.J. Ahn, J. Heo, Kinetically Controlled Growth of Phase-Pure SnS Absorbers for Thin Film Solar Cells: Achieving Efficiency Near 3% with Long-Term Stability Using an SnS/CdS Heterojunction, Adv. Energy Mater. 8 (2018) 1–9. https://doi.org/10.1002/aenm.201702605.

[101] D. Lee, J.Y. Cho, H.S. Yun, D.K. Lee, T. Kim, K. Bang, Y.S. Lee, H.Y. Kim, J. Heo, Vapor transport deposited tin monosulfide for thin-film solar cells: Effect of deposition temperature and duration, J. Mater. Chem. A. 7 (2019) 7186–7193. https://doi.org/10.1039/c8ta09820d.

[102] J.M. Skelton, L.A. Burton, F. Oba, A. Walsh, Metastable cubic tin sulfide: A novel phonon-stable chiral semiconductor, APL Mater. 5 (2017) 036101. https://doi.org/10.1063/1.4977868.

[103] A. Rabkin, S. Samuha, R.E. Abutbul, V. Ezersky, L. Meshi, Y. Golan, New Nanocrystalline Materials: A Previously Unknown Simple Cubic Phase in the SnS Binary System, Nano Lett. 15 (2015) 2174–2179. https://doi.org/10.1021/acs.nanolett.5b00209.

[104] P.K. Nair, A.R. Garcia-Angelmo, M.T.S. Nair, Cubic and orthorhombic SnS thin-film absorbers for tin sulfide solar cells, Phys. Status Solidi. 213 (2016) 170–177. https://doi.org/10.1002/pssa.201532426.

[105] R.E. Abutbul, E. Segev, L. Zeiri, V. Ezersky, G. Makov, Y. Golan, Synthesis and properties of nanocrystalline π-SnS – a new cubic phase of tin sulphide, RSC Adv. 6 (2016) 5848–5855. https://doi.org/10.1039/C5RA23092F.

[106] D.R.G. Mitchell, DiffTools: Electron diffraction software tools for DigitalMicrograph^{TM}, Microsc. Res. Tech. 71 (2008) 588–593. https://doi.org/10.1002/jemt.20591.

[107] C. Ye, X. Fang, Y. Hao, X. Teng, L. Zhang, Zinc Oxide Nanostructures: Morphology Derivation and Evolution, J. Phys. Chem. B. 109 (2005) 19758–19765. https://doi.org/10.1021/jp0509358.

[108] I.Y. Ahmet, M. Guc, Y. Sánchez, M. Neuschitzer, V. Izquierdo-Roca, E. Saucedo, A.L. Johnson, Evaluation of AA-CVD deposited phase pure polymorphs of SnS for thin films solar cells, RSC Adv. 9 (2019) 14899–14909. https://doi.org/10.1039/C9RA01938C.

[109] J. Xia, X.-Z. Li, X. Huang, N. Mao, D.-D. Zhu, L. Wang, H. Xu, X.-M. Meng, Physical vapor deposition synthesis of two-dimensional orthorhombic SnS flakes with strong angle/temperature-dependent Raman responses, Nanoscale. 8 (2016) 2063–2070. https://doi.org/10.1039/C5NR07675G.

[110] S. Lin, A. Carvalho, S. Yan, R. Li, S. Kim, A. Rodin, L. Carvalho, E.M. Chan, X. Wang, A.H.

Castro Neto, J. Yao, Accessing valley degree of freedom in bulk Tin(II) sulfide at room temperature, Nat. Commun. 9 (2018) 1455. https://doi.org/10.1038/s41467-018-03897-3.

[111] G.A. Tritsaris, B.D. Malone, E. Kaxiras, Structural stability and electronic properties of low-index surfaces of SnS, J. Appl. Phys. 115 (2014) 173702. https://doi.org/10.1063/1.4874775.

[112] Z.A. Jahangirli, Self-consistent calculations of the electronic structures of deep Sn and S vacancy levels in SnS by the method of green functions, Russ. J. Phys. Chem. A. 84 (2010) 1536–1539. https://doi.org/10.1134/S0036024410090165.

[113] J. Vidal, S. Lany, M. D'Avezac, A. Zunger, A. Zakutayev, J. Francis, J. Tate, Band-structure, optical properties, and defect physics of the photovoltaic semiconductor SnS, Appl. Phys. Lett. 100 (2012) 032104. https://doi.org/10.1063/1.3675880.

[114] P. Villars, Pearson's Handbook Desk Edition :Crystalographic Data for Intermetallic Phases, 1998.

[115] J.M. Skelton, L.A. Burton, F. Oba, A. Walsh, Metastable cubic tin sulfide: A novel phonon-stable chiral semiconductor, APL Mater. 5 (2017) 036101. https://doi.org/10.1063/1.4977868.

[116] J.M. Skelton, L.A. Burton, A.J. Jackson, F. Oba, S.C. Parker, A. Walsh, Lattice dynamics of the tin sulphides SnS 2 , SnS and Sn 2 S 3 : vibrational spectra and thermal transport, Phys. Chem. Chem. Phys. 19 (2017) 12452–12465. https://doi.org/10.1039/C7CP01680H.

[117] L.A. Burton, A. Walsh, Phase Stability of the Earth-Abundant Tin Sulfides SnS, SnS 2 , and Sn 2 S 3, J. Phys. Chem. C. 116 (2012) 24262–24267. https://doi.org/10.1021/jp309154s.

.